Nuclear Physics in Neutron Stars : Study of Superfluidity in Hypernuclei and Constraining the Nuclear Equation of State

Haşim Zahid Güven

Thèse de doctorat

NNT: 2020UPASP041

Nuclear Physics in Neutron Stars: Study of Superfluidity in Hypernuclei and Constraining the Nuclear Equation of State

Thèse de doctorat de Yildiz Technical University et de l'université Paris-Saclay

École doctorale n° 576, Particules hadrons énergie et noyau : Instrumentation, image, cosmos et simulation (PHENIICS)
Spécialité de doctorat: Structure et Réactions Nucléaires
Unité de recherche: Université Paris-Saclay, CNRS, IJCLab, 91405, Orsay, France.
Référent: Faculté des Sciences d'Orsay

Thèse présentée et soutenue à Orsay, le 16 Octobre 2020, par

Haşim Zahid Güven

Composition du jury:

Patrice Hello Professeur des Universités, Laboratoire de physique des 2 infinis - Irene Joliot-Curie (IJCLab)	Président
Francesca Gulminelli Professeur des Universités, Laboratoire de Physique Corpusculaire de Caen	Rapporteur & Examinateur
Micaela Oertel Directeur de Recherche, Laboratoire Univers et Théories (LUTH)	Rapporteur & Examinateur
Jérôme Margueron Directeur de Recherche, Institut de Physique des 2 Infinis de Lyon, Université Claude Bernard Lyon 1	Examinateur
Elias Khan Professeur des Universités, Laboratoire de physique des 2 infinis-Irene Joliot-Curiet (IJCLab)	Co-Directeur de thèse
Kutsal Bozkurt Professeur des Universités, Yıldız Technical University, Department of Physics	Co-Directeur de thèse

Acknowledgements

This thesis is supported by the Yildiz Technical University under project number FBI-2018-3325, the Scientific and Technological Research Council of Turkey (TÜBİTAK) BİDEB 2214-A Doctoral Research program and the Scientific and Technological Research Council of Turkey (TÜBİTAK) under project number MFAG-118F098.

Contents

Introduction

One of the most important quests of nuclear physics is the finding an universal interaction for the whole baryon family. In order to pursue this quest, more than 4000 scattering experiments have been performed until now [HN18]. The scattering data tightly constrains our models of the nucleon–nucleon interaction. However, while these experiments for finite nuclei probe finite ranges giving some clues up to nuclear saturation densities ($n_{\rm sat} \approx 0.16$ fm^{-3}, $\rho_{\rm sat} \approx 2.7 \times 10^{14}$ g/cm^3) and heavy-ion collisions explore a wider domain of densities with small isospin asymmetries, neutron stars (NSs) are the only system (for now) which explores the equilibrium properties of dense matter at densities well above saturation density and isospin asymmetries close to pure neutron matter [RPJ+18]. NS physics addresses thus one of the most fundamental questions in nuclear physics which is the understanding of the nuclear interaction in dense medium as a function of the density and the isospin asymmetry. They are excellent systems where the high density behavior of the nuclear equation of state (EoS) can potentially be determined. Although there are considerable astrophysical observations, a lot of uncertainties related to the structure of NS still exist.

Let us first give some information about the structure of NS. The outermost surface of the NS contains a very thin atmosphere of only a few centimeters thick that is composed of H, but may also contain heavier elements such as He and C [HPY07]. The detected electromagnetic radiation may be used to constrain critical parameters of the neutron star. For instance a black-body emission from the stellar surface at given temperature provides a

determination of the stellar radius from the Stefan-Boltzmann law. Unfortunately there are lots of uncertainties to determine exact values of radii (see Sec. 3.1 for details). Just below the atmosphere, the 1 km thick envelope (which also named crust) behave as a blanket between the cold atmosphere (with $T = 10^6$ K) and hot core (with $T = 10^8$ K) [PLPS04, HPY07]. The crust density varies from $10^{-3}\rho_{\rm sat}$ to $0.5\rho_{\rm sat}$ [HPY07]. It consists of electrons, free neutrons, and neutron-rich atomic nuclei. However, free neutrons start to appear where the density higher than the neutronization density ($\rho_{\rm ND} = 4 \times 10^{11}$ g/cm^3). This region usually named inner crust. As the density grows, the fraction of free neutrons increase [HPY07]. Besides, free neutrons and neutron rich-nuclei can also be in a superfluid state depending on temperature which has a significant impact on cooling scenarios of NSs [PLPS04, SC19]. At a density larger than $0.5\rho_{\rm sat}$, the finite-nuclear phase disappears and a new state of matter is formed [HPY07]. This section of NS is called "core" which is responsible for almost all the mass of NS and approximately 95% of its total radius. Besides, its density could even reach up to $10\rho_{\rm sat}$ [ÖF16]. However, this reality comes with its own problems since the behavior of the EoS for densities $\rho \geq \rho_{\rm sat}$ is not accurately known from experiments of nuclear physics and also their extrapolations to $2 - 10\rho_{\rm sat}$ are not solely reliable. For convenience, a general nomenclature is created which is named "outer core" for densities $0.5\rho_{\rm sat} < \rho \leq 2\rho_{\rm sat}$ and "inner core" for densities $\rho \geq 2\rho_{\rm sat}$ [HPY07]. The EoS of NS for outer core can be investigated by using nucleonic models derived from the nuclear physics experiments since these experiments represent the knowledge around the saturation density. In this case, NS can be considered as nuclear matter consisting of neutrons and protons, as well as a gas of electrons and muons at β equilibrium [HPY07, Boo07, MTW73, RPJ+18]: This is the traditional description of the NS. However for densities $\rho \geq 2\rho_{\rm sat}$, the EoS of NS is completely unknown. Therefore, three main hypothesis are proposed to explain the inner core of NS:

- Phase transition to hypernuclear matter: Appearance of hyperons on some onset density (typically $\rho > 2\rho_{\rm sat}$), specifically Σ^- and Λ hyperons [CS13, MKV15, CV16, FAPVn17, GCS19].

- Phase transition to quark matter: Deconfined light u and d quarks and strange s quarks, and a small admixture of electrons (or not) could

form a true ground state of matter which is also called strange matter hypothesis [FJ84]. This hypothesis leads to whole star could be quark matter which is also called as a quark star. However, it is a debated issue and there can be a two different scenarios leading to quark star or the quark phase transition could occur only at a sufficiently high density [ZH13, AHP13, HS19, MTHR19]. In the case of quark phase transition, building core of NS by using quarks results in significantly small radii compared to the traditional ones [ZH13, AHP13, HS19, MTHR19] except for the quarkyonic model, which describes the transition to quark matter as a crossover [MR19].

- Pion condensation: The appearance of a boson condensate of pion-like excitations with a strong renormalization and mixing of nucleon states [HP82, FKLS92, YSZ+18]. This hypothesis is considered as the least likely, since the effect of pion condensation on EoS is predicted to be negligible from nuclear matter calculations [FKLS92].

Considering the first hypothesis, at large densities, a substantial population of hyperons are expected because the Fermi energy of neutrons becomes of the order of their rest mass, leading to an increase of the hyperon fraction, but it also reduces the degeneracy pressure inside the NS, leading to soft NS EoS at high densities, causing a problem to reach maximum observed NS mass: $2M_{\odot}$ [AFW+13, ABBS+18] where $M_{\odot}$ is the solar mass. This problem could be alleviated by adding the hypothetical repulsive interaction using some vector mesons, specifically the ϕ meson (see Ref. [ZH13] for details.) Therefore, extracting the hyperon interaction inside the nuclear medium from hypernuclear experiments has an utmost importance. However, hyperon density inside the hypernuclei is around $\rho_{\Lambda} \approx 0.21\rho_{\rm sat}$ for the case of single Λ hypernuclei which is not enough for describing the phase transition to hypernuclear matter in NSs (see Ref. [HY09]for details) where the density of Λ could even reached up to $5\rho_{\rm sat}$ [GHM16]. One possible solution to extend Λ density is investigating multi-strange hypernuclei. In this case, there could be superfluidity (or in simple terms: pairing) which can affect the interpretation of the experiments related to multi-strange hypernuclei. Besides, the pairing interaction in the strange sector could have an important effect on the cooling curves of neutron stars [SC19]. However, the Λ pairing channel in hypernuclei is completely unknown. Therefore, the first part of the the-

sis is devoted to the investigation of the Λ pairing channel on hypernuclei. In Chap. 1, the theoretical foundations of mean field approximation (with Hartree-Fock-Bogoliubov or Bogoliubov-de Gennes equations) for hypernuclei are explained [RS04, DFT84, BD05]. We considered hypernuclei with proton and neutron closed shells, e.g. ${}^{40-S}_{-S\Lambda}$Ca, ${}^{132-S}_{-S\Lambda}$Sn and ${}^{208-S}_{-S\Lambda}$Pb, since semi-magicity often guarantees that nuclei remain at, or close to, sphericity. In Chap. 2, both nucleon-Λ and Λ-Λ pairing channel are investigated and their effect on the ground state properties such as binding energies, single particle spectrums and particle densities are calculated on ${}^{40-S}_{-S\Lambda}$Ca, ${}^{132-S}_{-S\Lambda}$Sn and ${}^{208-S}_{-S\Lambda}$Pb hypernuclei.

The advent of first detection of gravitational waves from a binary NS merger (GW170817) by the LIGO-Virgo collaboration [AAA+17, AAA+19], opens a new era for nuclear astrophysics since it provides an additional observable related to the EoS of NS, among which the Tidal deformability ($\tilde{\Lambda}$) [Hin08, FH08, DN09]. Considering this "new" observable, the second part of the thesis is devoted to constrain the nuclear EoS. To do this, nuclear EoSs generated by using observational data such as the maximum mass ($2M_\odot$ see Refs. [AFW+13, ABBS+18] for details) and $\tilde{\Lambda}$ from the gravitational wave event of GW170817 [AAA+17, DFL+18, AAA+19, CDMM19] as well as predictions from nuclear physics such as Chiral Effective Field Theory (χEFT) [DHS16] and Isoscalar Giant Monopole Resonance (ISGMR) [KMV12, KM13] are confronted to each other. In Chap. 3, the theoretical fundamentals of meta-model [MCG18a], Tolman-Oppenheimer-Volkoff (TOV) [Tol39, OV39] and Pulsation equations [Hin08, FH08, DN09] are given. In order to connect observational data with theoretical predictions of nuclear physics, a brief overview on Bayesian statistics is also given [SS06]. Finally with the power of Bayesian statistics, the building of the posterior probability from the likelihood one, which includes all constraints, and from the prior on the model parameters, are detailed. In Chap. 4, the analysis of the posterior probabilities is undertaken for the following empirical parameters: $L_{\rm sym}$, $K_{\rm sym}$, $Q_{\rm sat}$ and $Q_{\rm sym}$ as well as for the radius of $1.4M_\odot$, $R_{1.4}$, and the pressure at $2n_{\rm sat}$, $P(2n_{\rm sat})$. We then analyze origins of the correlation between the $L_{\rm sym}$-$K_{\rm sym}$ and $K_{\rm sat}$-$Q_{\rm sat}$ parameters. Finally, their implications on nuclear and NS physics are discussed in detail.

Studies conducted during the thesis have been published in following references:

- H. Güven, K. Bozkurt, E. Khan, and J. Margueron, "ΛΛ pairing in multi-strange hypernuclei", Physical Review C 98, 014318 (2018).
- H. Güven, K. Bozkurt, E. Khan, and J. Margueron, "Multi-messenger and multi-physics bayesian inference for GW170817 binary neutron star merger", Physical Review C 102, 015805 (2020).

Part I

STRANGENESS IN NUCLEAR STRUCTURE

1

Pairing in Hypernuclei: Theoretical Foundations

1.1. A Strange System: Hypernucleus and Hypernuclei

A hypernucleus is an extra-ordinary nucleus including ordinary nucleons with one (or more) strange baryons (hyperons). It was first detected from hyper-fragments exposed to cosmic rays [DP53] in 1952. One year after, a new quantum number, "strangeness", was introduced [GM53, NN53]. The reason why it is called "strangeness" is that, these systems are bound with the time-scale of strong interaction (10^{-23} s) but decay only with the weak interaction (which time-scale is 10^{-10} s) inside of the nucleus. Therefore, hypernuclei can be investigated with a many-body framework typically used in nuclear physics. Within the last 40 years, modern particle accelerators and electronic instrumentation have increased the rate and breadth of the experimental investigation of strangeness in nuclei (especially, the Japan Proton Accelerator Research Complex in Japan and the proton antiproton detector array at GSI Facility for Antiproton and Ion Research [Nag13, AAA+13, ABC+09, SNR+12]). As often, the theoretical interest has closely followed the experimental development.

A hyperon is characterized by its strangeness number S which is $S = -1$ for Λ, Σ^+, Σ^-, Σ^0 and $S = -2$ for Ξ^-, Ξ^0. The strangeness of a hypernucleus is determined by the strangeness number of the hyperon if the hypernucleus contains only one hyperon. However, some hypernuclei can contain more than one hyperon, forming a multi-strangeness hypernucleus where the strangeness of the system is defined by summing all of the strangeness number of each hyperons of hypernuclei.

Although in principle, any hyperon could be bound with an ordinary nucleus to form a hypernucleus, there is a specific attention for the Λ since the mass ($m_\Lambda = 1115.683 \pm 0.006$ MeV/c^2) is the smallest one compared to other hyperons ($m_{\Sigma^+} = 1189.370 \pm 0.070$ MeV/c^2, $m_{\Sigma^0} = 1192.642 \pm 0.024$ MeV/c^2, $m_{\Sigma^-} = 1197.449 \pm 0.030$ MeV/c^2, $m_{\Xi^-} = 1321.710 \pm 0.070$ MeV/c^2 and $m_{\Xi^0} = 1314.860 \pm 0.200$ MeV/c^2) [THH+18] and it also has an attractive interaction inside of the nucleus [GHM16]. It is therefore easier to probe Λ than other hyperons. Another reason for choosing Λ is that since other hyperons (Σ^+, Σ^-, Σ^0, Ξ^- and Ξ^0) decay to Λ inside the nucleus [HN18, BBG12], observing Λ hypernuclei is the easiest way to understand hyperon-nucleon interaction at first order. Experimentally, there are sufficient experimental data related to single-Λ hypernuclei, from ${}^{5}_{\Lambda}$He to ${}^{208}_{\Lambda}$Pb, which are relevant to understand the Λ-nucleon interaction, at least at very low density. Λ separation energies and single particle structures of these hypernuclei is now fairly known [HT06, GHM16]. For Σ hypernuclei, it is generally assumed that the bound Σ hypernuclear system does not exist except for ${}^{4}_{\Sigma}$He [HII+89, NAA+19]. The Σ^+ separation energy for ${}^{4}_{\Sigma}$He was measured to be 3.2 MeV [HII+89] (for comparison: 2.39 MeV for ${}^{4}_{\Lambda}$He [HT06, GHM16]). Besides, Ref. [NAA+19] shows that ${}^{4}_{\Sigma}$He has not any excited state. In the $-S \geq 2$, the situation is slightly better than the Σ case. There are few experimental data about double-Λ hypernuclei due to their low production rates of kaons, with some observed hypernuclei such as ${}^{6}_{\Lambda\Lambda}$He or ${}^{10}_{\Lambda\Lambda}$Be, allowing to extract the bond energy which is strongly related to Λ-Λ interaction [AAA+13, ABC+09, TAA+01, NT10]. The famous "NAGARA" event allows to determine the bond energy of ${}^{6}_{\Lambda\Lambda}$He to be 0.6-1 MeV [AAA+13, ABC+09, TAA+01, NT10]. Another case for $-S = 2$ is the Ξ hypernucleus. Unfortunately, there is only one event reported related to Ξ hypernucleus, "KISO" event for ${}^{15}_{\Xi^-}$C [NEF+15] where Ξ^- separation energies allow to conclude either $B_{\Xi^-} = 4.38 \pm 0.25$ MeV or $B_{\Xi^-} = 1.11 \pm 0.25$ MeV (see

Ref. [HN18] for details). However, if one considers the Coulomb interaction which is predicted to be 3 MeV for ${}^{15}_{\Xi^-}$C [HN18], Ξ-nucleon interaction could be either attractive or repulsive. All in all, due to the large experimental uncertainty on Σ and Ξ hypernuclei measurements, in the present work, we consider the case of Λ hypernuclei.

Let us now discuss about the theoretical description of hypernuclei. Λ hypernuclei have often been considered as the best system to investigate the nature of hyper-nuclear interactions in the baryon octet [FN15, GHM16]. Despite the numerous theoretical works about hypernuclei physics within various frameworks, such as relativistic mean field [RSZ17, vDCS14, HF08, YSZZ98], G-matrix combined with Skyrme-Hartree-Fock for finite-nuclei [GDS12, SR13, ZHS16, VPRS01], generalized liquid drop model [Sam10], as well as more recently quantum Monte-Carlo approach [LGP13, LLGP15], there are still open questions concerning the understanding of multi-strange nuclei and the hypernuclear equation of state. In general the main difficulties for theoretical approaches is the very scarce amount of experimental data, as explained in the previous paragraph. Constraints on the hyperon interactions are therefore still weak. As an example, the NNΛ interaction is still subject of debate [LGP13, LLGP15]. Most of the recent theoretical approaches predict binding energies and single particle energies of single-Λ systems such as ${}^{5}_{\Lambda}$He, ${}^{9}_{\Lambda}$Be, ${}^{13}_{\Lambda}$C, ${}^{209}_{\Lambda}$Pb in good agreement with the experimental data [RSZ17, vDCS14]. In the present work, for instance, we consider density functional approaches where the nucleon sector is treated with Skyrme interaction and the NΛ channel is based on G-matrix calculations starting from various bare interactions such as NSC89, NSC97a–f (Nijmegen Soft Core Potentials) or ESC08 (Extendend Soft Core Potentials) [SR13, VPRS01]. The older DF-NSC89 functional can reproduce with a good accuracy the experimental single particle energies of Λ hyperon for light hypernuclei such as ${}^{5}_{\Lambda}$He or ${}^{13}_{\Lambda}$C, but for heavier hypernuclei like ${}^{41}_{\Lambda}$Ca or ${}^{209}_{\Lambda}$Pb, DF-NSC97a–f and DF-ESC08 are better [SR13, VPRS01]. It should be noted that this discrepancy between the interactions can be removed with adequate fitting such as introducing new three body correction terms in energy functionals for the single Λ hypernuclei (see Ref. [SR13] for details).

There are still many open questions related to hypernuclei. The first one deals with the strength of the ΛΛ force. In general, the experimental bond energy of multi-strange systems, such as ${}^{6}_{\Lambda\Lambda}$He or ${}^{10}_{\Lambda\Lambda}$Be, are not reproduced

by the usual density functionals [YSZZ98]: the DF-NSC89 and DF-NSC97f forces predict bond energies ranging from -0.34 MeV ($^{10}_{\Lambda\Lambda}$Be) to -0.12 MeV ($^{210}_{\Lambda\Lambda}$Pb) while the DF-NSC97a, which has strong $\Lambda\Lambda$ interaction, predicts bond energies from 0.37 MeV ($^{10}_{\Lambda\Lambda}$Be) to 0.01 MeV ($^{210}_{\Lambda\Lambda}$Pb) [VPRS01]. It should be noted that more recent density functionals, e.g. the one derived from the ESC08 potential, do not better to reproduce the bond energy (-0.57 MeV for ESC08 in $^{6}_{\Lambda\Lambda}$He [VPRS01]). In order to improve the description of the $\Lambda\Lambda$ force, an empirical correction for DF-NSC89 and DF-NSC97a–f in the $\Lambda\Lambda$ channel has been proposed and fitted to the bond energies of $^{6}_{\Lambda\Lambda}$He (which is $\sim$ 0.6-1 MeV [AAA+13, ABC+09, TAA+01, NT10]) and named EmpC (see Ref. [MKG17] for details). Note that similar issues exist with relativistic approaches for hypernuclei and it was recently proposed then the fit of the bond energy shall enter directly in the definition of the Lagrangian [FAPVn17]. Therefore we shall use DF-NSC89, DF-NSC97a and DF-NSC97f with EmpC potentials due to the compatible results of $\Lambda\Lambda$ channel.

Besides, a well-known issue is indeed the so-called hyperon puzzle in neutron stars [CS13, MKV15, CV16, FAPVn17, GCS19]. It refers to the difficulty for many approaches to reach the largest observed mass of neutron stars, of about $1.9-2.0 M_\odot$ [AFW+13, FPE+16] when considering the softening induced by the onset of hyperons in the nuclear matter. The possible solutions may be that the hyperon interaction turns strongly repulsive in dense matter, counter balancing the softening of the phase transition to hypernuclear matter [CS13, ZH13, MKV15, CV16, FAPVn17, GCS19], or quark phase appears before the hypernuclear matter [AHP13, HS19, MTHR19, MR19]. A brief of discussion about the phase transition considering hyperons (or a quark phase) on neutron stars is given in Sec. 3.2.

There is however a question which has not been addressed yet and may modify our understanding of the $\Lambda\Lambda$ channel in finite hypernuclei: are Λ particles paired, and how much Λ pairing impacts the ground state properties of hypernuclei (density distributions, binding energies, etc.)? It should be noted that although there is currently no microscopic calculation in hypernuclei including Λ pairing, the pairing gap in hypernuclear matter has been calculated within the Bardeen–Cooper–Schrieffer (BCS) approximation [BB98, TT00, TMC03, ZSPD05, WS10]. The present work aims to provide a first investigation to the Λ pairing in finite hypernuclei by considering a rather optimistic scenario for the strength of $\Lambda\Lambda$ pairing.

Another question related to multi-strange nuclei deals with the presence of other strange baryons than Λ, such as Ξ, Σ or Ω. Ξ is the most crucial one because the $\Lambda+\Lambda \rightarrow \mathrm{N} + \Xi$ decay channel (also called Ξ-instability) can make it appear in the ground state of hypernuclei [MKG17, SBG00]. The attractive nature of the Ξ potential in nuclear matter ($\mathrm{U}_\Xi = -14$ MeV)[KAB+00] stabilizes Ξ and both Ξ^0 and Ξ^- hyperons are predicted in hypernuclei with a strangeness number $-S \geq 20 - 30$ [MKG17]. Besides, a Λ hyperon can also decay to Σ^0, Σ^+ and Σ^-. However, due to the high average free reaction (Q^{free}) values of Σ hyperons ($Q_\Sigma^{free} = -80$ MeV for Σ and $Q_\Xi^{free} = -26$ MeV for Ξ [SBG00, MKG17]), the decay of Λ to $\Sigma^{\pm,0}$ is not favored in finite hypernuclei. Since the presence of Ξ in the ground state is not expected to enhance the Λ pairing, and since the pairing in the Ξ channel is even less known that the one in the Λ channel, we shall focus our present study on the pairing in Λ hypernuclei. We do not expect our conclusions to be strongly modified by the presence of hyperons other than Λ in finite nuclei.

1.2. Main Principles

In the present work, the ground state properties of single and multi-Λ hypernuclei are investigated with Hartree-Fock-Bogoliubov (HFB) formalism considering $\Lambda\Lambda$ pairing interactions (Please see Sec.1.3.3 for details). On this purpose we neglect the Λ spin-orbit interaction, which is estimated to be very small [HT06, MLMY08, FKVW07] and the three body interactions such as NNΛ [LGP13, LLGP15] is effectively included from the functional approach. We have considered a zero range pairing force in the $\Lambda\Lambda$ channel, opening the possibility to calculate accurately open-Λ shell hypernuclei. In addition, our calculation are performed in spherical symmetry since deformation is not expected to greatly increase pairing correlations. We have considered hypernuclei with proton and neutron closed shells, e.g. ${}^{40-S}_{-S\Lambda}$Ca, ${}^{132-S}_{-S\Lambda}$Sn and ${}^{208-S}_{-S\Lambda}$Pb (where S is the total strangeness number of hypernuclei), since semi-magicity often guarantees that nuclei remain at, or close to, sphericity (see Ref. [Tan19] for the general case of $N = Z$ hypernuclei). A future study evaluating the effect of deformation on the pairing correlation for open shell Λ states would however be interesting to confirm our conclusions.

1.3. Mean Field Approximation

Considering a non-relativistic system composed of interacting nucleons N=(p,n) and $\Lambda's$, the total Hamiltonian reads,

$$\widehat{H} = \widehat{T}_N + \widehat{T}_\Lambda + \widehat{H}_{NN} + \widehat{H}_{N\Lambda} + \widehat{H}_{\Lambda\Lambda}, \tag{1.1}$$

where $\widehat{T}_A$ are the kinetic energy operators and $\widehat{H}_{AB}$ are the interaction operator terms acting between A and B species ($A, B = N, \Lambda$).

1.3.1 The Particle-Hole Channel

In the mean field approximation the ground state of the system is the tensor product $|\Psi_N\rangle \otimes |\Psi_\Lambda\rangle$, where $|\Psi_N\rangle$ ($|\Psi_\Lambda\rangle$) is a slater determinant of the nucleon (Λ) states. The total Hamiltonian (1.1) can be turned into a density functional $\epsilon(\rho_N, \rho_\Lambda)$, of the particle densities ρ_N and ρ_Λ, as $\widehat{H} = \int \epsilon(\rho_N, \rho_\Lambda) d^3r$. The energy functional ϵ is often expressed as [VPRS01, CLS00],

$$\begin{aligned}\epsilon(\rho_N, \rho_\Lambda) = \frac{\hbar}{2m_N}\tau_N + \frac{\hbar}{2m_\Lambda}\tau_\Lambda + \epsilon_{NN}(\rho_N) \\ + \epsilon_{N\Lambda}(\rho_N, \rho_\Lambda) + \epsilon_{\Lambda\Lambda}(\rho_\Lambda),\end{aligned} \tag{1.2}$$

where τ_N (τ_Λ) is the nucleonic (Λ) kinetic energy density and ϵ_{ij} are the interaction terms of the energy density functional describing the NN, NΛ and $\Lambda\Lambda$ channels.

In the following, the nucleonic terms will be deduced from the well known SLy5 Skyrme interaction [BHR03] widely used for the description of the structure of finite nuclei, while the $N\Lambda$ channel is given by a density functional $\epsilon_{N\Lambda}$ adjusted to Brueckner-Hartree-Fock (BHF) predictions in uniform matter [VPRS01, CLS00],

$$\epsilon_{N\Lambda}(\rho_N, \rho_\Lambda) = -f_1(\rho_N)\rho_N\rho_\Lambda + f_2(\rho_N)\rho_N\rho_\Lambda^{5/3}. \tag{1.3}$$

Although BHF predictions of hypernuclear matter are not compatible with neutron stars [CV16] due to the uncertainty at high density part of hyperonic

Functional	α_1	α_2	α_3	α_4	α_5	α_6	α_7
DF-NSC89 +EmpC	327	1159	1163	335	1102	1660	22.81
DF-NSC97a +EmpC	423	1899	3795	577	4017	11061	21.12
DF-NSC97f +EmpC	384	1473	1933	635	1829	4100	33.25

Tab. 1.1: Parameters of the functionals DF-NSC89, DF-NSC97a and DF-NSC97f considering EmpC prescription for α_7 [MKG17].

equation of state, it is rather sufficient to predict the experimental properties of hypernuclei (Please see Ref. [SR13] for details). Since the spin-orbit doublets are experimentally undistinguishable [HT06, MLMY08], the spin-orbit interaction among Λ particles is also neglected [KMGR15]. The following density functionals are considered for the $N\Lambda$ channel: DF-NSC89 from Ref. [CLS00], DF-NSC97a and DF-NSC97f from Ref. [VPRS01].

In the $\Lambda\Lambda$ channel $\epsilon_{\Lambda\Lambda}$ is adjusted to the experimental bond energy in ${}^{6}_{\Lambda\Lambda}$He [MKG17] from Nagara event (see Sec. 1.1 for details) [AAA+13, ABC+09, TAA+01, NT10]:

$$\epsilon_{\Lambda\Lambda}(\rho_\Lambda) = -f_3(\rho_\Lambda)\rho_\Lambda^2. \tag{1.4}$$

The corresponding empirical approach EmpC for the $\Lambda\Lambda$ channel is considered in the present work (see Ref. [MKG17] for details). The functions f_{1-3} in Eqs. (1.3, 1.4) are expressed as,

$$f_1(\rho_N) = \alpha_1 - \alpha_2\rho_N + \alpha_3\rho_N^2, \tag{1.5}$$
$$f_2(\rho_N) = \alpha_4 - \alpha_5\rho_N + \alpha_6\rho_N^2, \tag{1.6}$$
$$f_3(\rho_\Lambda) = \alpha_7 - \alpha_8\rho_\Lambda + \alpha_9\rho_\Lambda^2, \tag{1.7}$$

where α_{1-7} are constants given in Tab. 1.1. Since the high density behavior of hyperon-hyperon interaction is completely unknown, the parameters α_8 and α_9 are therefore simply chosen to be 0 (the same approach has been done in Ref. [MKG17]).

In uniform nuclear matter the single particle energies read,

$$\epsilon_N(k) = \frac{\hbar^2 k^2}{2m_N^*} + v_{NN}^{matt.} \text{ and } \epsilon_\Lambda(k) = \frac{\hbar^2 k^2}{2m_\Lambda^*} + v_\Lambda^{matt.}, \tag{1.8}$$

where the $v_\Lambda^{matt.}$ decomposes as,

$$v_\Lambda^{matt.} = v_{N\Lambda}^{matt.} + v_{\Lambda\Lambda}^{matt.}. \tag{1.9}$$

The potentials $v_{NN}^{matt.}$, $v_{N\Lambda}^{matt.}$ and $v_{\Lambda\Lambda}^{matt.}$ derive from the energy functionals. Namely,

$$v_{NN}^{matt.}(\rho_N, \rho_\Lambda) = v_N^{Skyrme} + \frac{\partial \epsilon_{N\Lambda}}{\partial \rho_N}, \tag{1.10}$$

$$v_{N\Lambda}^{matt.}(\rho_\Lambda) = \frac{\partial \epsilon_{N\Lambda}}{\partial \rho_\Lambda}, \tag{1.11}$$

$$v_{\Lambda\Lambda}^{matt.}(\rho_\Lambda) = \frac{\partial \epsilon_{\Lambda\Lambda}}{\partial \rho_\Lambda}. \tag{1.12}$$

The nucleon effective mass is given from Skyrme interaction [BBM08] and the Λ effective mass is expressed as a polynomial in the nucleonic density ρ_N as [CLS00],

$$\frac{m_\Lambda^*(\rho_N)}{m_\Lambda} = \mu_1 - \mu_2 \rho_N + \mu_3 \rho_N^2 - \mu_4 \rho_N^3. \tag{1.13}$$

The values for the parameters μ_{1-4} are given in Tab. 1.2.

In hypernuclei, energy densities ϵ_N and ϵ_Λ are corrected by the effective mass term before deriving potentials as (see Ref. [MKG17] and therein),

$$\epsilon_{NN}^{nucl.}(\rho_N) = \epsilon_{NN}(\rho_N) - \frac{3\hbar^2}{10 m_N} \rho_N^{5/3} \left(\frac{6\pi^2}{g_N}\right)^{2/3} \left[\frac{m_N}{m_N^*} - 1\right], \tag{1.14}$$

$$\epsilon_{N\Lambda}^{nucl.}(\rho_N, \rho_\Lambda) = \epsilon_{N\Lambda}(\rho_N, \rho_\Lambda) - \frac{3\hbar^2}{10 m_\Lambda} \rho_\Lambda^{5/3} \left(\frac{6\pi^2}{g_\Lambda}\right)^{2/3} \left[\frac{m_\Lambda}{m_\Lambda^*} - 1\right], \tag{1.15}$$

$$\epsilon_{\Lambda\Lambda}^{nucl.}(\rho_\Lambda) = \epsilon_{\Lambda\Lambda}(\rho_\Lambda), \tag{1.16}$$

Force	μ_1	μ_2	μ_3	μ_4
DF-NSC89	1.00	1.83	5.33	6.07
DF-NSC97a	0.98	1.72	3.18	0
DF-NSC97f	0.93	2.19	3.89	0

Tab. 1.2: The parameters of the Λ-effective mass.

where $\epsilon_{NN}^{nucl}(\rho_N)$ satisfies

$$\frac{\partial \epsilon_{NN}^{nucl}(\rho_N)}{\partial \rho_N} = v_N^{Skyrme}. \tag{1.17}$$

The present functional (SLy5 in the NN channel, DF-NSC in the NΛ channel and EmpC in the ΛΛ channel) therefore yields an optimal set to perform HF calculations in hypernuclei (see [MKG17] for details). The implementation of energy functionals to mean field approximation are shown in Sec.1.3.2.

1.3.2 Hartree-Fock-Bogoliubov Equations

The Hartree-Fock-Bogoliubov (HFB) framework is well designed for the treatment of pairing both for strongly and weakly bound systems. In this work, we study hypernuclei which are magic in neutron and proton and open-shell in Λ. We thus consider the HFB framework in the ΛΛ channel, and the NN channel is treated (naturally) within Hartree-Fock (HF) since we consider closed proton and neutron shells. In addition, because of their magic properties in the nucleon sector, which still contains the majority of particles, we consider spherical symmetry. In the HFB approach the mean field matrix that characterizes the system is obtained from the particle and pairing energy densities [RS04].

In order define the particle and pairing energy densities, one should define a quasi-particle state. The basic idea of quasi-particle concept is representation the ground state of nucleus as a vacuum with respect to quasi-particles, which are defined by the low-lying excitations of neighboring nuclei. A quasi-particle state is defined as a vacuum of quasi-particle operators which are

linear combinations of particle creation and annihilation operators which can be shown as

$$\mid \Psi \Big\rangle = \exp\Big\{ -\frac{1}{2}\int d^3\mathbf{r}d^3\mathbf{r}' \sum_{\sigma\sigma'} Z^+(\mathbf{r}\sigma,\mathbf{r}'\sigma')a^+_{\mathbf{r}\sigma}a^+_{\mathbf{r}'\sigma'}\Big\} \mid 0\Big\rangle \tag{1.18}$$

which is defined by the antisymmetric complex function $Z^+(\mathbf{r}\sigma,\mathbf{r}'\sigma')= -Z^*(\mathbf{r}\sigma,\mathbf{r}'\sigma')$ of the space-spin coordinates [RS04]. In the Eq.(1.18), $\mid 0\rangle$ is a vacuum state and $a^+_{\mathbf{r}\sigma}$ is creation operators which affect nucleon with $\sigma = \pm 1/2$ spin at point r. Particle and pairing densities can be expressed from the quasi-particle sates as

$$\rho(\mathbf{r}\sigma q,\mathbf{r}'\sigma' q') = \Big\langle \Psi | a^+_{\mathbf{r}'\sigma' q'} a_{\mathbf{r}\sigma q} | \Psi \Big\rangle, \tag{1.19}$$

$$\tilde{\rho}(\mathbf{r}\sigma q,\mathbf{r}'\sigma' q') = -2\sigma' \Big\langle \Psi | a_{\mathbf{r}'-\sigma' q'} a_{\mathbf{r}\sigma q} | \Psi \Big\rangle. \tag{1.20}$$

where $a^+_{r'\sigma' q'}$ and $a_{r\sigma q}$ are creation and annihilation operators which affect nucleon with $\sigma = \pm 1/2$ spin and q isospin at point r. The variation of the energy expectation value $E = \Big\langle \Psi \mid \hat{H} \mid \Psi \Big\rangle$, with respect to ρ and $\tilde{\rho}$ under the conservation of particle numbers, leads to HFB (or Bogoliubov-de Gennes) equations which also is an eigenvalue problem for the single particle states ($\psi_1(E,\mathbf{r}\sigma)$ and $\psi_2(E,\mathbf{r}\sigma)$ corresponding to particle-particle and particle-hole) in coordinate space:

$$\begin{aligned} \int d^3\mathbf{r}' \textstyle\sum_{\sigma'} \begin{pmatrix} h(\mathbf{r}\sigma,\mathbf{r}'\sigma') & \tilde{h}(\mathbf{r}\sigma,\mathbf{r}'\sigma') \\ \tilde{h}(\mathbf{r}\sigma,\mathbf{r}'\sigma') & -h(\mathbf{r}\sigma,\mathbf{r}'\sigma') \end{pmatrix} \begin{pmatrix} \psi_1(E,\mathbf{r}'\sigma') \\ \psi_2(E,\mathbf{r}'\sigma') \end{pmatrix} \\ = \begin{pmatrix} E+\lambda & 0 \\ 0 & E-\lambda \end{pmatrix} \begin{pmatrix} \psi_1(E,\mathbf{r}\sigma) \\ \psi_2(E,\mathbf{r}\sigma) \end{pmatrix}, \end{aligned} \tag{1.21}$$

where $h(\mathbf{r}\sigma,\mathbf{r}'\sigma')$ and $\tilde{h}(\mathbf{r}\sigma,\mathbf{r}'\sigma')$ are the mean field matrix elements, E is the eigenenergies for each quasi-particle state and λ is the Fermi energy. We solved Eq.(1.21) by the numerical iteration method which based on minimizing eigenvalues as described in Ref. [BD05]. The mean field matrix elements are obtained by variation of the expectation value of the energy with respect to the particle and pairing densities:

$$h(\mathbf{r}\sigma,\mathbf{r}'\sigma') = \frac{\delta\epsilon(\rho_N,\rho_\Lambda,\tau_N,\tau_\Lambda)}{\delta\rho(\mathbf{r}\sigma,\mathbf{r}'\sigma')}, \tag{1.22}$$

$$\tilde{h}(\mathbf{r}\sigma,\mathbf{r}'\sigma') = \frac{\delta\epsilon(\rho_N,\rho_\Lambda,\tau_N,\tau_\Lambda)}{\delta\tilde{\rho}(\mathbf{r}\sigma,\mathbf{r}'\sigma')}. \tag{1.23}$$

In Eq. (1.21), the diagonal elements of the matrix in the integral correspond to the particle-hole (Hartree-Fock) field while the non-diagonal elements of the matrix correspond to particle-particle field which includes contributions of the pairing to the mean field of the hypernucleus. Recalling Eqs. (1.14, 1.15 and 1.16), one can rewrite the total energy functional for hypernucleus:

$$\begin{aligned}\epsilon(\rho_N,\rho_\Lambda,\tau_N,\tau_\Lambda) = \frac{\hbar}{2m_N^*}\tau_N + \frac{\hbar}{2m_\Lambda^*}\tau_\Lambda + \epsilon_{NN}^{nucl.}(\rho_N) \\ +\epsilon_{N\Lambda}^{nucl.}(\rho_N,\rho_\Lambda) + \epsilon_{\Lambda\Lambda}^{nucl.}(\rho_\Lambda),\end{aligned} \tag{1.24}$$

as it is shown in Eq. (1.22), taking derivatives of Eq. (1.24) leads to the mean field operator for the particle-hole channel ($i = N, \Lambda$):

$$\int d^3\mathbf{r}' \sum_{\sigma'} h(\mathbf{r}\sigma,\mathbf{r}'\sigma') = \left[-\nabla\frac{\hbar^2}{2m_i^*(\mathbf{r})}\nabla + V_i(\mathbf{r}) - iW_i(\mathbf{r})(\nabla\times\sigma)\right], \tag{1.25}$$

where $W_i(\mathbf{r})$ is the spin-orbit term ($W_\Lambda(\mathbf{r}) = 0$ see Sec. 1.2 for details), $V_N(\mathbf{r})$ is the nucleon potential and $V_\Lambda(\mathbf{r})$ is Λ potential, respectively defined by:

$$\begin{aligned}V_N(\mathbf{r}) \equiv v_N^{Skyrme} + \frac{\partial\epsilon_{N\Lambda}}{\partial\rho_N} + \frac{\partial}{\partial\rho_N}\left[\frac{m_\Lambda}{m_\Lambda^*(\rho_N)}\right] \\ \times\left[\frac{\tau_\Lambda}{2m_\Lambda} - \frac{3}{5}\frac{(3\pi^2)^{2/3}\hbar^2}{2m_\Lambda}\rho_\Lambda^{5/3}\right],\end{aligned} \tag{1.26}$$

$$V_\Lambda(\mathbf{r}) \equiv \frac{\partial\epsilon_{N\Lambda}}{\partial\rho_\Lambda} + \frac{\partial\epsilon_{\Lambda\Lambda}}{\partial\rho_\Lambda} - \left[\frac{m_\Lambda}{m_\Lambda^*(\rho_N)} - 1\right]\frac{(3\pi^2)^{2/3}\hbar^2}{2m_\Lambda}\rho_\Lambda^{2/3}. \tag{1.27}$$

1.3.3 The Particle-Particle Channel

For the particle-particle channel, due to scarce available information, especially for the Λ pairing channel, it is convenient to consider a volume type

zero range pairing interaction in the $\Lambda\Lambda$ channel as,

$$V_{\Lambda_{pair}} = V_{\Lambda_0}\delta(\mathbf{r}-\mathbf{r'})\delta_{\sigma\sigma'}, \tag{1.28}$$

where V_{Λ_0} is the Λ pairing strength. The implementation of pairing interaction to HFB equations is shown in Sec. 1.3.4.

We now discuss the strength V_{Λ_0} of the Λ pairing interaction. At variance with the NN pairing interaction, there are not enough experimental data to set the $\Lambda\Lambda$ pairing interaction. We therefore choose to calibrate the $\Lambda\Lambda$ pairing interaction to calculations of Λ pairing gaps in uniform matter, see for instance the recent work in Ref. [RSW17]. There are several predictions for the Λ pairing gap in uniform matter which have been employed in cooling models for neutron stars. These predictions are substantially different for several reasons: they were calibrated on either the old [BB98, TT00] or the more recent [TMC03, WS10] value for the Nagara event [TAA+01]; they were considering non-relativistic [BB98, TT00] or relativistic mean field [TMC03, WS10] approaches; as a consequence, they incorporate different density dependencies of the nucleon and Λ effective masses; they are based on various Λ interactions which are weakly constrained. As a result, qualitatively different predictions have been performed in nuclear matter: the influence of the nucleon density on the Λ pairing gap has been found opposite between non-relativistic approaches [BB98, TT00] and relativistic ones [TMC03]. Despite these differences, the predictions of the Λ pairing gap at saturation density and for $k_{F_\Lambda} \approx 0.8$ fm^{-1} (corresponding to the average Λ density $\rho_{sat}/5$ in hypernuclei) are rather consistent across the different predictions and reach a maximum at about 0.5-0.8 MeV. For instance, under these conditions the Λ pairing gap is predicted to be about 0.5 MeV for $\rho_N = \rho_{sat}$ with HS-m2 parameters [TMC03], and 0.5 (0.75) MeV for NL3 (TM1) parameters with ESC00 Λ force sets [WS10]. These values are also consistent with the extrapolations of earlier calculations [BB98, TT00] in hypernuclear matter. Some interactions predict however lower values. In the following, we will therefore calibrate our $\Lambda\Lambda$ pairing interaction on hypernuclear matter predictions of Ref. [TMC03], which represents an average prediction for the maximum possible Λ pairing gap. We explain fitting procedure from the hypernuclear matter predictions at the next chapter.

In addition to the $\Lambda\Lambda$ pairing, let us mention the existence of a prediction

suggesting a strong NΛ pairing interaction in nuclear matter [ZSPD05]. In finite nuclei, large NΛ pairing gaps may however be quenched by shell effects, due to large single particle energy differences between the N and Λ states, or mismatch of the associated single particle wave functions. This will be discussed in more details in the next chapter of this thesis.

1.3.4 The Calculation of Nuclear Observables

Let us now discuss how to extract ground state properties for any hypernucleus with HFB framework. Considering Eq. (1.21), one can find energy eigenvalues and quasi-particle wave functions by solving two coupled differential equations by using numerical iterations starting from a trial wavefunction. However, we don't give the full detail about the numerical solution of HFB equations, we refer to Refs. [DFT84, BD05] for details. After the HFB iteration is converged, the particle and pairing densities can be expressed as

$$\rho(\mathbf{r}\sigma,\mathbf{r}'\sigma') = \sum_{E_n<E_{cut}} \psi_2(E_n,\mathbf{r}\sigma)\psi_2^*(E_n,\mathbf{r}'\sigma') \tag{1.29}$$

$$\tilde{\rho}(\mathbf{r}\sigma,\mathbf{r}'\sigma') = -\sum_{E_n<E_{cut}} \psi_2(E_n,\mathbf{r}\sigma)\psi_1(E_n,\mathbf{r}'\sigma'), \tag{1.30}$$

where E_{cut} is the cutoff energy which simulates the finite range of the interaction for mean fields. We used a 60 MeV cutoff energy and $15\hbar$ cutoff total angular momentum for quasi-particles, allowing for a large configuration space for all hypernuclei under study. The fact that the density matrix $\rho(\mathbf{r}\sigma,\mathbf{r}'\sigma')$ vanishes for $\mathbf{r}\to\infty$ or $\mathbf{r}'\to\infty$ leads to definition of canonical wave functions obtained from diagonalization of the particle and pairing densities [DNW+96],

$$\int d^3\mathbf{r}' \sum_{\sigma'} \rho(\mathbf{r}\sigma,\mathbf{r}'\sigma')\phi_n(\mathbf{r}'\sigma') = v_n^2\phi_n(\mathbf{r}\sigma), \tag{1.31}$$

where the v_n^2 is the occupation probability and $\phi_n(\mathbf{r}\sigma)$ are canonical states which also represents the wave function of nucleons. In order to introduce pairing field $\tilde{h}(\mathbf{r}\sigma,\mathbf{r}'\sigma')$, one can use Eq. (1.28) in the following way:

$$\tilde{h}(\mathbf{r}\sigma,\mathbf{r}'\sigma') = V_{\Lambda_{pair}} = V_{\Lambda_0}\delta(\mathbf{r}-\mathbf{r}')\delta_{\sigma\sigma'}. \tag{1.32}$$

Making the same approach as we did for Eq. (1.31), u_n^2 can be also generated as (while satisfying $v_n^2 + u_n^2 = 1$ condition) [DNW+96]

$$\int d^3\mathbf{r}' \sum_{\sigma'} \tilde{\rho}(\mathbf{r}\sigma, \mathbf{r}'\sigma')\phi_n(\mathbf{r}'\sigma') = u_n v_n \phi_n(\mathbf{r}\sigma). \tag{1.33}$$

As a result, quasi-particle wave functions ψ_1 and ψ_2 are now proportional to the canonical basis wave functions as,

$$\psi_1(E_n, \mathbf{r}\sigma) = u_n\phi_n(E_n, \mathbf{r}\sigma) \tag{1.34}$$
$$\psi_2(E_n, \mathbf{r}\sigma) = v_n\phi_n(E_n, \mathbf{r}\sigma), \tag{1.35}$$

which are also eigenfunctions of the particle-hole (Hartree-Fock) and particle-particle (pairing) field:

$$\int d^3\mathbf{r}' \sum_{\sigma'} h(\mathbf{r}\sigma, \mathbf{r}'\sigma')\phi_n(\mathbf{r}', \sigma') = (\epsilon_n - \lambda)\phi_n(\mathbf{r}, \sigma), \tag{1.36}$$
$$\int d^3\mathbf{r}' \sum_{\sigma'} \tilde{h}(\mathbf{r}\sigma, \mathbf{r}'\sigma')\phi_n(\mathbf{r}', \sigma') = \Delta_n\phi_n(\mathbf{r}, \sigma). \tag{1.37}$$

The eigenvalues $\epsilon_n - \lambda$ and Δ_n represent particle and pairing energies for each shell respectively where λ is acquired from the HFB iteration is already defined in Eq. (1.21). Besides, λ can also be interpreted as the Fermi energy of each channel when the HFB iteration is converged [BD05].

Finally we shall obtain the total energy of a hypernucleus and also density distribution of each nucleons and hyperons. The total energy of a hypernucleus E_{tot} can be calculated by using ϵ_n and Δ_n as

$$E_{tot} = \sum_{i=N,\Lambda} \sqrt{(\epsilon_i - \lambda)^2 + \Delta_i^2}. \tag{1.38}$$

The particle and pairing densities for each state is easily calculated by taking the trace of densities which are already defined in Eq. (1.29):

$$\rho_{N,\Lambda}(\mathbf{r}) = \mathrm{Tr}[\rho_{N,\Lambda}(\mathbf{r}\sigma, \mathbf{r}'\sigma')], \tag{1.39}$$
$$\tilde{\rho}_{N,\Lambda}(\mathbf{r}) = \mathrm{Tr}[\tilde{\rho}_{N,\Lambda}(\mathbf{r}\sigma, \mathbf{r}'\sigma')]. \tag{1.40}$$

In the following chapter, we show the calculated results of single particle

spectrums, densities and binding energies for the selected hypernuclei.

1.4. Concluding Remarks

In the present chapter, we provided theoretical foundations for calculating ground state properties of Λ hypernuclei. On this purpose, we first described a density dependent interaction for NN, NΛ and ΛΛ channels. For NN channel, the SLy5 Skyrme functional is used, while for the NΛ channel we use three functionals fitted from microscopic Brueckner-Hartree-Fock calculations: DF-NSC89, DF-NSC97a and DF-NSC97f. These functionals reproduce the sequence of single-Λ experimental binding energies from light to heavy hypernuclei. For the ΛΛ channel, we used the empirical prescription EmpC which is calibrated on the experimental bond energy in ${}^{6}\mathrm{He}_{\Lambda\Lambda}$ in which, we excluded the high density behavior of the ΛΛ functional due to the lack of experimental information. In order to modelling pairing, we consider a zero range pairing force in the ΛΛ channel, opening the possibility to calculate open-Λ shell nuclei. We also reviewed the current situation about Λ pairing in hypernuclear matter sector where, the Λ pairing gap varies between from 0.5 MeV to 0.75 MeV for the density $\rho_N = \rho_{sat}$ depending on different interactions. It should be reminded that the Λ pairing gap only depends on ρ_Λ related to their k_F according to hypernuclear matter calculations. Finally, we use all these interactions within the Hartree-Fock-Bogoliubov formalism to calculate ground state properties of Λ hypernuclei. In order to that, we extend Hartree-Fock-Bogoliubov computer code (HFBRAD) to hypernuclear sector by introducing NΛ and ΛΛ channels. In addition, our calculations are performed in spherical symmetry since deformation is not expected to increase greatly in the case of pairing correlations. Therefore, we shall consider hypernuclei with proton and neutron closed shells, e.g. ${}^{40-\mathrm{S}}_{-\mathrm{S}\Lambda}\mathrm{Ca}$, ${}^{132-\mathrm{S}}_{-\mathrm{S}\Lambda}\mathrm{Sn}$ and ${}^{208-\mathrm{S}}_{-\mathrm{S}\Lambda}\mathrm{Pb}$, since semi-magicity often guarantees that nuclei remain at, or close to, sphericity.

2

Pairing in Hypernuclei: Results

2.1. An Overview

In the present section, we show predictions for the Λ pairing gap and its impact on multi-Λ hypernuclei. In order to achieve this quest, we first discuss relative gaps between N and Λ single particle energies predicted by HF calculation without the pairing to assert our calculation without NΛ pairing. We then employ Hartree-Fock-Bogoliubov (HFB) framework including pairing in the ΛΛ channel to study binding energies and density profiles in multi-Λ hypernuclei.

2.2. Hunting Clues for the Λ Pairing: Results of the Hartree-Fock Approach

2.2.1 Λ Single Particle Spectrums for Multi-Λ Hypernuclei

Let us first discuss the hypernuclei of interest in this work, without ΛΛ pairing interaction. On this purpose, we investigate closed shell hypernuclei such as ${}^{60}_{20\Lambda}$Ca, ${}^{172}_{40\Lambda}$Sn, ${}^{278}_{70\Lambda}$Pb shown in Fig. 2.1. These nuclei are triply magic.

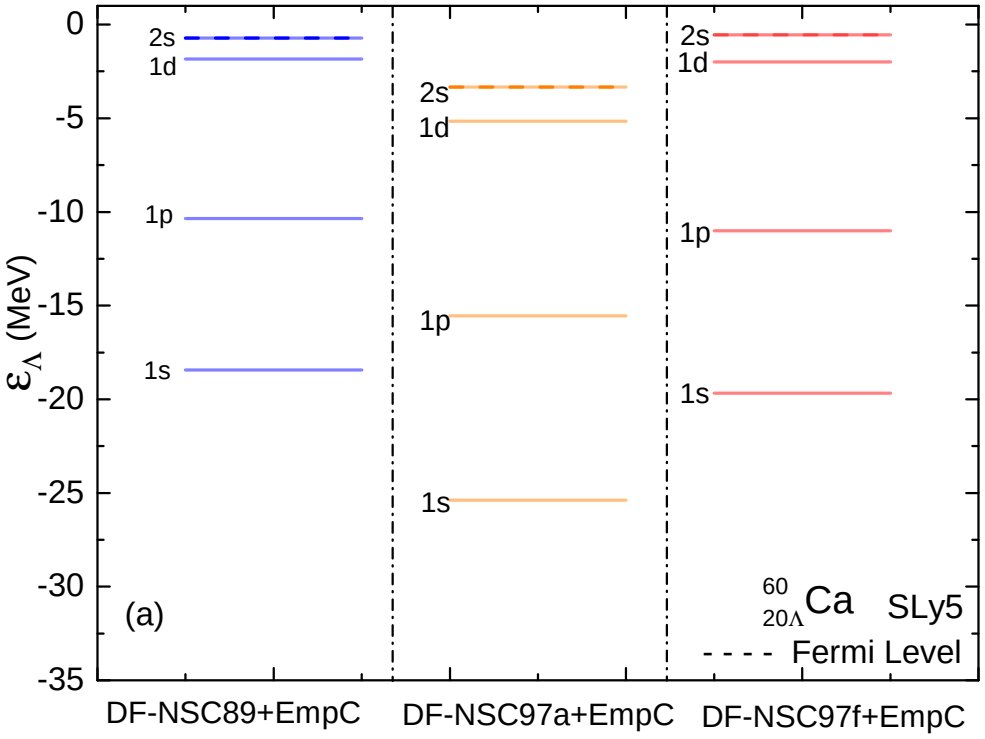
0
-5
-10
-15
-20
-25
-30
-35
ε_Λ (MeV)
2s
1d
1p
1s
2s
1d
1p
1s
2s
1d
1p
1s
(a)
$^{60}_{20\Lambda}$Ca SLy5
Fermi Level
DF-NSC89+EmpC
DF-NSC97a+EmpC
DF-NSC97f+EmpC

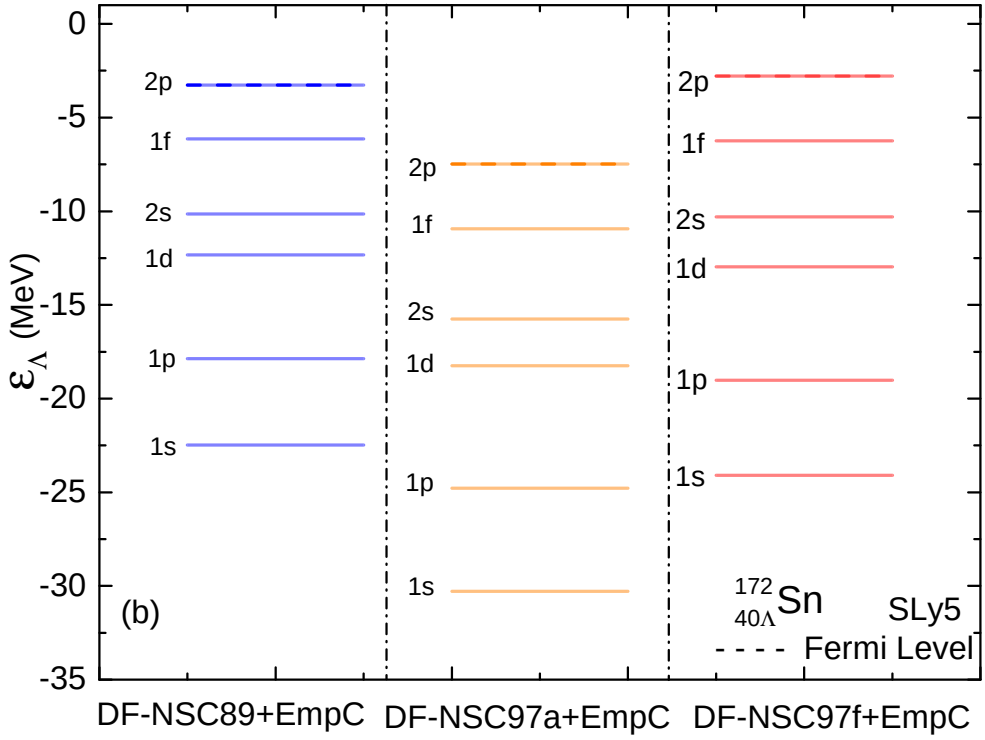
0
-5
-10
-15
-20
-25
-30
-35
ε_Λ (MeV)
2p
1f
2s
1d
1p
1s
2p
1f
2s
1d
1p
1s
2p
1f
2s
1d
1p
1s
(b)
$^{172}_{40\Lambda}$Sn SLy5
Fermi Level
DF-NSC89+EmpC
DF-NSC97a+EmpC
DF-NSC97f+EmpC

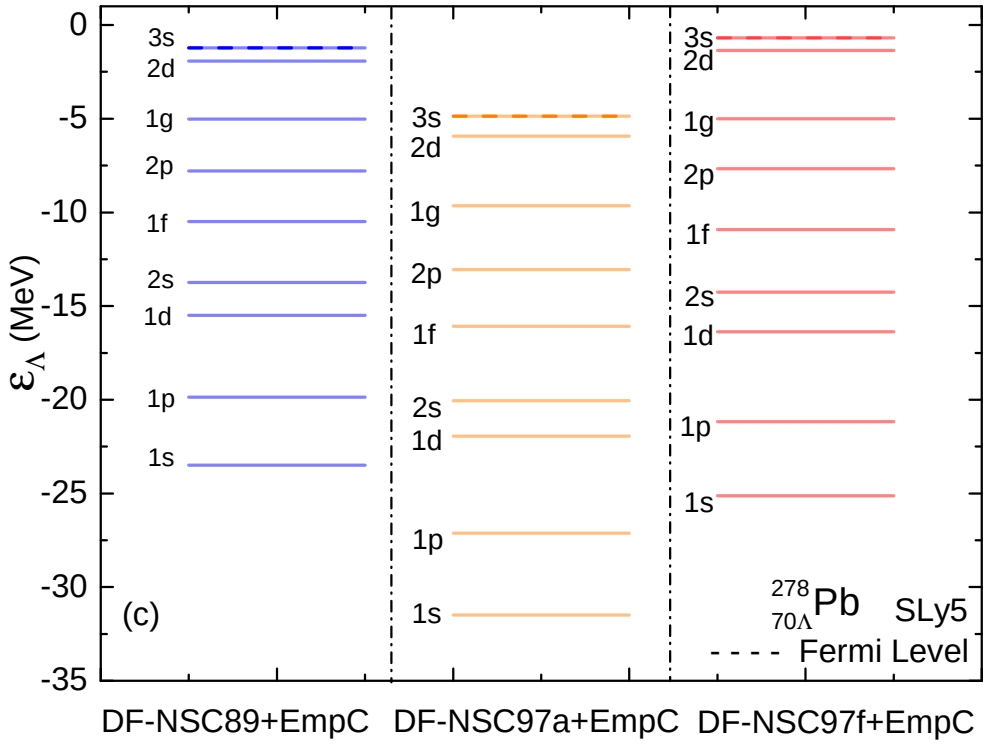

Fig. 2.1: The Λ single particle spectrum $^{60}_{20\Lambda}$Ca (a), $^{172}_{40\Lambda}$Sn (b) and $^{278}_{70\Lambda}$Pb (c) hypernuclei, calculated with the HF approach.

Due to the absence of spin-orbit term, the shell structure of hyperon is also expected to be similar to that of the spherical harmonic oscillator, with magic numbers 2, 8, 20, 40, 70, etc, and the energy gaps are larger than in ordinary nuclei (please see Sec. 1.2 about a discussion for the spin-orbit splitting of hypernuclei). While the central potential is also expected to modify the details of the single particle spectrum, the gross increase of the single particle gap compared to ordinary nuclei, is mostly due to the absence of spin-orbit interaction. New magic numbers in the Λ channel is clearly caused by absence of spin-orbit interaction, increasing the degeneracy of the states as well as the average energy gaps between single particle states. In order to check this statement, we have calculated the single particle spectrum for other Skyrme interactions, e.g. SGII [GS81], SAMI [RMCS12] and SIII [BFGQ75], and we found the same gross conclusions.

The average single particle gaps between two neighboring orbitals can be

Shell	Energy Difference (MeV)		
	${}^{60}_{20\Lambda}$Ca	${}^{172}_{40\Lambda}$Sn	${}^{278}_{70\Lambda}$Pb
1s	6.00	7.50	8.50
1p	6.00	6.87	7.10
1d	3.32	5.80	6.36
2s	2.59	5.57	6.42
1f	-	4.81	6.30
2p	-	4.20	5.20

Tab. 2.1: Energy difference of each shell between DF-NSC97a+EmpC and DF-NSC89+EmpC force sets. The detailed spectra are shown in Fig. 2.1.

estimated from Fig. 2.1, where the Λ spectrum is shown for ${}^{60}_{20\Lambda}$Ca, ${}^{172}_{40\Lambda}$Sn, and ${}^{278}_{70\Lambda}$Pb hypernuclei and for 3 different density functionals in the Λ channel (the Skyrme interaction SLy5 is fixed in the nucleon channel): the average single-particle gap is found to be generally larger than 4 MeV, except for the gap between the 2s-1d and 3s-2d states, where it is between 1 and 3 MeV. These smaller energy gaps may be related to the pseudo-spin symmetry [Gin05, LMZ15], since the 2s-1d and 3s-2d states are pseudo-spin partners. The small energy gap between these states makes them good candidates for pairing correlations: These states could largely mix against pairing correlations when they are close to the Fermi level, represented in dashed lines in Fig. 2.1. For the selected nuclei in Fig. 2.1, the Fermi level is indeed close to either the 2s-1d or the 3s-2d states in the cases of Ca and Pb hypernuclei, respectively.

The energy spectra predicted by DF-NSC89+EmpC and DF-NSC97f+ EmpC are mainly identical, while the single particle states predicted by DF-NSC97a+ EmpC are systematically more bound, since the NΛ potential is deeper for DF-NSC97a+ EmpC compared to the two others functionals [MKG17, KMGR15]. We give a more quantitative estimation of the single particle energy differences between the predictions of DF-NSC97a+EmpC and DF-NSC89+EmpC in Tab. 2.1. As expected, the larger the number of hyperons, the larger the differences. The larger the nucleon density, the larger the differences as well, since the NΛ potential strongly depends on nucleon density. Hence, the difference is larger for the deep single particle states than for the weakly bound ones.

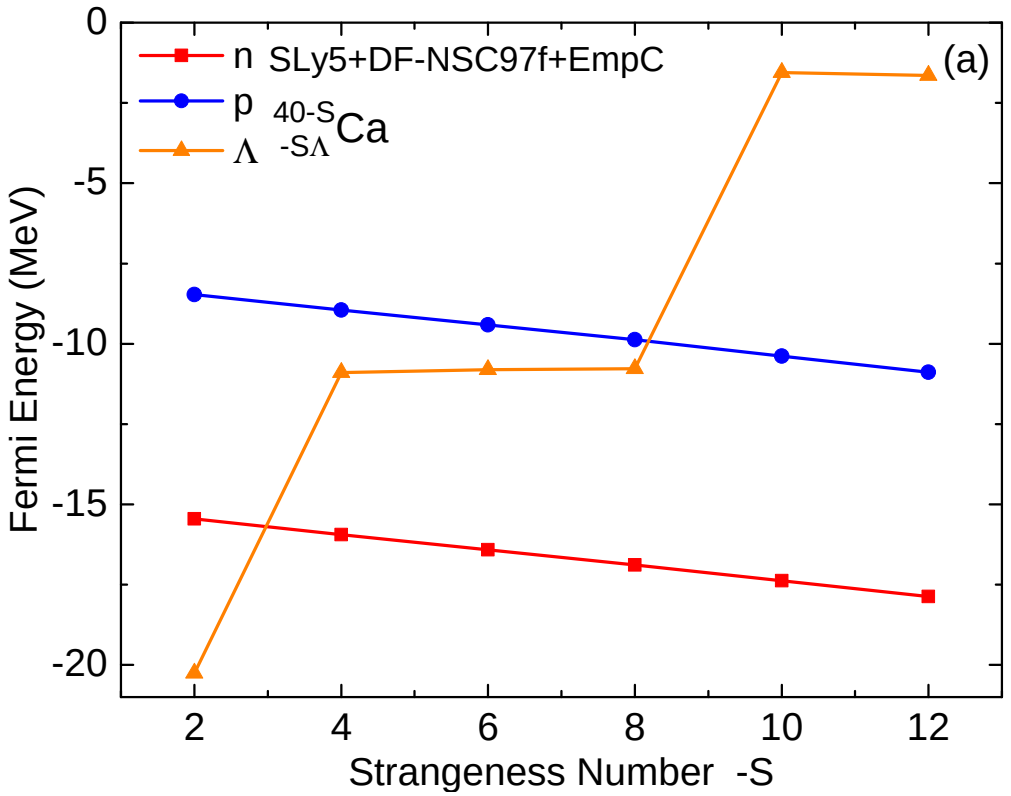
n
p
Λ
SLy5+DF-NSC97f+EmpC
40-S
-SΛ
Ca
(a)
Fermi Energy (MeV)
Strangeness Number -S
0
-5
-10
-15
-20
2
4
6
8
10
12

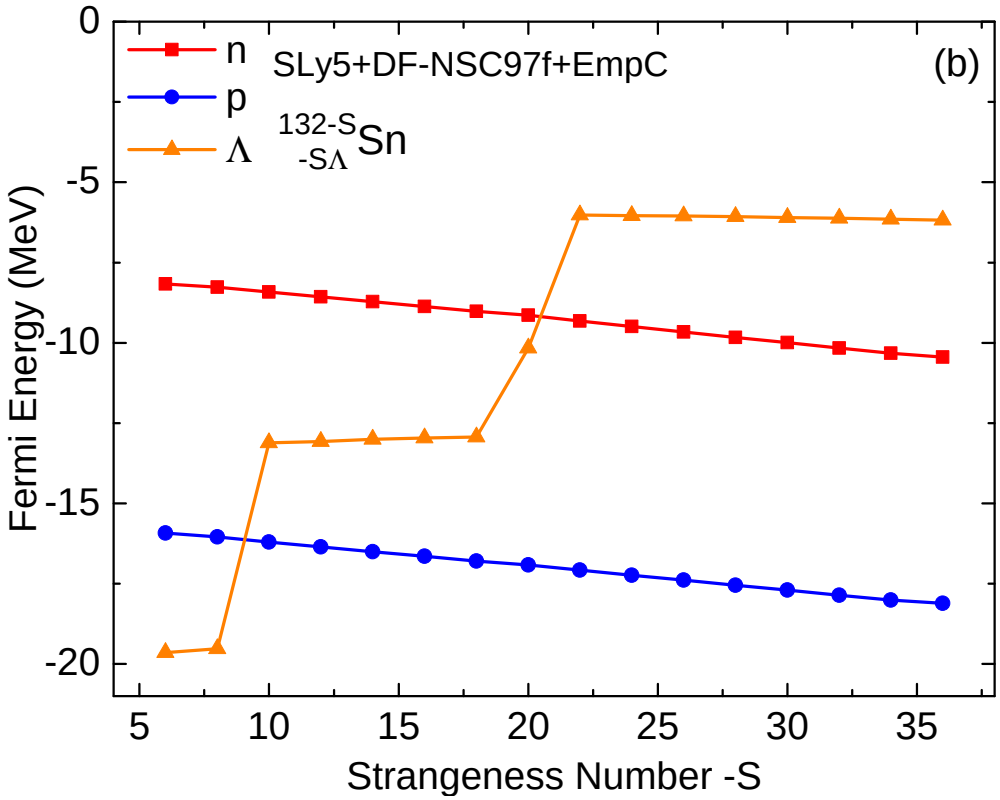
n
p
Λ
SLy5+DF-NSC97f+EmpC
132-S
-SΛ
Sn
(b)
Fermi Energy (MeV)
Strangeness Number -S
0
-5
-10
-15
-20
5
10
15
20
25
30
35

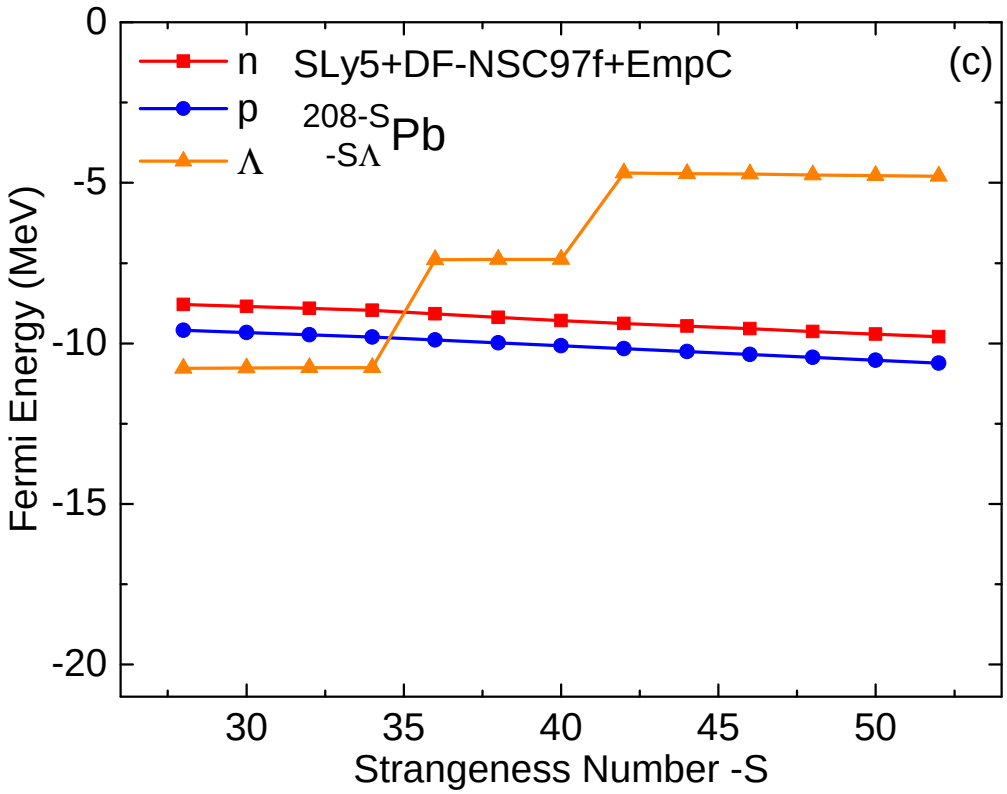

Fig. 2.2: Evolution of proton, neutron and Λ Fermi energies function of strangeness number -S for ${}^{40-S}_{-S\Lambda}$Ca (a), ${}^{132-S}_{-S\Lambda}$Sn (b), and ${}^{208-S}_{-S\Lambda}$Pb (c) hypernuclei with the HF approach.

2.2.2 Possibility of the NΛ Pairing Channel

We now discuss the NΛ and ΛΛ pairing channels. These two pairing channels are expected to compete: a Lambda can be paired either to a nucleon or to another Lambda. Drawing an analogy with $T = 0$ and $T = 1$ pairing channels in ordinary nuclei, the pairing interaction between two different particles ($T = 0$) can occur under the condition of a good matching between their wave functions and also between their single particle energies. This is the main reason why $T = 0$ pairing is expected to appear mainly at (or close to) N=Z nuclei [WFS71, Goo99]. The condition for $T = 0$ pairing channel can be easily guessed by investigating single particle spectrums and Fermi energies with the HF calculation.

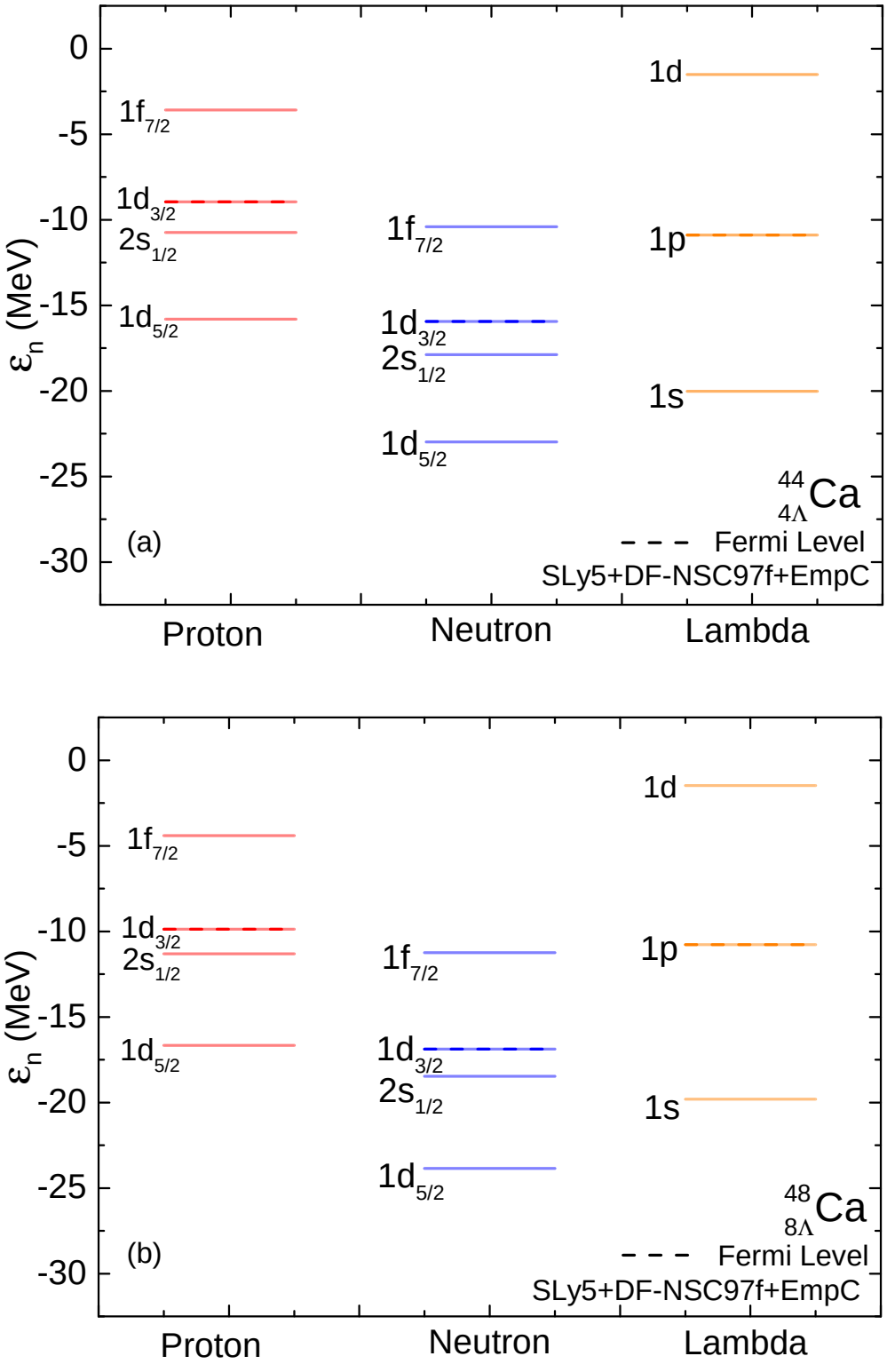

Fig. 2.3: A complete single particle spectrum of ${}^{44}_{4\Lambda}$Ca (a) and ${}^{48}_{8\Lambda}$Ca (b) hypernuclei, calculated with the HF approach.

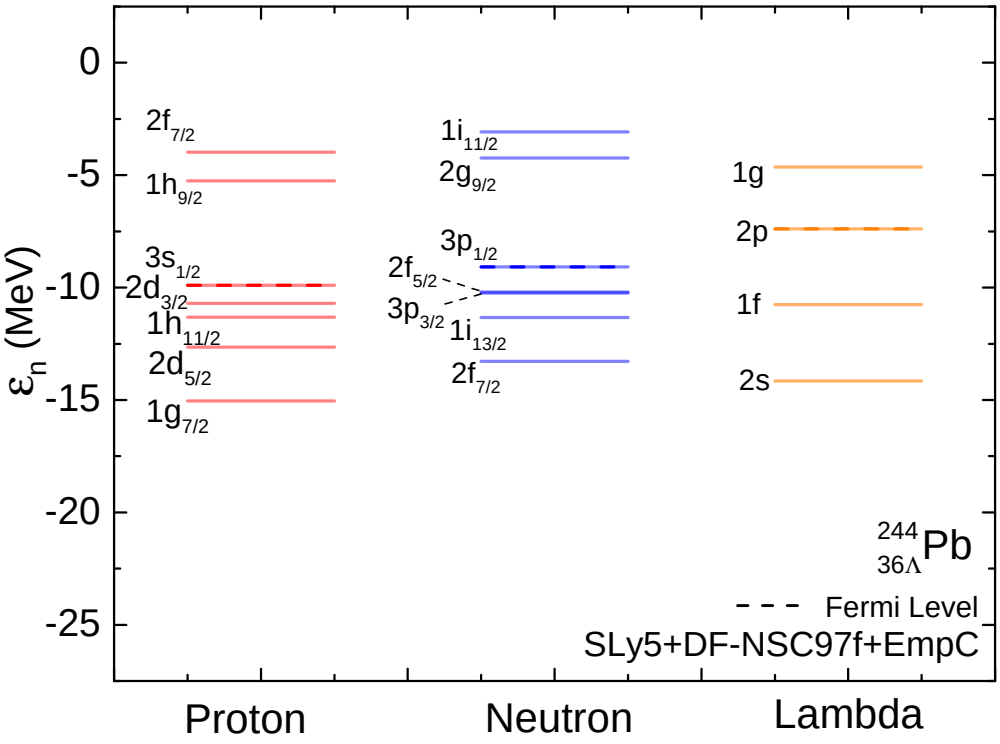

Fig. 2.4: A complete single particle spectrum of ${}^{244}_{36\Lambda}$Pb hypernucleus with the HF approach.

Let us first focus on the NΛ pairing. A necessary condition for this pairing to occur is that the neutron or proton Fermi energy is close to the Λ one. The neutron, proton and Λ Fermi energies are displayed on Fig. 2.2 as function of the strangeness number $-S$ for the three representative nuclei: ${}^{40-S}_{-S\Lambda}$Ca, ${}^{132-S}_{-S\Lambda}$Sn and ${}^{208-S}_{-S\Lambda}$Pb. The intersections of nucleons and Λ Fermi energies occur at $-S = 4$ (neutrons) and 8 (protons) for ${}^{40-S}_{-S\Lambda}$Ca, $-S = 10 - 16$ (proton) and $20 - 32$ (neutrons) for ${}^{132-S}_{-S\Lambda}$Sn and for $-S = 34 - 40$ for both neutrons and protons ${}^{208-S}_{-S\Lambda}$Pb hypernuclei.

Let us now take typical examples of the nuclei which are located at these crossings. ${}^{44}_{4\Lambda}$Ca and ${}^{48}_{8\Lambda}$Ca single-particle levels are shown in Fig. 2.3 and the ones of ${}^{244}_{36\Lambda}$Pb is shown in Fig. 2.4 The Λ Fermi level is mainly the 1p state in ${}^{44}_{4\Lambda}$Ca and ${}^{48}_{8\Lambda}$Ca, and there are no p states in the neutron and proton spectrum around the Fermi energy. The conditions for NΛ pairing are therefore not satisfied for Ca isotopes.

A similar analysis can be made for the Sn isotopes. We also calculated ${}^{142}_{10\Lambda}$Sn, ${}^{152}_{20\Lambda}$Sn and ${}^{156}_{24\Lambda}$Sn hypernuclei for which the proton or neutron and the Λ levels cross. The last occupied Λ states is 1d for ${}^{142}_{10\Lambda}$Sn (resp. 2s for ${}^{152}_{20\Lambda}$Sn and 1f for ${}^{156}_{24\Lambda}$Sn) while the corresponding proton (res. neutron) state is $1g_{9/2}$ (resp. $1h_{11/2}$). Since the orbital quantum numbers do not coincide between the nucleons and the Λ states in the cases where their respective Fermi energies cross, the NΛ pairing is not favored for these Ca and Sn nuclei.

The case of ${}^{208-S}_{-S\Lambda}$Pb hypernuclei is different. Fig. 2.4 displays the single particle spectrum for ${}^{244}_{36\Lambda}$Pb hypernucleus, since the crossing of the nucleon (neutrons and protons) and Λ Fermi levels occurs at around $S = -36$ (Fig. 2.3). Fig. 2.4 shows that the last filled orbits are $3s_{1/2}$ for proton, $3p_{1/2}$ for neutron and 2p for Λ. Since Pb is magic in proton, only neutrons and Λ may be paired. We therefore predict that nΛ pairing may occur for ${}^{208-S}_{-S\Lambda}$Pb hypernuclei and for Λ between $S = -34$ and $S = -40$. For lower or higher values of S, the mismatching of the single particles orbitals does not favor nΛ pairing. Since the level density increases with increasing masses, it is expected the general trend that NΛ pairing may occur more frequently as A increases.

${}^{208-S}_{-S\Lambda}$Pb is a typical case representing heavy hypernuclei. Since the Ξ-instability is expected to occur around $-S = 70$ [MKG17], we can infer that pairing may occur for about 10% of ${}^{208-S}_{-S\Lambda}$Pb isotopes (See Sec. 1.1 for details). This number may be considered as the maximum percentage of heavy hypernuclei where NΛ pairing may occur. This case is therefore predicted to be small due to the amount of hypernuclei where NΛ pairing is possible. In the following, we will avoid the cases where it may occur.

2.3. *Investigating Impacts of the ΛΛ Pairing on Hypernuclei: Results of the Hartree-Fock-Bogoliubov Approach*

2.3.1 *A Fitting Protocol for the ΛΛ Pairing Strength*

We now focus on the ΛΛ pairing and consider the cases of semi-magical hypernuclei, such as ${}^{40-S}_{-S\Lambda}$Ca, ${}^{132-S}_{-S\Lambda}$Sn, and ${}^{208-S}_{-S\Lambda}$Pb. It should be noted that

Tab. 2.2: Pairing strength, Λ density and calculated, averaged mean gap and hypernuclear pairing gap for each force sets.

Force Set	Pairing Strength (MeV fm^3)	ρ_{av} (fm^{-3})	Hypernucleus	Calculated Mean Gap (MeV)	Average Mean Gap (MeV)	Pairing Gap in uniform matter [TMC03] (MeV)
DF-NSC89+EmpC	-139	0.0264	$^{46}_{6\Lambda}$Ca	0.82	0.59	0.42
DF-NSC97a+EmpC	-148	0.0349	$^{46}_{6\Lambda}$Ca	1.04	0.50	0.44
DF-NSC97f+EmpC	-180	0.0241	$^{46}_{6\Lambda}$Ca	0.98	0.49	0.43
DF-NSC89+EmpC	-158	0.0421	$^{160}_{28\Lambda}$Sn	0.84	0.46	0.43
DF-NSC97a+EmpC	-145	0.0499	$^{160}_{28\Lambda}$Sn	0.82	0.45	0.50
DF-NSC97f+EmpC	-180	0.0382	$^{160}_{28\Lambda}$Sn	0.82	0.46	0.45
DF-NSC89+EmpC	-184	0.0400	$^{272}_{64\Lambda}$Pb	0.69	0.44	0.47
DF-NSC97a+EmpC	-180	0.0320	$^{272}_{64\Lambda}$Pb	0.76	0.46	0.45
DF-NSC97f+EmpC	-220	0.0270	$^{272}_{64\Lambda}$Pb	0.71	0.44	0.40

these nuclei are magic in both proton and neutron numbers, which helps most of these hypernuclei to resist against deformation, as in the case of normal hypernuclei. They have however an open shell in the Λ channels.

The Λ pairing strengths, mean gaps and averaged mean gaps of isotopic chains are displayed in Tab. 2.2. The fitting procedure for the ΛΛ pairing is the following: we first remind that the ΛΛ mean-field interaction is calibrated to the ΛΛ bond energy in ^{6}He (Nagara event; see Sec. 1.3.1 for details). We then consider open-shell nuclei and calibrate the average Λ-pairing gap to its expectation from uniform matter calculations. Densities are averaged from r=0.2 fm to 10 fm for each hypernucleus and each force set using HF results for each isotopes (by closing paring channel of HFB calculation). These densities are also averaged over the isotopic chain (ρ_{av}) and it is shown in Tab. 2.2. Fermi momentum corresponding to these densities are calculated as $k_{F_\Lambda} = (\frac{3\pi^2}{2}\rho_\Lambda)^{1/3}$. The density profile of hypernuclear matter calculations [TMC03] which has corresponding Fermi momentum and density fraction allows to extract ΛΛ pairing gap for each hypernucleus for each force sets. In order to find adequate Λ pairing strength ($V_{\Lambda_{pair}}$ in Eq. (1.28)), starting from -50 MeV fm^3 to -300MeV fm^3, we iterated and determined mean gap values for each hypernuclei chain in HFB calculation. For each iteration, the mean gap values are averaged over the isotopic chain until similar values of pairing gaps of hypernuclear matter calculation are obtained. Namely for the ${}^{40-S}_{-S\Lambda}$Ca isotopic chain, the average mean gap was calculated by summing each mean gap of hypernucleus starting from $-S$=6 to $-S$=20 and dividing by the total isotope number. Similarly for the ${}^{132-S}_{-S\Lambda}$Sn (${}^{208-S}_{-S\Lambda}$Pb) isotopes, the average man gap determined between $-S$=18 ($-S$=58) to $-S$=40 ($-S$=70) range. The average mean gaps for each isotopes with each force set is given in Tab. 2.2 which are calculated by averaging over the isotopic chain. It should be noted that this is calculated by taking best Λ pairing strength according to the pairing gap of uniform matter. A small difference between the average mean gap and pairing gap of uniform matter does not crate a measurable difference on hypernuclei properties since pairing gap is rather small. For comparison we also present the calculated mean gap for a selected open shell hypernucleus. As a result, a typical 0.5 MeV gap is obtained in all nuclei, leading to a pairing effect independent of the number of Λ involved.

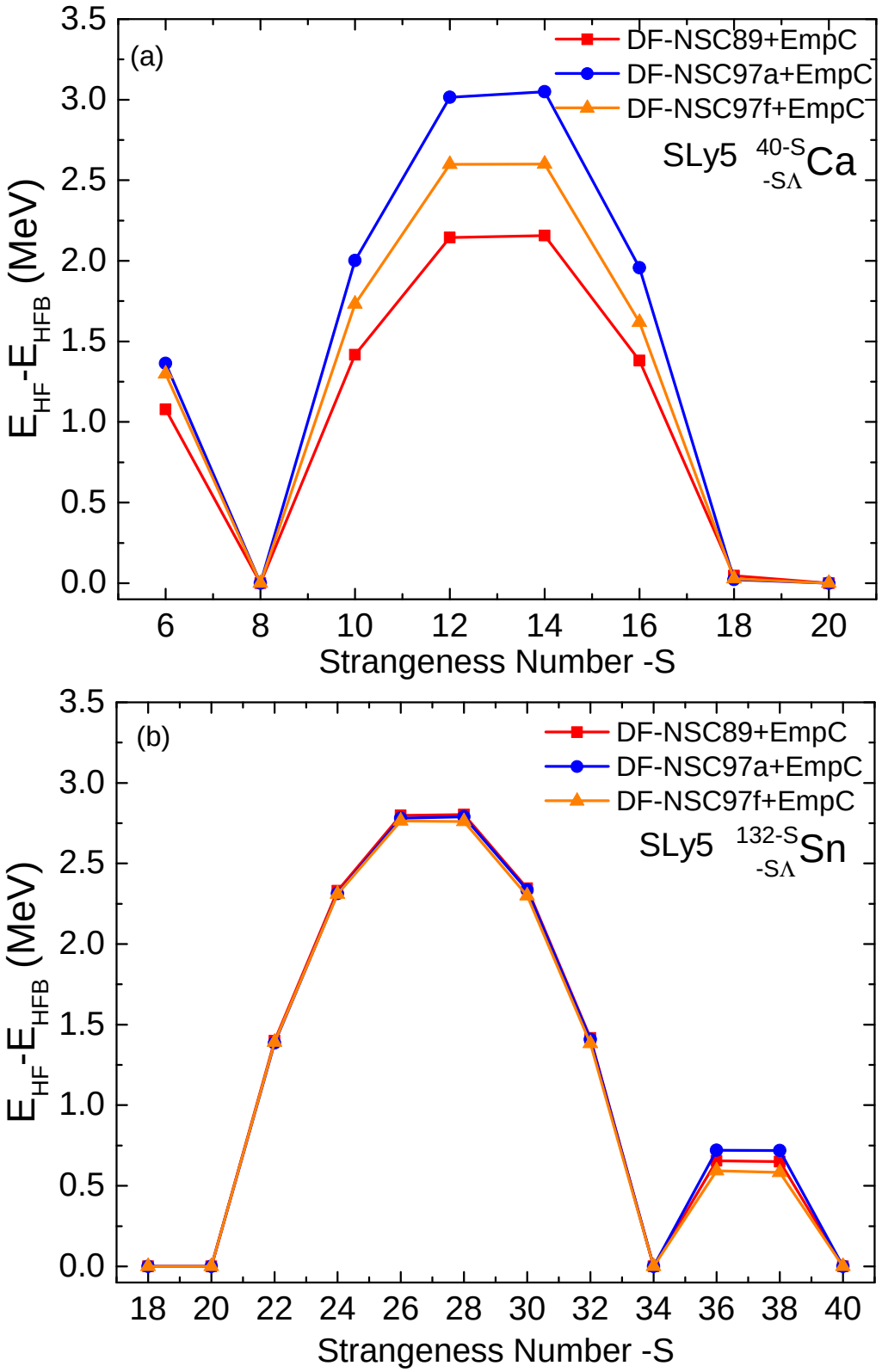

Fig. 2.5: Difference of binding energies between HF and HFB for ${}^{40-S}_{-S\Lambda}$Ca (a) and ${}^{132-S}_{-S\Lambda}$Sn (b) hypernuclei with DF-NSC89+EmpC, DF-NSC97a+EmpC and DF-NSC97f+EmpC force sets.

2.3.2 *The ΛΛ Pairing and Nuclear Binding Energies*

The effect of ΛΛ pairing on the binding energy can be estimated from the condensation energy, defined as $E_{cond} = E_{HF} - E_{HFB}$. The condensation energy measures the impact of the pairing effect on the binding energy. Fig. 2.5 displays the condensation energy for a set of ${}^{40-S}_{-S\Lambda}$Ca and ${}^{132-S}_{-S\Lambda}$Sn semi-magical hypernuclei. As in the case of normal nuclei, the condensation energy evolves as arches, with zero values at closed shells and maximum values for middle-open shells. The condensation energy can reach about 3 MeV in mid-open shell hypernuclei for Ca and Sn isotopes. Since the ΛΛ pairing interaction considered here is calibrated on the maximum prediction for the Λ gap in uniform matter with respect to Λ force sets, the condensation energy represents the estimation of the maximum value for the condensation energy generated by ΛΛ pairing interaction. Besides, the Λ numbers at which condensation energy is zero signs the occurrence of the shell closure. It is therefore not surprising to recover the magical numbers 8, 20, 40, as we previously discussed. Strong sub-shell closure occurs for Λ=34 in Sn isotopes corresponding the filling of the 1f state.

Investigating the effect of ΛΛ pairing on the single particle energies, it turns out to be weak: states around the Fermi level are shifted by about 100-200 keV at maximum. The impact of Λ pairing on single particle energies remains therefore rather small.

2.3.3 *The ΛΛ Pairing and Nuclear Densities*

We now discuss the effect of ΛΛ pairing on both normal and pairing densities. Fig. 2.6 shows normal density profiles for ${}^{40-S}_{-S\Lambda}$Ca, ${}^{132-S}_{-S\Lambda}$Sn and ${}^{208-S}_{-S\Lambda}$Pb series of hypernuclei. For the ${}^{40-S}_{-S\Lambda}$Ca series we consider cases where the NΛ pairing is not expected to occur. As mentioned above, the 1d and 2s states are almost degenerate, and can largely mix due to pairing correlations. Namely, before the 1d orbital is completely filled, Λ hyperons start to fill the 2s state due to the pairing interaction, resulting in a small increase at the centre of the hypernucleus which corresponds the effect of the s state. Similar results can be seen on the density profile of ${}^{208-S}_{-S\Lambda}$Pb hypernucleus: Before the 2d state is completely filled, Λ hyperons start to fill the 3s state

due to the pairing interaction resulting from the almost degeneracy of the 2d and 3s Λ-states. In the case of ${}^{132-S}_{-S\Lambda}$Sn, there is no major difference on density profiles: because of the large gap between 1f and 2p states, the Λ pairing changes only the total energy of the ${}^{132-S}_{-S\Lambda}$Sn isotopic chain in $-S$=24 to $-S$=30 zone but does not impact the occupation numbers of 1f and 2p orbitals.

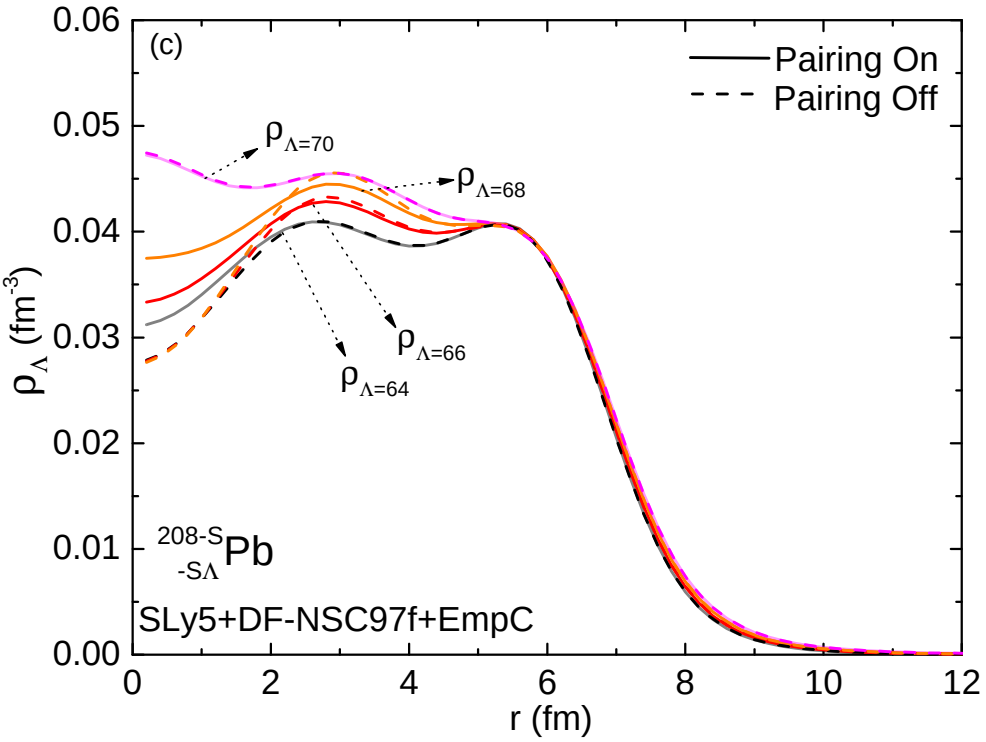

Fig. 2.6: Normal density profiles with on/off pairing for ${}^{40-S}_{-S\Lambda}$Ca (a), ${}^{132-S}_{-S\Lambda}$Sn (b), and ${}^{208-S}_{-S\Lambda}$Pb (c) hypernuclei, calculated with the HFB approach.

Fig. 2.7 displays the Λ pairing density for ${}^{40-S}_{-S\Lambda}$Ca, ${}^{132-S}_{-S\Lambda}$Sn and ${}^{208-S}_{-S\Lambda}$Pb. As mentioned above, pairing interaction effects result in the partial occupation of Λ hyperons in the s and d states. The pairing density of ${}^{54}_{14\Lambda}$Ca hypernucleus peaks at 3 fm due to half-filled 1d orbital. As strangeness number increases, hyperons start to fill the 2s state and the contribution of the 1d state decreases. For $-S$=18, Λ hyperons starts to largely fill the 2s state before the 1d state is completely full, resulting in a pairing density having non-negligible contributions of both s and d states. Similar result

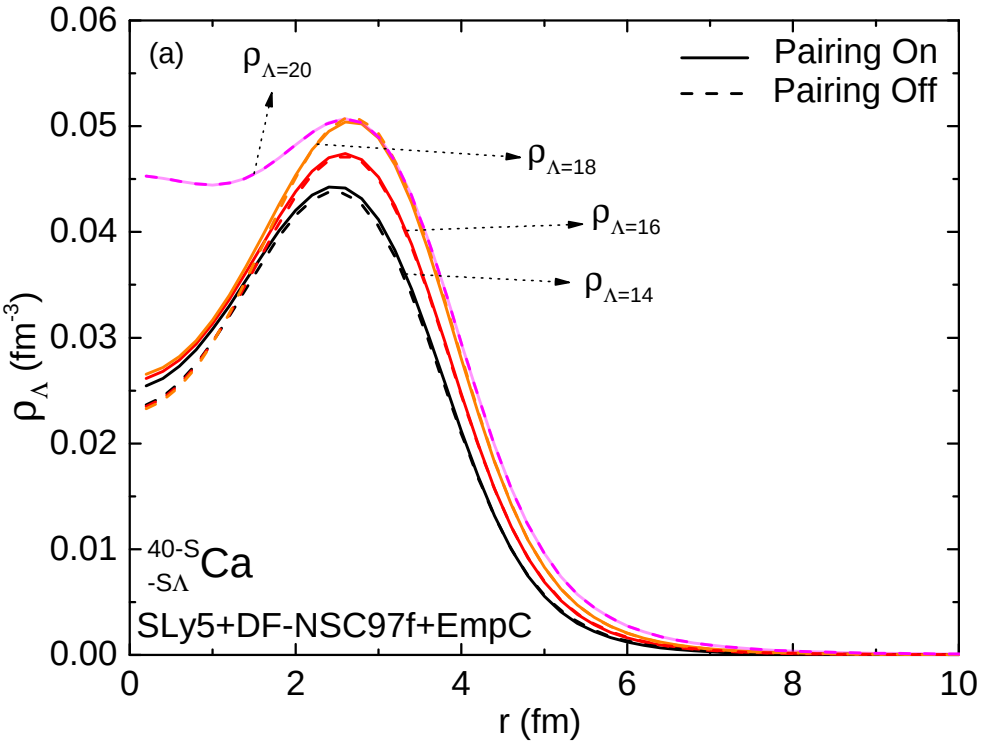
(a)
ρΛ=20
ρΛ=18
ρΛ=16
ρΛ=14
Pairing On
Pairing Off
40-SΛ Ca
SLy5+DF-NSC97f+EmpC
ρΛ (fm-3)
r (fm)
0.00
0.01
0.02
0.03
0.04
0.05
0.06
0
2
4
6
8
10

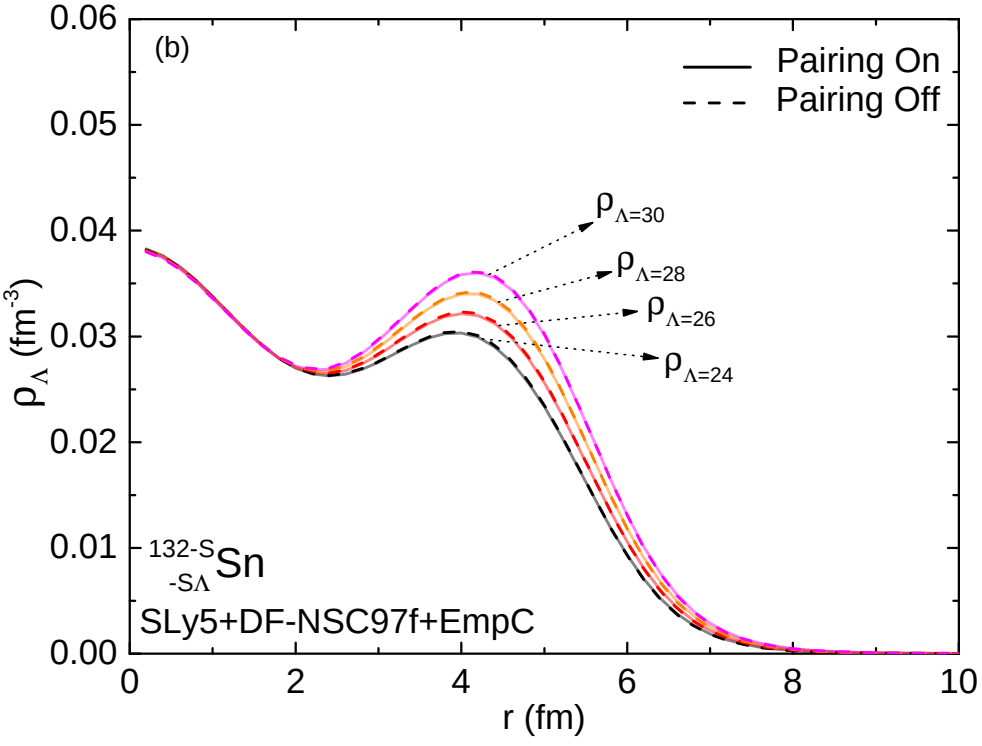
(b)
ρΛ=30
ρΛ=28
ρΛ=26
ρΛ=24
Pairing On
Pairing Off
132-SΛ Sn
SLy5+DF-NSC97f+EmpC
ρΛ (fm-3)
r (fm)
0.00
0.01
0.02
0.03
0.04
0.05
0.06
0
2
4
6
8
10

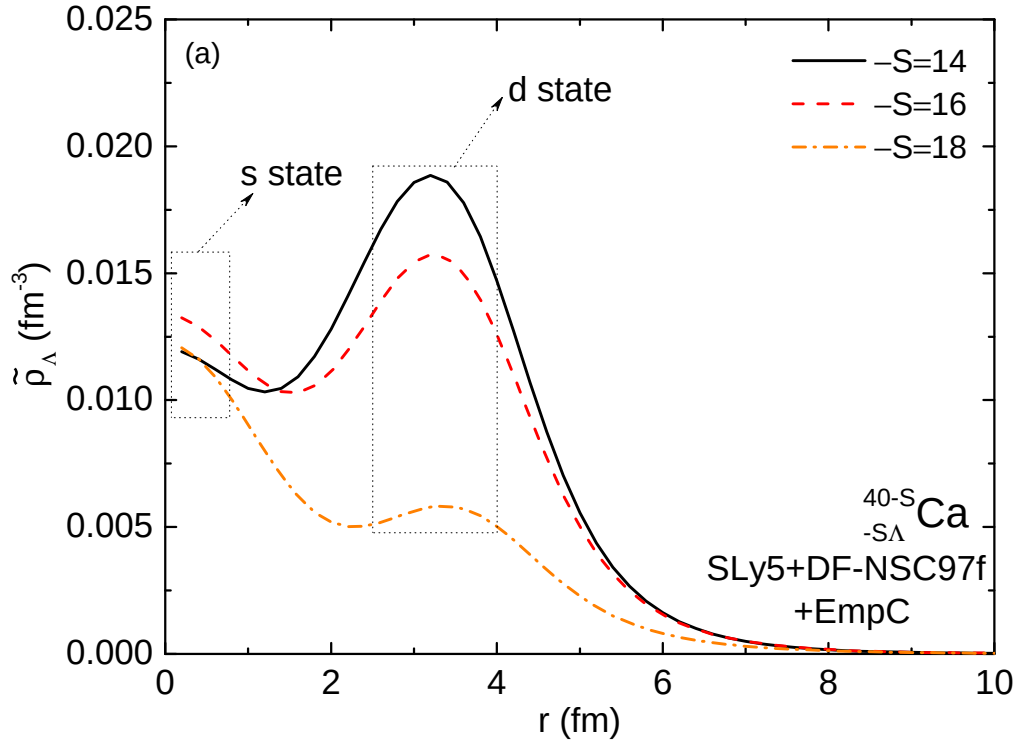
(a)
–S=14
–S=16
–S=18
d state
s state
$^{40\text{-}S}_{\text{-}S\Lambda}$Ca
SLy5+DF-NSC97f
+EmpC
$\tilde{\rho}_\Lambda$ (fm^{-3})
r (fm)
0.025
0.020
0.015
0.010
0.005
0.000
0
2
4
6
8
10

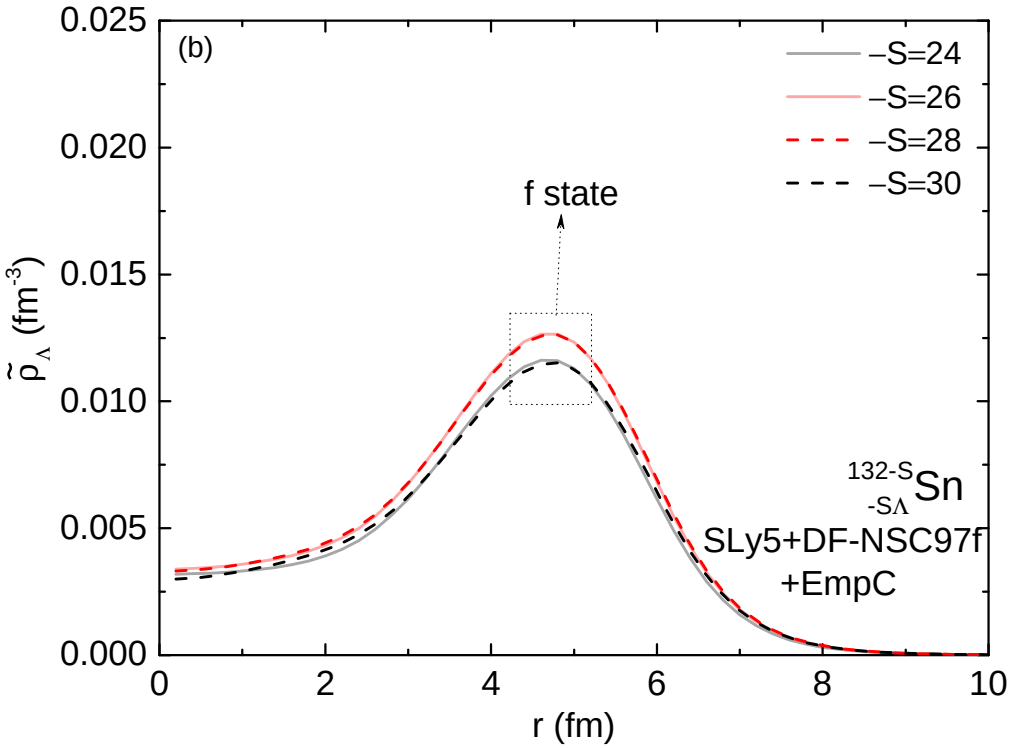
(b)
–S=24
–S=26
–S=28
–S=30
f state
$^{132\text{-}S}_{\text{-}S\Lambda}$Sn
SLy5+DF-NSC97f
+EmpC
$\tilde{\rho}_\Lambda$ (fm^{-3})
r (fm)
0.025
0.020
0.015
0.010
0.005
0.000
0
2
4
6
8
10

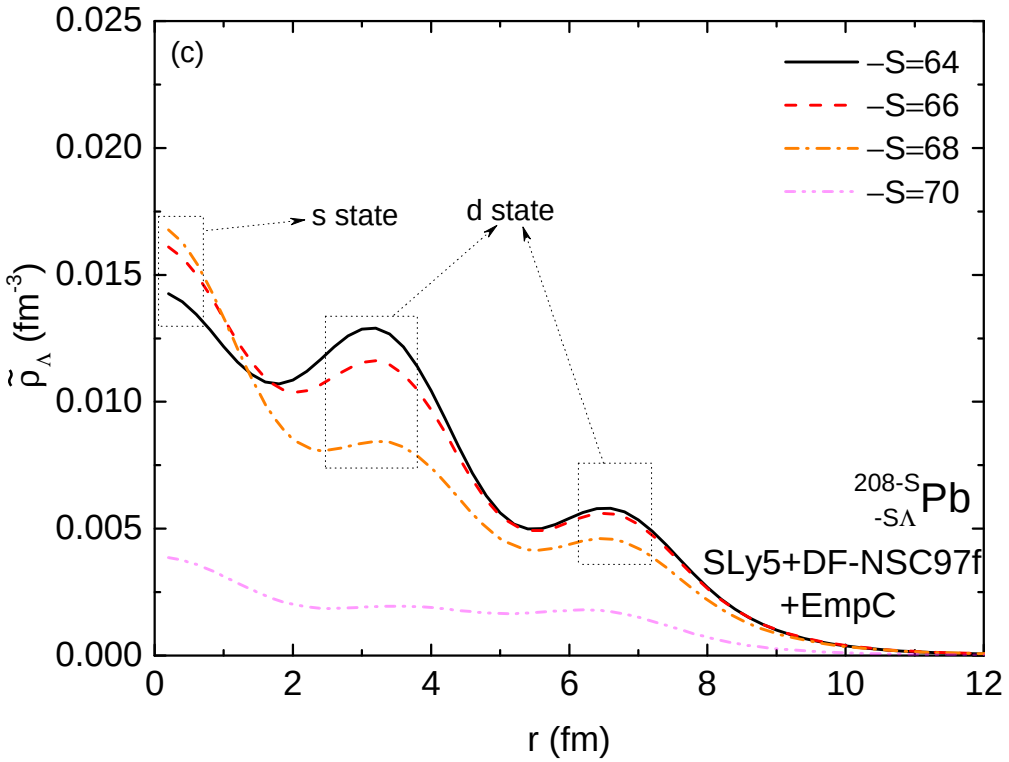

Fig. 2.7: Λ pairing densities for ${}^{40-S}_{-S\Lambda}$Ca (a), ${}^{132-S}_{-S\Lambda}$Sn (b), and ${}^{208-S}_{-S\Lambda}$Pb (c) hypernuclei, calculated with the HFB approach.

can be seen for the pairing density of ${}^{208-S}_{-S\Lambda}$Pb hypernuclei which has 2d-3s coupling. At $-S$=64, pairing densities are mainly built from the 2d state but as the strangeness number increases, the pairing of 2d orbital decreases while pairing density at 3s state increases. However for ${}^{132-S}_{-S\Lambda}$Sn hypernuclei, the situation is different. Due to the large energy gap between 2s and 1f states, the pairing interaction does not change the occupation of these states. For this reason, the pairing density is only built from the 1f orbital and its magnitude increases when the occupation of the 1f orbital increases until it is half-filled. When the 1f state is more than half-filled, the magnitude of the pairing density starts to decrease. The spatial distribution of pairing effect in hypernuclei is therefore expected to exhibit strong variations from one hypernucleus to another, because of the weak spin-orbit effect, giving rise to well separated sets of states.

2.4. Concluding Remarks

In the present chapter, we first investigated the shell structure of ${}^{40-S}_{-S\Lambda}$Ca, ${}^{132-S}_{-S\Lambda}$Sn and ${}^{208-S}_{-S\Lambda}$Pb hypernuclear chain with using HF approach to discuss the NΛ pairing. It is seen that since the energy difference between the N and Λ Fermi levels are usually large (more than 5 MeV) in the considered hypernuclei, the NΛ pairing is quenched in most of the cases. An exception however is ${}^{208-S}_{-S\Lambda}$Pb hypernuclear chain. There is a match between $S = -34$ and $S = -40$ for neutron and Λ Fermi energies which means that neutron-Λ pairing may occur for the related interval. We can infer that pairing may occur for about 10% of ${}^{208-S}_{-S\Lambda}$Pb isotopes. Besides, the expected general trend is that NΛ pairing may occur more frequently as A increases because the level density increases with increasing masses. However, since the Ξ-instability could limit the maximum number of Λ around $-S = 70$, the amount of hypernuclei where NΛ pairing is possible, is therefore predicted to be small.

We then used the HFB approach on same hypernuclei. A $\Lambda\Lambda$ pairing interaction is therefore introduced, which magnitude is calibrated to be consistent with the maximum BCS predictions for the Λ pairing gap in hypernuclear matter. The impact of $\Lambda\Lambda$ pairing on the binding energies, density profiles and single particle energies have been analyzed for ${}^{40-S}_{-S\Lambda}$Ca, ${}^{132-S}_{-S\Lambda}$Sn and ${}^{208-S}_{-S\Lambda}$Pb chains. We have shown that the effects of the $\Lambda\Lambda$ pairing depends on hypernuclei. At maximum, the condensation energy in these chains is about 3 MeV. Density profiles reflect the occurrence of almost degenerate states in the Λ single particle spectrum, such as for instance the almost degeneracy between the 1d and 2s states in ${}^{40-S}_{-S\Lambda}$Ca hypernuclei and 2d and 3s almost-degeneracy in ${}^{276}_{68\Lambda}$Pb. The effects of the Λ pairing also depend on the NΛ and $\Lambda\Lambda$ force sets, but we found only a small overall impact. Generally, we found that $\Lambda\Lambda$ pairing could be active if the energy gap between orbitals is smaller than 3 MeV. Under this condition, Λ pairing could impact densities and binding energies. Since only a weak spin-orbit interaction is expected in the Λ channel, Λ states are highly degenerated and usually distant by more than 3 MeV in energy. In conclusion, the present microscopic approach shows that the Λ-related pairing effect can usually be neglected in most of hypernuclei, except for hypernuclei which have a single particle gap lower than 3 MeV around the Fermi level.

Part II

NEUTRON STARS

3

Neutron Stars: Foundations and Constraints

3.1. Prologue: A Dying Star

An ordinary star is at a delicate balance between the gravitation and the pressure caused by thermonuclear reactions. Since the fusion of light nuclei into ever increasing heavier elements terminates abruptly with the synthesis of the iron-group elements (mostly ^{56}Fe) that are characterized by having the largest binding energy per nucleon, the ^{56}Fe accretion continues at the core of the star as long as the temperature high enough to reach nuclear ^{56}Fe stage. Once, ^{56}Fe accretion at the core reaches the Chandrasekhar limit ($1.44M_{\odot}$) or its temperature not high enough to ignite the next burning stage, the gravity starts to win and the collapse begins [HFW+03, JLM+07]. If the mass of star is greater than $9M_{\odot}$, the ^{56}Fe scenario happens and during the collapse, the star goes into the supernova phase [JLM+07]. However, if it has a smaller mass than $9M_{\odot}$, its temperature cannot support the thermonuclear reactions and the star will turn to a red giant where ^{56}Fe synthesis will not be started due to the lack of the gravitational compression [HFW+03]. In both cases, the thermonuclear reaction inside the core is slowed and eventually stopped. Since the thermonuclear reaction is the only source of pressure

to counterbalance the gravity, the gravity starts to compress the interior of the star. First solid state forces try to stop gravity, however it is not enough: electrons start to be compressed by gravity while they resist placing at same quantum state due to their fermionic nature. This is called electron degeneracy pressure [HPY07].

If the electron degeneracy pressure is large enough to stop the gravity, the dying star core becomes a white dwarf [HPY07, Boo07, MTW73]. This is a typical end for red giants. However, if the ^{56}Fe accretion reach the Chandrasekhar limit ($1.44 M_{\odot}$), it undergoes a supernova where the degeneracy pressure of the electrons is not large enough to stop the gravity. Therefore, electrons start to get close from each other and their wavelength become of the order of fm, with an increased Fermi momentum allowing for appearing electrons near or inside of the nucleus at high pressure. This starts a massive electron capture process:

$$p + e^{-} \longrightarrow n + \nu \tag{3.1}$$

Because of electron capture, there is also a β decay:

$$n \longrightarrow p + e^{-} + \bar{\nu} \tag{3.2}$$

Consequently, $^{56}_{26}$Fe turns to $^{62}_{28}$Ni by electron capture process and subsequent β decay (for instance, 62 $^{56}_{26}$Fe nuclei create 56 $^{62}_{28}$Ni nuclei with the help of highly energetic degenerate electrons due to the gravity) then to a heavier neutron rich nucleus $^{122}_{39}$Y and it continues to heavier nuclei with an increased neutron fraction [MTW73]:

$$^{56}_{26}\mathrm{Fe} \overset{\text{Gravity}}{\longrightarrow} {}^{62}_{28}\mathrm{Ni} \overset{\text{Gravity}}{\longrightarrow} {}^{122}_{39}\mathrm{Y} \overset{\text{Gravity}}{\longrightarrow} ..... \overset{\text{Gravity}}{\Longrightarrow} \text{Nuclear Matter} \tag{3.3}$$

This process is also modified by strong interactions of nuclear medium due to the distance between nuclei becomes comparable distance between nucleons. Since the driving force is the work done by the compression due to the gravity, it continues until the gravity is counterbalanced: nuclear matter could stop the collapse due to its incompressibility. If then, accelerated particles during collapse will bounce from the nuclear matter core and create a shockwave which triggers a supernova explosion [JLM+07]. Consequently, the matter outside of the core is ejected to the interstellar medium. The remaining

neutron rich, hot and dense nuclear matter in the core forms an object named Neutron Star.

3.2. Neutron Stars: General Properties

Neutron stars (NS) are one of the most interesting objects in universe. They have a typical mass $M = 1 - 2M_{\odot}$, where $M_{\odot} = 2 \times 10^{33}$ g is the solar mass, and a radii $R = 10 - 14$ km [HPY07, Boo07, MTW73, RPJ+18]. Their place between white dwarfs and black holes on the same stage of stellar evolution, makes them a very charming object to understand the exotic phases of matter. While experiments in finite nuclei probe densities around saturation density of nuclear matter ($n_{\rm sat} \approx 0.16 {\rm fm}^{-3}$, $\rho_{\rm sat} \approx 2.7 \times 10^{14}$ g/cm^3) and heavy-ion collisions explore a wider domain of densities with small isospin asymmetries, NSs are the solely system to explore the equilibrium properties of dense matter at densities well above saturation density, and with large isospin asymmetries (Note that instead of Ch. 1 and Ch. 2, we used n for the particle density and ρ for the matter density.) [RPJ+18].

From the astrophysical side, the observation of NSs allows to set limits on the maximum mass which also affects the maximum observable density of stable baryonic matter. The maximum mass of neutron stars, which is yet not well-determined, fixes the mass boundary between NSs and black holes, which give clues on the understanding of supernova core-collapse mechanism [JLM+07] as well as of the fate of NS mergers as kilonovae [Met17]. The observed masses vary from $1.174(4)M_{\odot}$ [ÖF16, FPE+16] to about $2M_{\odot}$ [AFW+13, ÖF16] and the centroid value is 1.4 $M_{\odot}$ [ÖF16]. The well established upper mass limits are: $1.908(16)M_{\odot}$ for PSR J1614-2230 [ABBS+18] and $2.01(4)M_{\odot}$ for PSR J0348+0432 [AFW+13]. Nowadays, widely accepted observed maximum mass of NS is ($M^{obs}_{max} = 2.01(4)M_{\odot}$) [AFW+13]. Recently, two new observations have raised up the upper limit to $M_{max} = 2.14^{+0.10}_{-0.09}M_{\odot}$ from Shapiro delay (which is an observable when a stellar object passes behind its companion during the orbital motion, creates a small delay in pulse arrival times induced by the curvature of space-time in the vicinity of the companion star) associated to the MSP J0740+6620 [CFR+19] and $M_{max} = 2.27^{+0.17}_{-0.15}M_{\odot}$ from magnesium lines associated to the "redback" PSR J2215+5135 [LSC18].

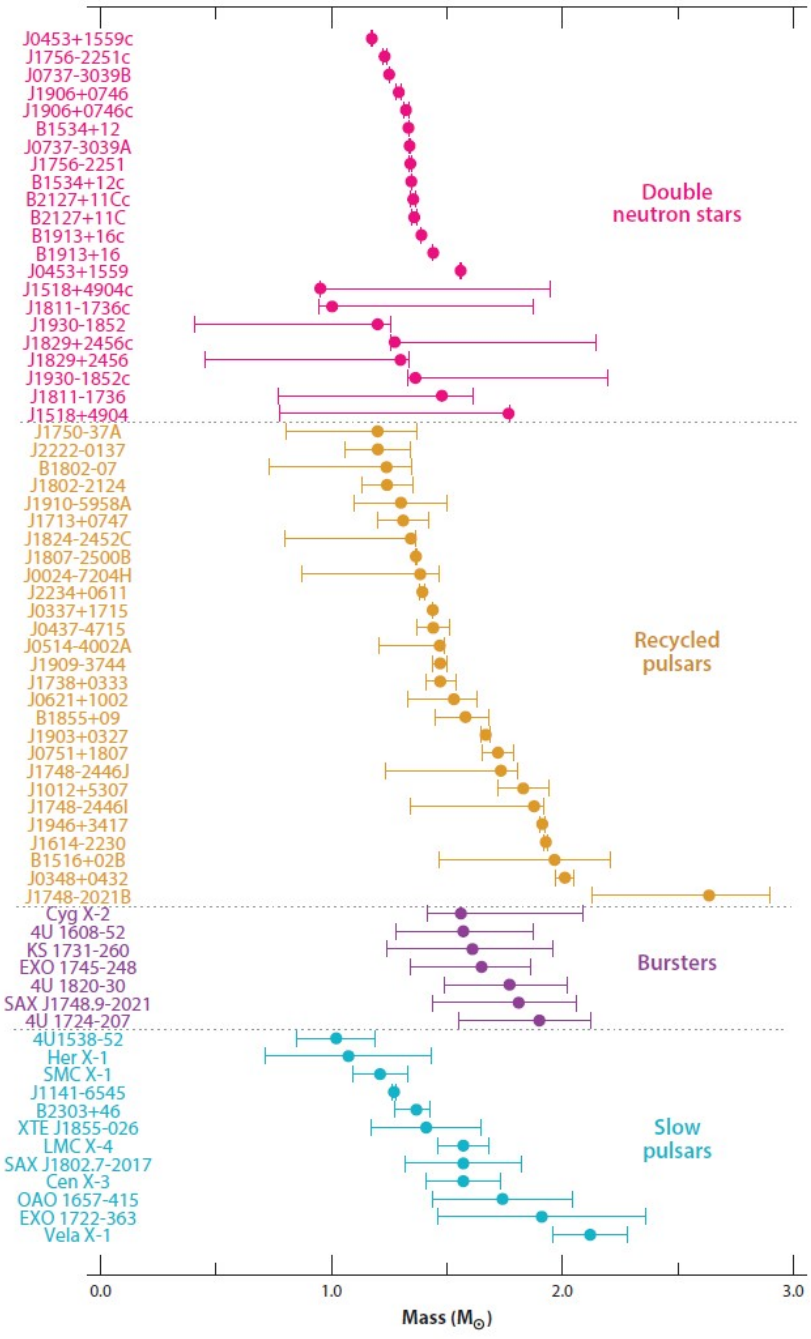

Fig. 3.1: Observed NS masses from Ref. [ÖF16]

Unlike mass, radii observations from NS thermal emission or X-ray burst is not very accurate [SLB10, LS14, ÖF16, ÖPG+16, ROP16, MDDS+18, dGM+19]. A clear understanding of the composition of the atmosphere, the magnetic field, the NS spinning as well as the density of the interstellar medium is however necessary to get reliable estimation of the NS radius [ÖF16]. Model dependence on equation of states is also an important source of uncertainties since it was shown that it can shift radii up to 2 km [MDDS+18]. Eventually, the predicted radii from the X-ray observations for $M = 1.4M_\odot$ is in the $9.8 - 11$ km range. However, it could also be as small as $R_{1.4} = 8.9^{+1.7}_{-1.0}$ km from Ref. [MDDS+18] or as large as $R_{1.4} = 12^{+0.66}_{-0.45}$ km from Refs. [SLB10, LS14]. In a recent work, a semi-agnostic meta-model was directly injected in the analysis of the thermal emission from 7 qLMXB [dGM+19]. The constant radius approximation of Ref. [GSWR13] was also performed with the new data, providing a radius of about $R_{NS} = 11.06 \pm 0.4$ km. Injecting constraints from nuclear physics and neglecting possible phase transitions in dense matter, the radius of a $1.4M_\odot$ NS is predicted to be $R_{1.4} = 12.4 \pm 0.4$ km. The observation of a NS with a lower radius would clearly indicate a softening of the EoS induced by new degrees of freedom which are not contained in our nuclear physics meta-modeling.

Now let us start to give some technical details. Since NS are formed from the balance between pressure and gravity, it is fundamental to define a term named as equation of state (EoS). This "EoS" represents the dependence of the pressure P on energy density ε (depending on baryonic density $\varepsilon = (m_b c^2 + e)n$ where m_b mass of baryons, e is energy per particle and n baryon number density) ε is source of gravity, and P is governed by the interactions between the particles. Approximately 50-100 years after the explosion, NS reaches a thermal equilibrium between the core and the crust in which its core temperature is around $0.03 - 0.12$ MeV [LP07]. Temperature T therefore can be neglected on EoS at first order. The model dependance comes from $P(\varepsilon)$ and the related interactions. Indeed, theoretical predictions of models and interactions from nuclear physics cannot accurately constrain observational measurements. More precisely, the extrapolations to $\rho = 2 - 10\rho_{\rm sat}$ is still under discussion (where ρ is the matter density and $\rho_{\rm sat} = 2.7 \times 10^{14}$ g/cm^3 is the nuclear saturation density) since the behavior of EoS for $\rho \geq \rho_{\rm sat}$ is not known from nuclear experiments. Therefore, more precise observations

are needed to understand the high density behavior of the EoS. The small summary about models derived from nuclear physics is given in Sec. 3.3.

Another debated topic about the high density behavior of NS EoS is the phase transition. For densities above $\rho \sim 3\rho_{sat}$, new degrees of freedom could appear, such as pion condensation [HP82, FKLS92, YSZ+18], hyperonization [Gle87, CS13, MKV15, CV16, FAPVn17, GCS19] or phase transition to quark matter [Ito70, BC76, CN76, KK76, ZH13, AHP13, HS19, MTHR19, MR19]. In general the occurrence of new degrees of freedom tends to soften the EoS, and thus reduce the radius, except in the case of the quarkyonic model, which describe the transition to quark matter as a crossover [MR19]. However, the softening is smaller at second order phase transition such as hyperonization and pion condensation compared to first order one such as quark matter. In addition, it is also possible to consider pion condensation as a first order phase transition, which dramatically softens the NS EoS (see Ref. [HP82] for details). A recent article (Ref. [YSZ+18]) discuss the possibility for pion condensation in nuclear medium by extracting Landau-Migdal parameters from Gamow-Teller transitions of ^{132}Sn to ^{132}Sb. However, the effect of pion condensation on EoS is predicted to be negligible from nuclear matter calculations due to the low energy gap of superconductivity and therefore it has a least concern at first order [FKLS92]. Other kind of phase transitions are now subject of debate: Hyperonization and quark matter. At large densities, a substantial population of hyperons are expected because the Fermi energy of neutrons becomes of the order of rest mass of hyperons, leading to an increase of the hyperon fraction, but it also reduces the degeneracy pressure inside the NS, leading to soft NS EoS at high densities. The softening of the EoS also reduces the maximum mass, and therefore the observation constraint for M_{max}^{obs} could be crucial for the EoS selection. This is often referred as the hyperonization issue [CS13, MKV15, CV16, GCS19]. On the other hand, phase transition to deconfined quark matter could also soften the NS EoS without breaking down the M_{max}^{obs} constraint, if the speed of sound in dense quark matter is fixed to a large value (above the conformal limit of $C_{s,\infty}^2 = 1/3$ [AKV10]) [BS15, TMR18, TMR19].

3.3. A New Constraint: GW170817

As reviewed in previous discussion, the precision of observational mass/radii measurements is not enough to determine NS EoS, while nuclear experiments are only constraining the densities around saturation densities which is far from the densities of NSs ($\rho = 3 - 10\ \rho_{\rm sat}$). Therefore, the extrapolation of these models are indeed inside the observational margins but not enough for an accurate definition of interior structure. However, there is an additional constraint which is directly connected to the interior structure of NS: Tidal deformability [Hin08, FH08, DN09]. During the in-spiral, two NS in a binary emit gravitational wave while dancing with each other and during that process, each of them is deformed due to the tidal gravitational field created by their companion. The emitted gravitational waves can be understood as a composition of two different parts: The orbital motion of each individual mass and the quadrupole response of the tidal gravitational field. The quadrupole part is important since it includes geometry/distribution of mass (energy) inside the NSs. In other words it is directly connected to the NS EoS. This kind of effect is characterized by the tidal deformability ($\tilde{\Lambda}$) which will be detailed in Sec. 3.7.

In 2017, the first gravitational waves (GW) from a binary NS merger (GW170817) have been detected by the LIGO-Virgo collaboration [AAA+17, AAA+19], providing an estimation of the NS tidal deformability $\tilde{\Lambda}$. The tidal deformability is similar to the measure of compactness of star [AAA+17], and together with a measure of the mass, is can be used to extract the NS radius [TMR19]. The tidal deformability extracted from GW170817 is $70 < \tilde{\Lambda} < 720$ at 90% confidence level from Ref. [AAA+19], and $70 < \tilde{\Lambda} < 500$ from Ref. [DFL+18] where the electromagnetic counterpart of the signal is additionally considered to constrain their model. Moreover the $\tilde{\Lambda}$ probability distribution function (PDF) exhibit an interesting structure, doubly peaked in Ref. [AAA+19] (with a large and a small peak) and only single peaked in Ref. [DFL+18].

After the detection, the GW170817 signal has been confronted to various nuclear models of EoS, going from the most agnostic ones, such as piecewise polytropes [RÖP17, AGKV18, MWRSB18, FAMF19] and sound speed EoS [TMR19, TMR18], semi-agnostic approaches where matter composition

is known, Taylor-Expanded EoS [TMR18, LH18, TMR19, CSY19, LH19]) or more traditional approaches based on nuclear interactions or Lagrangians, such as Skyrme Functional [MAF+18, KLK+18, ZCZ19, MAD+19, CSY19], and Relativistic Mean Field [HTZ+18, CSY19, MAF+18, LDL+19, NCP19]. In Refs. [HTZ+18, LDL+19], based on Relativistic Mean Field modeling, the authors concluded that the nuclear empirical parameters L_{sym} is independent of the radius at $1.4M_{\odot}$ and that most of the explored EoSs are inside the tidal deformability limit ($\tilde{\Lambda} < 720$). In Refs [KLK+18] and [MAD+19], 5 and 28 Skyrme Functionals were analyzed predicting NS radii to be $11.8 \leq R_{1.4} \leq 12.8$ km from Ref. [KLK+18] ($R_{1.4} = 11.6 \pm 1$ km from Ref. [MAD+19]) and the tidal deformability for canonical NS mass ($1.4M_{\odot}$) $308 < \Lambda_{1.4} < 583$, respectively. Additionally, it is suggested that the nuclear isoscalar giant monopole resonance (ISGMR) could constrain the compactness of NS [MAD+19]. We also used ISGMR to constrain NS EoS as explained in Sec 3.9.3. In Refs. [AGKV18, MWRSB18], polytropes were used to calculate NS EoS leading to $12 \leq R_{1.4} \leq 13.7$ km for the canonical $1.4M_{\odot}$ NS radius. Similar results are found using both Relativistic Mean Field and Skyrme Functionals [MAF+18, LH18, CSY19] , as well as Taylor-Expanded EoS [LH18, CSY19]. Contrary to Ref. [HTZ+18], Taylor-Expanded EoS from Ref [CSY19] showed that the tidal deformability has a specific impact on both the slope of the incompressibility at the saturation density M_0 and $L_{\rm sym}$ (see Eq. 3.4). Recently, GW170817 has been reanalysed based on an agnostic approach and including a constraint on the maximal mass of NS [CTB+19]. This analysis concluded that the NS radius shall be $R \sim 11 \pm 1$ km. The difference of radius on these works can be explained due to the impact of selected EoSs.

In addition to the GW signal, the GW170817 binary NS merger have produced an observed electromagnetic signal (AT2017gfo) and a gamma-ray burst (GRB170817A). These additional signals are influenced by the properties of the in-spiral NS, and could potentially also help the characterization of the tidal deformability. A recent multi-messenger Bayesian analysis has been performed based on the present knowledge and modeling of the EM and GRB signals [CDMM19]. This analysis has considerably reduced the Bayesian probability corresponding to $\tilde{\Lambda} \leq 300$, which reinforce the probability for $\tilde{\Lambda} \geq 300$ [CDMM19]. While one should expect improved modeling of the electromagnetic and gamma-ray burst emission before rising strong

conclusions, this analysis illustrates how a global understanding of the transient event could shed light on the estimation of the tidal deformability.

3.4. Main Principles

Until now we provided observational and theoretical data about NSs, which also describes the starting point and framework of our work. Therefore, it is worth to mention about the principle of this work before explaining theoretical foundations. As we discussed above, the most common description of the NS is a giant nuclear system which contains neutrons and protons, as well as a gas of electrons and muons at the β equilibrium [RPJ+18]. If we assume this description is true, it opens a possibility to define high density region of nuclear EoS from the NS observations. Hence, since we aim at exploring the limits of nucleonic hypothesis for the composition of the core of NS, we currently did not include phase transition at high density. All in all, the NS EoS should satisfy following conditions:

- The EoS should have compatible results at finite nuclear properties and its implications should be feasible to the nuclear physics without model dependence.
- The EoS should satisfy to the NS observations in terms of maximum observed NS mass and tidal deformability.
- The EoS should naturally satisfy causality and stability conditions at all densities [RR74].

3.5. A Semi-Agnostic Approach: The Meta-Model

3.5.1 Meta-Model: Introduction

We consider an semi-agnostic approach which is mainly parameterized in terms of nuclear empirical parameters (describing EoS fundamental properties such as the nuclear incompressibility) and can thus be easily related to

experimental knowledge from nuclear physics. At variance to fully agnostic approaches such as piece-wise polytropes [RÖP17, AGKV18, MWRSB18, FAMF19] or sound speed model [TMR18, TMR19], the present meta-model can predict proton, electron and muons ratios as function of the density. These ratios are controlled by the density dependence of the symmetry energy, and therefore the meta-model establishes correlations between particle ratios and nuclear empirical parameters. It allows to follow the β equilibrium and any path out-of-equilibrium, such as the ones encountered in supernova core collapse [MCG18a]. Hence, it can reproduce the EoSs based on any nuclear interactions such as Skyrme Functional or Relativistic Mean Field by choosing a different empirical parameters for each model. Thanks to the meta-model, the problem reduces to find adequate empirical parameters from the observables of nuclear physics and NSs.

Let us explain how the meta-model can potentially include all EoSs from nuclear physics. To do so, one should perform a link between experimental nuclear observables and theory, which can be done introducing the so-called nuclear empirical parameters. The link between NS matter and nuclear experiments can be performed through the nuclear empirical parameters, directly connected to the properties of the EoS. These parameters are defined as the Taylor coefficients of the binding energy density for symmetric matter (SM) $e_{\rm sat}$ and for the symmetry energy $e_{\rm sym}$,

$$\begin{aligned} e_{sat}(n_0) &= E_{\rm sat} + \frac{1}{2}K_{\rm sat}x^2 + \frac{1}{3!}Q_{\rm sat}x^3 \\ &\quad + \frac{1}{4!}Z_{\rm sat}x^4 + O(x^5), \qquad (3.4) \\ e_{sym}(n_0) &= E_{\rm sym} + L_{\rm sym}x + \frac{1}{2}K_{\rm sym}x^2 + \frac{1}{3!}Q_{\rm sym}x^3 \\ &\quad + \frac{1}{4!}Z_{\rm sym}x^4 + O(x^5). \qquad (3.5) \end{aligned}$$

where the Taylor expansion parameter is $x = (n_0 - n_{\rm sat})/(3n_{\rm sat})$ [PC09a], n_0 being the isoscalar density for protons and neutrons, $n_0 = n_n + n_p$. In the equation above, $E_{\rm sat}$ is the saturation energy, $K_{\rm sat}$ is the incompressibility modulus, $Q_{\rm sat}$ is the skewness parameter, $E_{\rm sym}$ is the symmetry energy, $L_{\rm sym}$ is the slope of the symmetry energy, $K_{\rm sym}$ is the curvature of the symmetry energy sometimes called the symmetry incompressibility and $Q_{\rm sym}$ is the third derivative of the symmetry energy. Besides, the parameter $Z_{\rm sat}$ ($Z_{\rm sym}$)

is the fourth derivative of saturation (symmetry) energy which is completely unknown. Assuming that these two quantities (e_{sat} and e_{sym}) are the leading ones, the binding energy in isospin asymmetric matter (AM) can be expressed as,

$$e(n_0, n_1) = e_{\rm sat}(n_0) + \left(\frac{n_1}{n_0}\right)^2 e_{\rm sym}(n_0), \tag{3.6}$$

where the isovector density is defined as $n_1 = n_n - n_p$. Note that Eq. (3.6) neglects the contribution beyond the quadratic terms in isospin asymmetry.

3.5.2 Enhanced Fermi Gas Calculation

Let us now turn to the meta-model. As it is well known, neutrons and protons can be considered as independent particles in Fermi Gas (FG) approximation. Since the FG can be considered only kinetic contribution of particles, one could make an extension by including interactions. Let us start to explain the FG model, before meta-modeling. The kinetic energy of FG can be expressed as:

$$T_n = \frac{< P^2 >}{2M_n} = \left(\frac{3}{5}\right)\frac{P_F^2}{2M_n}, \tag{3.7}$$

where M_n is the mass of nucleons (n =n for neutrons or p for protons), P and P_F are the momentum and the Fermi momentum respectively. In the case of AM, the total kinetic energy can be written as

$$T(p, n, T_p, T_n) = pT_p + nT_n. \tag{3.8}$$

Here T_p (T_n) is the kinetic energy for proton (neutron) and p (n) is proton (neutron) number. However, one needs to relate p (n) to n_0 and n_1. This can be done by

$$n_p = \frac{p}{\Omega}, \tag{3.9}$$

$$n_n = \frac{n}{\Omega}, \tag{3.10}$$

where Ω is the total volume. Since the volume is unchangeably large in the nuclear matter concept, we do not use energy but rather energy density as a measurable quantity. We then define the kinetic energy density instead

kinetic energy:

$$t^{FG*}(n_p, n_n, T_p, T_n) \equiv \frac{T(p, n, T_p, T_n)}{\Omega} = n_p T_p + n_n T_n. \tag{3.11}$$

On the other hand, the neutron and proton densities, n_n and n_p, can be defined as

$$n_{n/p} = \frac{1}{3\pi^2} k^3_{F_{n/p}}, \tag{3.12}$$

in terms of the Fermi momentum $k_{F_{n/p}}$. Using Eq. (3.12) to Eq. (3.11) in terms of n_0 and n_1, one can obtain to kinetic energy density for isospin asymmetry as

$$t^{FG*}(n_0, n_1) = \frac{t^{FG}_{\rm sat}}{2} \Big(\frac{n_0}{n_{\rm sat}}\Big)^{2/3} f_1(\delta) \tag{3.13}$$

where $t^{FG}_{\rm sat} = 3\hbar^2/(10m)(3\pi^2/2)^{2/3} n^{2/3}_{\rm sat}$ is the kinetic energy per nucleons in SM and at saturation, m is nucleonic mass taken identical for neutrons and protons ($m = (m_n + m_p)/2 = 938.919$ MeV/c^2), giving $t^{FG}_{\rm sat} = 22.1$ MeV. Note that $t^{FG}_{\rm sat}$ selected from the centroid value of $n_{\rm sat}$ which is $n_{\rm sat} = 0.155 \pm 0.005$ fm^{-3} from nuclear models [MCG18a].

The function $f_1(\delta)$ is defined as

$$f_1(\delta) \equiv (1+\delta)^{5/3} + (1-\delta)^{5/3}, \tag{3.14}$$

where, $\delta = (n_1/n_0)$ is called isospin asymmetry parameter. The two boundaries $\delta = 0$ and 1 correspond to SM and to neutron matter (NM), respectively, while any value of δ between -1 and 1 defines AM.

Let us focus on Landau effective mass. The effective mass is a useful concept used to characterize the propagation of quasiparticles inside a strongly interacting medium, such as nuclei or nuclear matter. It reflects the nonlocality in space and time of the quasiparticle self-energy. The nonlocality in space, also called the Landau effective mass, is related to the momentum dependence of the nuclear interaction. The Landau effective mass depends on the isoscalar and isovector densities and can be different for neutrons and protons. The Landau effective mass can also be different for SM and AM: $m^*_n = m^*_p$ for SM whereas in AM, the neutron and proton Landau effective mass can be different. Therefore the isospin splitting of the Landau effective

mass can then be generally expressed as

$$\Delta m^*(n_0, n_1) = m_n^*(n_0, n_1) - m_p^*(n_0, n_1). \tag{3.15}$$

Two quantities ($m_n^*(n_0, n_1)$ and $m_p^*(n_0, n_1)$) can be written as an expansion for SM at saturation $m_{\rm sat}^*$ and the isospin splitting taken for $n_0 = n_1 = n_{\rm sat}$ in NM, $\Delta m_{\rm sat}^*$. The momentum dependence of the nuclear interaction gives rise to the concept of effective mass: An average effect of the in-medium nuclear interaction is to modify the inertial mass of the nucleons. Thereafter the Landau effective mass can be parameterized according to isospin asymmetry in the following way;

$$\frac{m}{m_\tau^*(n_0, n_1)} = 1 + (\kappa_{\rm sat} + \tau_3 \kappa_{\rm sym}\delta)\frac{n_0}{n_{\rm sat}} \tag{3.16}$$

where $\tau_3 = 1$ for neutrons and -1 for protons (τ is proton and neutron), and the parameters $\kappa_{\rm sat}$ and $\kappa_{\rm sym}$ are a function of $m_{\rm sat}^*$ and $\Delta m_{\rm sat}^*$. In the framework of the meta-model, we use $m_{\rm sat}^*$ and $\Delta m_{\rm sat}^*$ as inputs as well as the empirical parameters defined in Eq. (3.4) (the connection to empirical parameters will be shown explicitly in this section). In Eq. 3.16, both $\kappa_{\rm sat}$ and $\kappa_{\rm sym}$ can be rewritten from $m_{\rm sat}^*$ and $\Delta m_{\rm sat}^*$ at $n = n_{\rm sat}$:

$$\begin{aligned} \kappa_{\rm sat} = \frac{m}{m_{\rm sat}^*} - 1 &= \kappa_s, \text{ in SM } (\delta = 0), \\ \kappa_{\rm sym} = \frac{1}{2}\left[\frac{m}{m_n^*} - \frac{m}{m_p^*}\right] &= \kappa_s - \kappa_v, \text{ in NM } (\delta = 1). \end{aligned} \tag{3.17}$$

Thereafter, one can write m from $m_p^*(n_0, n_1)$ and $m_n^*(n_0, n_1)$ at $n_0 = n_1 = n_{\rm sat}$ with the help of Eq. (3.16) to the Eq. (3.13), the new expression for the kinetic energy in nuclear matter appears which includes effective mass parameters:

$$\begin{aligned} t^{FG*}(n_0, n_1) = \frac{t_{\rm sat}^{FG}}{2}\left(\frac{n_0}{n_{\rm sat}}\right)^{2/3}\Bigg[\left(1 + \kappa_{\rm sat}\frac{n_0}{n_{\rm sat}}\right) f_1(\delta) \\ + \kappa_{\rm sym}\frac{n_0}{n_{\rm sat}} f_2(\delta)\Bigg], \end{aligned} \tag{3.18}$$

where the new function f_2 is defined as

$$f_2(\delta) \equiv \delta(1+\delta)^{5/3} - \delta(1-\delta)^{5/3}. \tag{3.19}$$

3.5.3 *Meta-Eos: Linking Nuclear EoS Parameters to the Model*

In this work, we consider the metamodeling ELFc introduced in Ref. [MCG18a]. In this metamodeling, the energy per particle is defined as

$$e(n_0, n_1) = t^{FG*}(n_0, n_1) + v(n_0, n_1). \tag{3.20}$$

The first term is the kinetic energy density as presented in Eq. (3.18) and the second term is the interaction potential which can be expressed as

$$v(n_0, n_1) = \sum_{a\geq 0}^{N} \frac{1}{a!}(c_a^{sat} + c_a^{sym}\delta^2)x^a u_a(x), \tag{3.21}$$

where $u_a(x) = 1-(-3x)^{N+1-a}\exp(-bn_0/n_{\rm sat})$ and b is fixed to be $b = 10\ln 2 \approx 6.93$. The function $u_a(x)$ and the parameter b are fitted according to the high density behavior of nuclear EoSs which is generated from various models [MCG18a].

Fixing parameters $\kappa_{\rm sat}$ and $\kappa_{\rm sym}$, the coefficients c_a^{sat} and c_a^{sym} are directly related to the empirical parameters through the following one-to-one correspondences by comparing Eq. (3.20) and Eq. (3.4),

$$\begin{aligned}
c_{a=0}^{sat} &= E_{\rm sat} - t_{\rm sat}^{FG}(1+\kappa_{\rm sat}),\\
c_{a=1}^{sat} &= -t_{\rm sat}^{FG}(2+5\kappa_{\rm sat}),\\
c_{a=2}^{sat} &= K_{\rm sat} - 2t_{\rm sat}^{FG}(-1+5\kappa_{\rm sat}),\\
c_{a=3}^{sat} &= Q_{\rm sat} - 2t_{\rm sat}^{FG}(4-5\kappa_{\rm sat}),\\
c_{a=4}^{sat} &= Z_{\rm sat} - 8t_{\rm sat}^{FG}(-7+5\kappa_{\rm sat}),
\end{aligned} \tag{3.22}$$

and

$$\begin{aligned}
c_{a=0}^{sym} &= E_{\rm sym} - \frac{5}{9}t_{\rm sat}^{FG}[1+(\kappa_{\rm sat}+3\kappa_{\rm sym})],\\
c_{a=1}^{sym} &= L_{\rm sym} - \frac{5}{9}t_{\rm sat}^{FG}[2+5(\kappa_{\rm sat}+3\kappa_{\rm sym})],
\end{aligned}$$

$$
\begin{aligned}
c_{a=2}^{sym} &= K_{\rm sym} - \frac{10}{9} t_{\rm sat}^{FG}[-1 + 5(\kappa_{\rm sat} + 3\kappa_{\rm sym})], \\
c_{a=3}^{sym} &= Q_{\rm sym} - \frac{10}{9} t_{\rm sat}^{FG}[4 - 5(\kappa_{\rm sat} + 3\kappa_{\rm sym})], \\
c_{a=4}^{sym} &= Z_{\rm sym} - \frac{40}{9} t_{\rm sat}^{FG}[-7 + 5(\kappa_{\rm sat} + 3\kappa_{\rm sym})].
\end{aligned} \tag{3.23}
$$

The one-to-one correspondence between the meta-model coefficients c_a^{sat}, c_a^{sym} and the empirical parameters directly bridges the analysis of the impact of the empirical parameters on the properties of the equation of state to the predictions of NS properties. To summarise, we got 10 empirical parameters from the Taylor expansion ($E_{\rm sat}$, $n_{\rm sat}$, $K_{\rm sat}$, $Q_{\rm sat}$, $Z_{\rm sat}$, $E_{\rm sym}$, $L_{\rm sym}$, $K_{\rm sym}$, $Q_{\rm sym}$, and $Z_{\rm sym}$) and 2 parameters from Landau effective mass ($m^*_{\rm sat}$ and $\Delta m^*_{\rm sat}$) which are inputs of the metamodel.

3.5.4 The Condition of β Equilibrium

Let us now discuss about the β equilibrium. Until here, we discussed how to calculate EoS if isovector (n_0) and isoscalar (n_1) densities are known. In case of NSs, these densities are determined from the β equilibrium condition. As discussed in Sec. 3.1, dying star core becomes neutron rich nuclear matter with electron capture processes. However, it takes up to 100 years to reach thermal equilibrium between crust and core. After that NSs continue to cool down by neutrino processes where particle compositions are defined by β equilibrium for temperature of NSs [LP07]. When the temperature of NSs is around the nuclear scale (1 MeV or 10^{10} K), the system could be considered to be frozen where particle composition is stable from the point of view of hadronic or leptonic picture [Gle12]. In this case, NS EoS can be investigated as β equilibrium nuclear matter. We shall also remind that the phase transition to hyperonic matter is excluded in present work since it could have a noticeable impact on equilibrium conditions. Given a proton fraction $x_p = n_p/n_0$, charge neutrality condition immediately imposes $x_p = x_e$ where x_e is the electron fraction and we also have $p_{F_e} = p_{F_p}$ for Fermi momentums. The impact of the β equilibrium condition can easily be calculated by minimizing the total energy of the system:

$$
\varepsilon(n_p, n_n) = e(n_p, n_n) + E_{\rm elec} + \frac{n_p}{n_0} m_p c^2 + \frac{n_n}{n_0} m_n c^2, \tag{3.24}
$$

where m_p (m_n) are the rest mass of proton (neutron), $e(n_p, n_n)$ the energy density from the meta-model and $E_{\rm elec}$ the electron energy density which can be written from the ultra-relativistic limit:

$$E_{\rm elec} = c(p_{F_e}^2 + m_e^2 c^2)^{1/2}, \tag{3.25}$$

where p_{F_e} is the Fermi momentum of electron, c speed of light and m_e the rest mass of electron. One then can calculate each particle fraction by minimizing the total energy (see Ref. [BL91] for details):

$$\frac{d\varepsilon(n_p, n_n)}{dx_p} = 0. \tag{3.26}$$

When the electron Fermi energy is large enough (around the threshold energy for muons ($m_\mu c^2 \approx 105$ MeV)), electron to muon conversion is energetically favorable with the decay channel [PLPS04, BACK16]:

$$e^- \longrightarrow \mu^- + \nu_e + \bar{\nu_\mu}. \tag{3.27}$$

Therefore the total energy of the system becomes,

$$\varepsilon(n_p, n_n) = e(n_p, n_n) + E_{\rm elec} + \frac{n_p}{n_0} m_p c^2 + \frac{n_n}{n_0} m_n c^2 + E_\mu, \tag{3.28}$$

where E_μ the muon energy density can be show in ultra-relativistic limit:

$$E_\mu = c(p_{F_\mu}^2 + m_\mu^2 c^2)^{1/2}, \tag{3.29}$$

where p_{F_μ} is the Fermi momentum and m_μ is the rest mass of muon. Imposing the charge neutrality condition $x_e = x_p - x_\mu$, the total energy density defined in Eq. (3.28) becomes a function of proton and electron fraction, where one can find each particle fraction by minimizing the total energy [PLPS04, BACK16]:

$$\left.\frac{\partial\varepsilon(n_p, n_n)}{\partial x_p}\right|_{x_\mu} = 0 \tag{3.30}$$

$$\left.\frac{\partial\varepsilon(n_p, n_n)}{\partial x_\mu}\right|_{x_p} = 0 \tag{3.31}$$

The advantage of the meta-model is that it is analytical, fast computed, very flexible and can reproduce most of existing nucleonic EoS. Moreover, it keeps information concerning matter composition, such as the neutron/proton ratio, the fraction of electrons and muons. It is therefore optimal for extensive statistical analyses which require the set-up of a large number of EoS samples. In the next sections, we briefly detail how the NS properties such as masses, radii and tidal deformabilities can be related to the nuclear equation of state assuming general relativity (TOV and Pulsation equations) [HPY07, Tol39, OV39, Hin08, FH08, DN09].

3.6. Building a Neutron Star: Tolman-Oppenheimer-Volkoff Equations

According to Birkhoff's theorem the Schwarzschild solution is the most general description outside a nonrotating, spherically symmetric star [MTW73]. Although, the Schwarzschild solution works well outside spherical objects, one need to define a more general metric to describe energy and pressure profiles inside the NS. Starting time-independent form of the Schwarzschild solution, $ds^2 = g_{\mu\nu}dx^\mu dx^\nu = -e^{2\Phi(r)}c^2dt^2 + e^{2\lambda(r)}dr^2 + r^2(d\theta^2 + sin^2\theta d\phi^2)$, where the potential $\Phi(r)$ and the function $\lambda(r)$ only depend on r (the function λ being fixed to $e^{-2\lambda} = 1 - 2Gm/(c^2r)$), the Einstein equation produce the necessary relations at the hydrostatic equilibrium in the NS where it is calculated from the vanishing divergence of the energy-momentum tensor. Let us first write the Einstein equation as:

$$G^{\mu\nu} \equiv R^{\mu\nu} - \frac{1}{2}Rg^{\mu\nu} = \frac{8\pi G}{c^4}T^{\mu\nu}, \tag{3.32}$$

where G is the gravitational constant and c the speed of light in the vacuum. The general approach for solving Einstein equation is equalling the left hand side (Einstein Tensor) and the right hand side (energy-momentum tensor). The energy-momentum tensor can be written as

$$T^{\mu\nu} = (\varepsilon + P)\frac{u^\mu u^\nu}{c^2} + Pg^{\mu\nu}, \tag{3.33}$$

where P the pressure and ε the energy density containing contributions from the nucleon rest mass (m_N) and from the total energy per particles (e): $\varepsilon = (m_N c^2 + e)n_0$. Besides one can obtain diagonal components of 4-velocity by using $-c^2 = g_{\mu\nu}u^\mu u^\nu$. Equalling the left hand side and the right hand side the $G^{tt} = \frac{8\pi G}{c^4}T^{tt}$ component of Eq. (3.32):

$$\frac{dm(r)}{dr} = \frac{4\pi r^2}{c^2}\varepsilon(r), \tag{3.34}$$

where $m(r)$ the enclosed mass at radius r.

From the $G^{rr} = \frac{8\pi G}{c^4}T^{rr}$ component, one gets

$$\frac{d\Phi(r)}{dr} = \frac{Gm}{c^2 r^2}\left(1 + \frac{4\pi P(r) r^3}{mc^2}\right)\left(1 - \frac{2Gm}{rc^2}\right)^{-1}. \tag{3.35}$$

However, a differential equation for the pressure is also required This is done by using conservation of energy, implying that the divergence of the stress-energy tensor vanishes. Since the system is spherical symmetric, this can be done by using radial component ($\mu = r$):

$$0 = \nabla_\nu T^{r\nu} = \frac{\partial T^{r\nu}}{\partial x^\nu} + T^{\sigma\nu}\Gamma^r_{\sigma\nu} + T^{r\sigma}\Gamma^\nu_{\sigma\nu}, \tag{3.36}$$

eventually leading to

$$\frac{dP(r)}{dr} = -\big(P(r) + \varepsilon(r)\big)\frac{d\Phi(r)}{dr}. \tag{3.37}$$

Eqs.(3.34, 3.35 and 3.37) are named as the Tolman-Oppenheimer-Volkoff (TOV) equations [MTW73, Tol39, OV39]. For convenience we show these equations all together:

$$\begin{aligned}
\frac{dm(r)}{dr} &= \frac{4\pi r^2}{c^2}\varepsilon(r), \\
\frac{dP(r)}{dr} &= -\big(P(r) + \varepsilon(r)\big)\frac{d\Phi(r)}{dr}, \\
\frac{d\Phi(r)}{dr} &= \frac{Gm}{c^2 r^2}\left(1 + \frac{4\pi P(r) r^3}{mc^2}\right)\left(1 - \frac{2Gm}{rc^2}\right)^{-1}.
\end{aligned} \tag{3.38}$$

Eqs. (3.38) are integrated in coordinate space starting from 0 to the radius R, fixing the boundary conditions $m(0) = 0$ and $P(0) = P_c$ where $P_c(\varepsilon = \varepsilon_c)$ is arbitrarily varied. The pressure P decreases from the center to the surface and the NS radius is defined as the coordinate for which the condition $P(r = R) = 0$ is reached. The family of solutions with unique mass $m(R) = M$ and radii R are generated by varying the central energy density ε_c.

Since there are three equations for four variables (m, P, ε and Φ) in Eqs. (3.38), one need another equation to close the system. This additional equation is provided by the equation of state of dense matter, $P(\varepsilon)$, which is evaluated at β-equilibrium for the NS conditions. NSs are formed by a crust and a core whereas in the meta-model we considered only applies to uniform matter inside the core. We refer Ref. [ACCG19] to the reader in order to see application of meta-model on the crust EoS. Since the crust includes multiple phases, we did not make an analysis for a crust EoS as well as transition density n_{tr}. Besides, we expect that the impact of the connection between the crust and the core is small for our analysis (for more details see Ref. [MCG18b]). The core EoS is matched to the crust EoS with a cubic spline starting from an arbitrary transition density $n_{tr} = 0.1 n_{sat}$ to $n_{\rm sat}$. Below n_{tr}, we set crust EoS to be SLY for all core EoSs [DH01]. SLY (also known as Douchin-Haensel EoS) is based on the Skyrme nuclear interaction SLy4 [CBH$^+$98], which has been applied for the crust EOS considering a compressible liquid-drop model [DH01]. Apart from the nuclear interaction, the model of crust includes considerable modeling behind such as $T = 0$ approximation or the assumption of the ground state composition. Since details are far beyond from the scope of this work, we refer Ref. [DH01] for a discussion about the SLY EoS. In next section we will discuss how we use GW to our advantage to describe NS EoS.

3.7. Pulsation Equations and Gravitational Wave

3.7.1 Tidal Love Number

As discussed in Sec. 3.1, the observational constraints on the internal structure of NSs are weak and there is no direct method to measure radii of NS. X-ray observations requires to have a model for the emission itself, which

can be thermal (improved black-body) or a burst, or generated by a hot spot (or several) located at the surface of the neutron star. In all these cases, in addition to general relativity, a model for the emission process is required. The art of the observation is to isolate some neutron stars for which there is almost no ambiguity in the interpretation of the data, for instance see Ref. [dGM+19] for details. In the latter case, one could still argue that there is a $1 - 1.5$ km uncertainty coming from systematical uncertainties (model dependence related to atmospheric conditions or selected EoSs). While it is not entirely satisfactory, it is comparable with the uncertainty from binary neutron star mergers. Thus, X-ray observations are not presently very constraining for the EoS determination, but they provide promising new observables which could bring more accuracy by accumulating more events and could be contrasted with other methods to provide a consistent picture. However, measuring GW from NS in-spiral can provide additional constraint on the NS EoS. Coalescing binary NSs are one of the most important sources for ground-based gravitational wave detectors [CT02].

One way to utilise GW to describe EoS is to make hydrodynamics simulation of NS-NS mergers on post-merger phases [Bau03]. However, trying to extract EoS information in this way rises several difficulties which complex behavior requires solving the nonlinear equations of general relativity together with relativistic hydrodynamics. Moreover, the signal includes unknown quantities such as spins and angular momentum distribution inside the NS (see Ref. [Hin08] for details). There is however an easier method to use GW to constrain the EoS. During the early time of in-spiral, the GW signal is very clean and the influence of tidal effects correspond the only small correction to waveform's phase. However, at the late times of merger, it could alter the GW signal, or alternatively could give information about the NS structure. This has been studied by several authors (see Ref. [BPM+02] and therein). The influence of the internal structure of the NS on the gravitational wave phase in this early regime of the in-spiral is characterized by a single parameter, namely, the ratio λ of the induced quadrupole to the perturbing tidal field. This ratio λ (or Λ see Eq. (3.54)) also called tidal deformability, is related to the star's tidal Love number k_2 by

$$\lambda = \frac{2k_2}{3R^5} \tag{3.39}$$

where R the radius of NS [Hin08, FH08].

3.7.2 Pulsation Equations

The tidal Love number k_2 is an outside solution of linearized perturbation equations due to an external quadrupolar tidal field. To derive the expression of k_2, we first express the Einstein equation in the effect of a quadrupolar tidal field. We use derivation from Ref. [TC67] which uses spherical harmonics in Regge-Wheeler gauge for the electrical part of the even-parity static pulsation. In the presence of a quadrupole field, the metric can be described by making first order perturbation to the Schwarzschild metric:

$$g_{\mu\nu}^{(ac)} = g_{\mu\nu} + h_{\mu\nu}, \tag{3.40}$$

where $h_{\mu\nu}$ is a linearized metric perturbation and $g_{\mu\nu}$ is the Schwarzschild metric, which is $ds^2 = g_{\mu\nu}dx^\mu dx^\nu = -e^{2\Phi(r)}c^2dt^2 + e^{2\lambda(r)}dr^2 + r^2(d\theta^2 + sin^2\theta d\phi^2)$. Using the Regge-Wheeler gauge condition, $h_{\mu\nu}$ becomes

$$h_{\mu\nu} = [-e^{2\Phi(r)}H_0(r)c^2dt^2 + e^{2\lambda(r)}H_2(r)dr^2 + r^2K(r)(d\theta^2 + sin^2\theta d\phi^2)]Y_{20}, \tag{3.41}$$

where Y_{20} is spherical harmonic. It should be noted that non-diagonal elements of both $g_{\mu\nu}$ and $h_{\mu\nu}$ are zero. In order to derive $H_0(r)$, $H_2(r)$ and $K(r)$ functions, one needs to use the linearized version of Einstein equation. Therefore, before finding metric elements, we first discuss how to derive linearized Einstein equation. Thus is obtained by taking variations of both side of Einstein equation:

$$\delta G_\nu^\mu = \frac{8\pi G}{c^4}\delta T_\nu^\mu. \tag{3.42}$$

The left hand side is:

$$\delta G_{\mu\nu} = \delta[R_{\mu\nu} - \frac{1}{2}Rg_{\mu\nu}] = \delta R_{\mu\nu} - \frac{1}{2}[h_{\mu\nu}R + g_{\mu\nu}\delta R], \tag{3.43}$$

where $\delta R = g^{\mu\nu}\delta R_{\mu\nu} + h^{\mu\nu}R_{\mu\nu}$. It is convenient to use δG_ν^μ instead of $\delta G_{\mu\nu}$ since the equations are much simpler in this way. The corresponding form of Einstein tensor is

$$\delta G_\nu^\mu = \delta(g^{\mu\beta}G_{\beta\nu}) = h^{\mu\beta}G_{\beta\nu} + g^{\mu\beta}\delta G_{\beta\nu}, \tag{3.44}$$

where $G_{\beta\nu} = R_{\beta\nu} - \frac{1}{2}Rg_{\beta\nu}$ is the unperturbed Einstein tensor based on the Schwarzschild metric. The right hand side of linearized Einstein equation is based on the perturbated energy momentum tensor which can be written as [TC67],

$$\delta T^{\mu}_{\nu} = \begin{cases} \delta T^{\mu}_{\nu} = \delta\varepsilon/c^2, & \mu = \nu = t; \\ \delta T^{\mu}_{\nu} = -\delta P, & \mu = \nu \text{ and } \mu = r, \theta, \phi; \\ \delta T^{\mu}_{\nu} = 0, & \mu \neq \nu. \end{cases} \tag{3.45}$$

Equating left hand side and right hand side of Eq. (3.42), one can express the variables $H_0(r)$, $H_2(r)$ and $K(r)$ in terms of $H_0(r) = H(r)$ as

$$\delta G^{\theta}_{\theta} - \delta G^{\phi}_{\phi} = -\delta P + \delta P = 0 \implies -H_2(r) = H_0(r) = H(r), \tag{3.46}$$

$$\delta G^{r}_{\theta} = 0 \Longrightarrow \frac{dK(r)}{dr} = 2H(r)\frac{d\Phi(r)}{dr} + \frac{dH(r)}{dr}, \tag{3.47}$$

where $d\Phi(r)/dr$ is already defined in Eq. (3.38). Besides, there are still variables coming from the perturbated energy momentum tensor (δP and $\delta\varepsilon$). However, it can be elegantly process by using $\delta\varepsilon = c_s\delta P$ where $c_s \equiv (c^2)(dP/d\varepsilon)^{-1}$ is the speed of sound. Keeping this mind, one can replace δP as

$$\delta P = -c^4\frac{\delta G^{\theta}_{\theta} + \delta G^{\phi}_{\phi}}{16\pi G}, \tag{3.48}$$

using in to

$$\delta G^{t}_{t} - \delta G^{r}_{r} = \frac{8\pi G}{c^4}\delta P\big(c_s + 1\big), \tag{3.49}$$

leads to the pulsation equation for NS interior;

$$r\frac{dy(r)}{dr} + y(r)^2 + y(r)F(r) + Q(r) = 0, \tag{3.50}$$

with

$$F(r) = \frac{1}{r - 2Gm/c^2}\left(\frac{r + 4\pi Gr^3}{P - \varepsilon}\right), \tag{3.51}$$

$$Q(r) = \frac{4\pi Gr^3/c^2}{r - 2Gm/c^2}\left(\frac{5\varepsilon}{c^2} + \frac{9P}{c^2} + \frac{P + \varepsilon}{c_s}\right)$$

$$-\frac{4\pi G r^3/c^2}{r-2Gm/c^2}\left(\frac{6}{4\pi G r^2/c^2}\right)-\left(\frac{2G^2 r}{c^4}\right)\times\left(\frac{m+4\pi r^3 P/c^2}{r-2Gm/c^2}\right)^2,$$

where $y(r)\equiv RH'(r)/H(r)$ and $H'=dH/dr$. However, Eq. (3.50) is only valid inside of the NS. Outside of the NS, Eq. (3.50) becomes associated Legendre equation with $l=m=2$ for which $H(r)$ is analytically solvable.

3.7.3 An Observable: Tidal Deformability

In order to build a bridge between the pulsation equations and tidal Love number k_2, one can make a multipolar expansion (in the framework of general relativity) for mass, by only taking leading terms [Tho98]:

$$-\frac{g_{tt}+1}{2}=-\frac{m}{r}-\frac{3Q_{ij}}{2r^3}n^i n^j+...+\frac{R_{0i0j}}{2}r^2 n^i n^j+...\ , \tag{3.52}$$

where $Q_{ij}=-\lambda R_{0i0j}$ and $\vec{n}=(\sin(\theta)\cos(\phi),\sin(\theta)\sin(\phi),\cos(\theta))$. Using the outside solution of $H(r)$ (outside version of Eq. (3.50)) and Eq. (3.39), tidal Love number (k_2) can be extracted as:

$$\begin{aligned}k_2 \ = \ & \frac{8C^5}{5}(1-2C)^2[2+2C(Y-1)-Y]\\ &\times\big\{2C[6-3Y+3C(5Y-8)]\\ &+4C^3[13-11Y+C(3Y-2)+2C^2(1+Y)]\\ &+3(1-2C)^2[2-Y+2C(Y-1)]\\ &\times\ln(1-2C)\big\}^{-1},\end{aligned} \tag{3.53}$$

where $Y=y(R)$ is the solution of the pulsation equation at the surface of the NS. Note that $Y=y(R)$ is a continuous quantity which is valid for both inside and outside of the NS. The pulsation equation is solved once the density and pressure radial profiles are defined from the solution of the TOV equations. Despite that the tidal Love number is proposed as a measurable quantity from GW (see Refs. [Hin08, FH08]), nowadays the mostly used related quantity is dimensionless tidal deformability (which it is still called

tidal deformability) Λ [AAA+17, DFL+18, CDMM19]. Similarly to λ, it is defined from the tidal Love number as

$$\Lambda = \frac{2k_2}{3C^5}, \tag{3.54}$$

where $C = (GM)/(c^2R)$ is compactness for the NS of mass M and radius R.

Due to the current sensitivity of the detectors, actually observed quantity is the effective tidal deformability $\tilde{\Lambda}$, defined from each individual deformabilities of the NS, Λ_1 and Λ_2 (see Ref. [Fav14] for details), as

$$\tilde{\Lambda} = \frac{16}{13}\frac{(M_1 + 12M_2)M_1^4\Lambda_1 + (M_2 + 12M_1)M_2^4\Lambda_2}{(M_1 + M_2)^5}, \tag{3.55}$$

where $(M_1,\ \Lambda_1)$ and $(M_2,\ \Lambda_2)$ are the masses and tidal deformabilities of the individual NSs (by convention $M_1 \geq M_2$) [AAA+17]. If $M_1 = M_2$, this expression becomes $\tilde{\Lambda} = \Lambda_1 = \Lambda_2$. However, as discussed below, we shall explore the general case of asymmetric masses in our study.

3.8. Putting All Together: Bayesian Statistics

The relation between nuclear EoS empirical parameters and the NS properties is performed within the Bayesian statistical analysis. The core of the Bayesian analysis lies on Bayes theorem expressing the probability associated to a given model, represented here by its parameters $\{a_i\}$, to reproduce a set of data, $P(\{a_i\} \mid \text{data})$ also called the posterior PDF [SS06]:

$$P(\{a_i\} \mid \text{data}) \simeq P(\text{data} \mid \{a_i\}) \times P(\{a_i\}), \tag{3.56}$$

where $P(\text{data} \mid \{a_i\})$ is the likelihood function determined from the data comparison between the model and the measurement, and $P(\{a_i\})$ is the prior PDF which represents our knowledge or bias on the model parameters. Detailed discussions for the prior $P(\{a_i\})$ and for the likelihood probability $P(\text{data} \mid \{a_i\})$ are given in Sec. 3.9.1.

The one- and two-parameter probabilities are defined as [SS06]

$$P(a_j \mid \text{data}) = \left\{ \prod_{\substack{i=1 \\ i\neq j}}^{12} \int da_i \right\} P(\{a_i\} \mid \text{data}) \,, \tag{3.57}$$

$$P(a_j, a_k \mid \text{data}) = \left\{ \prod_{\substack{i=1 \\ i\neq j,k}}^{12} \int da_i \right\} P(\{a_i\} \mid \text{data}) \,. \tag{3.58}$$

These marginal probabilities represent the one parameter PDF and the two-parameter correlation matrix, repectively.

3.9. Constraining a Neutron Star

3.9.1 General Framework

In our analysis, we evaluate the NS EOSs for each set of empirical parameters, which are 12 free parameters in total (10 nuclear empirical parameters and two parameters associated to the Landau effective mass, see Sec.3.5.3 for details). Some of these parameters are however already well-known from the nuclear physics experiments and their small uncertainties do not impact the dense matter EoS to a large extend (see Ref. [MCG18b] for details). The 12 free parameters are therefore separated into three different groups:

(P1) The parameters which are not varied: E_{sat}, E_{sym}, n_{sat}, m^*_{sat}/m and $\Delta m^*_{\text{sat}}/m$ (see Ref. [MCG18b] for details).

(P2) The less-known parameters, which are varied on a uniform grid: K_{sat}, L_{sym}, K_{sym}, Q_{sat} and Q_{sym}.

(P3) The totally unknown parameters, which however do not impact our analysis enough to be explored: Z_{sat} and Z_{sym}, since they do not play a major role for the dense matter equation of state associated to NS in the mass range between $1M_\odot$ and $2M_\odot$ which corresponds to possible masses of the binary NSs from GW170817 (see Ref. [MCG18b] for more details).

$E_{\rm sat}$ (MeV)	$E_{\rm sym}$ (MeV)	$n_{\rm sat}$ (fm^{-3})	$m^*_{\rm sat}/m$	$\Delta m^*_{\rm sat}/m$	$Z_{\rm sat}$ (MeV)	$Z_{\rm sym}$ (MeV)
-15.8	32.0	0.155	0.75	0.1	0	0

Tab. 3.1: The prior parameters: the fixed empirical parameters from group P1 and P3.

Empirical Parameters	$L_{\rm sym}$ (MeV)	$K_{\rm sat}$ (MeV)	$K_{\rm sym}$ (MeV)	$Q_{\rm sat}$ (MeV)	$Q_{\rm sym}$ (MeV)
			Prior set #1		
Min	-10	**150**	-500	-1000	-2000
Max	70	280	**1500**	3000	2000
Step	5	10	200	400	400
N	17	**14**	**11**	11	11
			Prior set #2		
Min	-10	**180**	-500	-1000	-2000
Max	70	280	**300**	3000	2000
Step	5	10	100	400	400
N	17	**11**	**9**	11	11

Tab. 3.2: The prior parameters: the empirical parameters from group (P2), which are varied on a uniform grid for two different scenarios. Changes between the two sets are indicated in bold characters. Here Min, Max are first and last values of the each parameter, Step is an increment for each iteration and N is the number of total fragment. For prior set #1 and #2, please see the text for details.

In Table. 3.1, we show the parameters which are not varied (from group P1), see Ref. [MCG18b] and references therein. The parameters like $E_{\rm sat}$, $E_{\rm sym}$ and $n_{\rm sat}$ are well-known from finite-nuclei experiments and their uncertainty does not impact our analysis. The other parameters such as $m^*_{\rm sat}/m$ and $\Delta m^*_{\rm sat}/m$ are also constrained from nuclear physics experiments, to a lower extend, but their uncertainties only weakly impact dense matter EoS [MCG18a].

In the present analysis the model parameters $\{a_i\}$ which are varied (group P2) are: $L_{\rm sym}$, $K_{\rm sat}$, $K_{\rm sym}$, $Q_{\rm sat}$ and $Q_{\rm sym}$. These empirical parameters are sampled on a uniform grid defined in Table 3.2. These parameters are varied

between a lower (Min) and an upper (Max) value, with N steps defining a constant step. We have considered two different choices for the prior. In the prior set #1, the boundaries of the parameters are determined such that the likelihood probability reaches zero, or a very small value compared to the one inside the range. In the prior set #2, we fix the boundaries to be the ones determined from nuclear physics experiments and reported in Ref. [MCG18a], except for $L_{\rm sym}$ for which we allow the exploration of small values. Anticipating our results, we will show that low values for $L_{\rm sym}$ are favoured by the tidal deformability from GW170817. A detailed discussion about $L_{\rm sym}$ is made in next chapter.

The likelihood probability defines the ability of the model to reproduce the data. In the present analysis, it is defined as [SS06],

$$P(\text{data} \mid \{a_i\}) = w_{\rm filter} \times p_{\tilde{\Lambda}} \times p_{\chi\rm EFT} \times p_{\rm ISGMR}\,, \tag{3.59}$$

where $w_{\rm filter}(\{a_i\})$ is a pass-band type filter which select only the models satisfying the necessary condition (C1) expressed hereafter, and the probabilities $p_{\tilde{\Lambda}}$, $p_{\chi\rm EFT}$ and $p_{\rm ISGMR}$ are associated to constraints (C2)-(C4) expressed hereafter. The constraints entering into the Bayesian probability (Eq. (3.59)) are:

(C1) The necessary conditions that each viable EoS shall satisfy: causality, stability, positiveness of the symmetry energy and maximum observed mass $M^{obs}_{max} = 2.01(4)M_\odot$ [AFW+13].

(C2) $p_{\tilde{\Lambda}}$: the probability associated to the ability of the EoS to reproduce the tidal deformability extracted from the GW170817 event [AAA+19, DFL+18].

(C3) $p_{\chi\rm EFT}$: the probability measuring the compatibility between the meta-model and the energy and pressure bands function of the density predicted from χ-EFT approach below saturation density [DHS16].

(C4) $p_{\rm ISGMR}$: the probability of a given meta-model to be compatible with recent analysis of the ISGMR collective mode [KMV12, KM13].

The constraints (C1) are necessary constraints for all EoS, (C2) are constraints from astrophysics impacting high densities, while (C3) and (C4) are

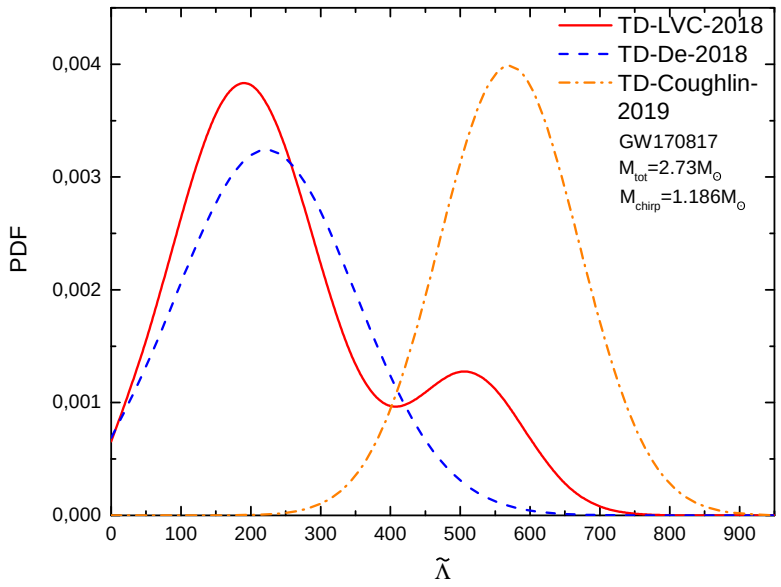

Fig. 3.2: The generated likelihood functions for tidal deformability from Refs. [AAA+19, DFL+18].

constraints from low-density nuclear physics. In the following, we detail how the probabilities associated to these constraints are estimated in practice.

Let us detail the constraints from the group (C1). Causality, stability and positiveness of the symmetry energy are imposed as in Ref. [MCG18b]. The constraints are imposed up to the density corresponding to the maximum density of the stable branch. We also impose that all viable EoS shall have a maximum mass $M_{max} \geq M_{max}^{obs} = 2M_{\odot}$ [AFW+13].

3.9.2 Constraints of the Gravitational Wave

We now come to the constraint (C2) associated to the tidal deformability from GW170817. We consider two independent GW analyses which provide two slightly different $\tilde{\Lambda}$ PDF. These PDFs are displayed in Fig. 3.2 under the legend "TD-LVC-2018" and "TD-De-2018". TD-LVC-2018 is the result of the latest analysis from the LIGO-Virgo collaboration [AAA+19] while TD-De-2018 is an independent analysis proposed in Ref. [DFL+18]. Contrary to TD-De-2018, TD-LVC-2018 has a double peak; the highest one is peaked

around $\tilde{\Lambda}^1_{\rm max} \approx 180$ and the smaller one is around $\tilde{\Lambda}^2_{\rm max} \approx 550$. However, in TD-De-2018, the only peak is $\tilde{\Lambda}_{\rm max} \approx 200$. The presence of a double peak has an impact on the higher value for the 90% confidence-level: It is 720 in the case of TD-LVC-2018 while it is about 500 for TD-De-2018. Anticipating our results, the PDF from TD-De-2018 shall select more compact objects than the one assuming TD-LVC-2018.

Note that recently, a combined analysis including the electro-magnetic and GRB counterpart observations including the remnant mass of NS has shifted up the lower limit for $\tilde{\Lambda}$ and the centroid: $300 < \tilde{\Lambda} < 800$ also displayed under the legend "TD-Coughlin-2019" on Fig. 3.2 [CDMM19].

The probability $p_{\tilde{\Lambda}}$ is calculated in the following way. For a given parameter set $\{a_i\}$, the TOV and the pulsation equations are first solved, which provides a family $\{M_i, \Lambda_i\}$, where i is an index running over the central density. We then sample the mass distribution for the two NS (M_1, M_2) by taking a set of six masses, where M_2 is distributed from $1.1M_\odot$ to $1.35M_\odot$, and M_1 is calculated such that $M_1 + M_2 = 2.73M_\odot$ (observed total mass of the binary $2.73^{+0.04}_{-0.01}M_\odot$ [AAA+19]), accurately determined from GW170817. For each sample elements the combined tidal deformability $\tilde{\Lambda}$ is calculated from Eq. (3.55) and a probability, $p^k_{\tilde{\Lambda}}$, is assigned from the PDF shown in Fig. 3.2 for the two scenarios. The final probability $p_{\tilde{\Lambda}}$ is then obtained from the averaging over sample elements,

$$p_{\tilde{\Lambda}} = \frac{1}{N}\sum_{i=k}^{N} p^k_{\tilde{\Lambda}}\,. \tag{3.60}$$

Note that there are several ways to calculate $p_{\tilde{\Lambda}}$. Another choice could have been, for instance, to assign to the parameter set the maximum probability obtained for $\tilde{\Lambda}$, $p_{\tilde{\Lambda}} = \max_k p^k_{\tilde{\Lambda}}$. However, since the $\tilde{\Lambda}$ PDF only weakly depends on the mass asymmetry [DFL+18], we do not expect a large effect between these two possible prescriptions. It should also be noted that this is true since we do not consider first-order phase transitions: the mass asymmetry between the two NSs could have a strong impact on $\tilde{\Lambda}$ if the phase transition occurs at a mass in-between the ones of the two NS [PYAC+18, TMR19].

In the present analysis, we assume that each neutron star of the binary system has the same EoS, the same particle composition and that their particle

fractions is derived from the β equilibrium condition. Other exotic compositions such as Delta resonances, hyperons giving rise to Hybrid-Star/NS binaries could be considered, are beyond the scope of this work.

3.9.3 Constraints of Nuclear Physics Observables

The constraint (C3) is a nuclear physics constraint which measures the proximity of the meta-model to the prediction bands for the energy per particle and the pressure in SM and NM obtained by many-body perturbation theory based on χEFT nuclear two and three-body interactions [DHS16], see Fig. 3.3 for illustration. At low densities, the many-body perturbation theory based on χEFT nuclear two and three-body interactions has predicted bands based on 7 Hamiltonians which could equally well reproduce NN phase shifts and the binding energy of the deuteron [DHS16]. These bands are represented in Fig. 3.3 together with a set of models. We compare these bands with three different models which are SLy [CBH$^+$98], ArgonneV18 [LS08] and FSUGold [PC09b]. The binding energies of these models are in good agreement with the χEFT bands in both symmetric matter (SM) and neutron matter (NM). This is also true for the pressure in SM, but there are deviations in NM for FSUGold and SLy models, which predict the pressure above the bands for the high density region. The origin of these deviations lies in the way the χEFT bands for the pressure is defined: It is the boundary calculated from the derivative of the binding energy predicted from the 7 Hamiltonians only. The pressure band does not exhaust all possible density dependence for the binding energy. It is therefore possible for models, such as FSUGold and SLy, to be inside the energy band and outside the pressure band. The pressure band from the χEFT estimation provides a smaller band width than the one which would be based on all the models compatible with the energy band. It is however the width compatible with the 7 Hamiltonians that we will consider in the following. All in all, we can interpret (C3) as an common expectation of the nuclear physics, since it is calculated by using few-body observables at nucleonic scale with their theoretical uncertainties.

In practice, we estimate the following error function $\chi_{2,\chi EFT}$ for each set

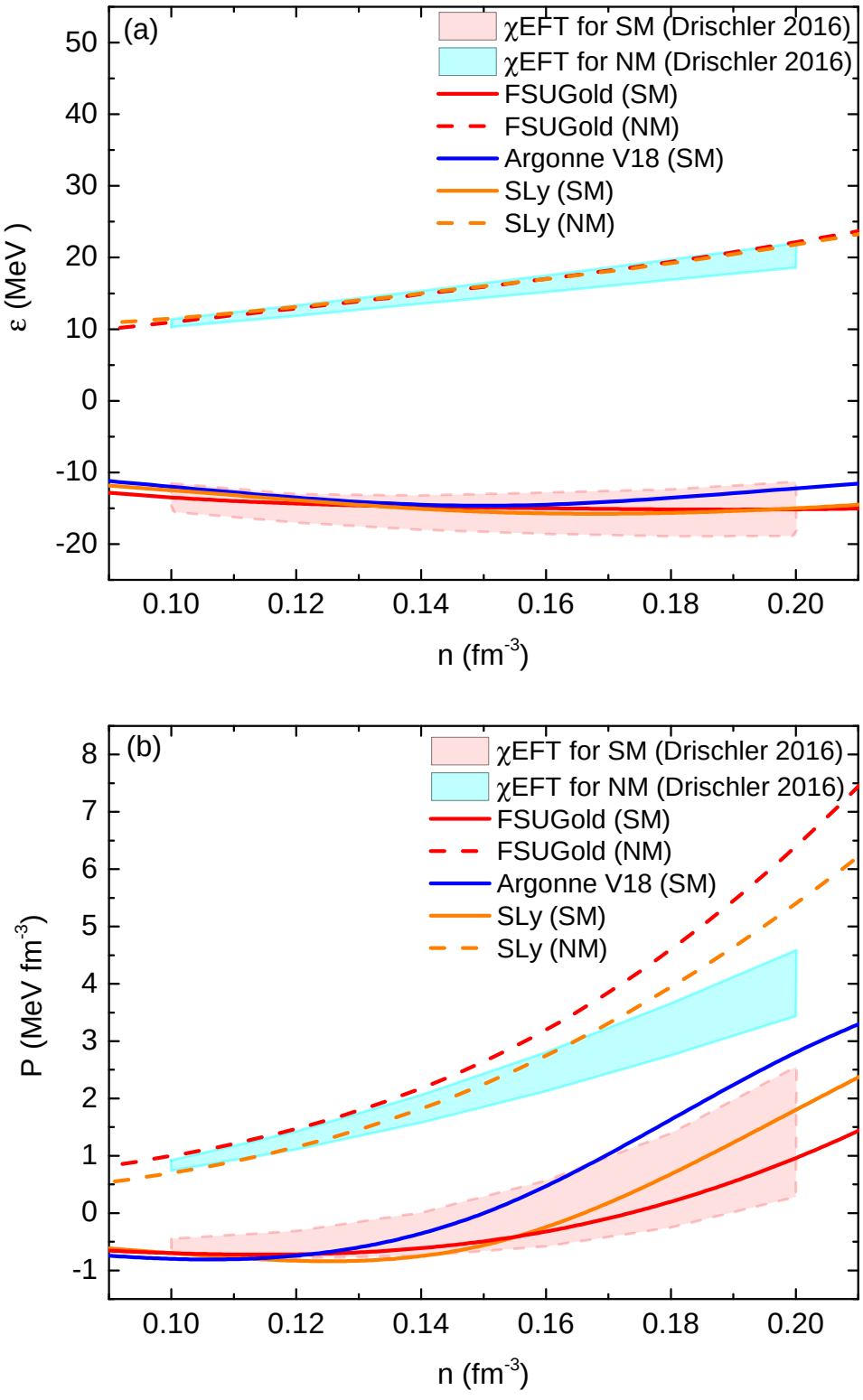

Fig. 3.3: Energy (a) and Pressure (b) distributions calculated by using χEFT from the Ref. [DHS16] for both symmetric matter (SM) and neutron matter (NM).

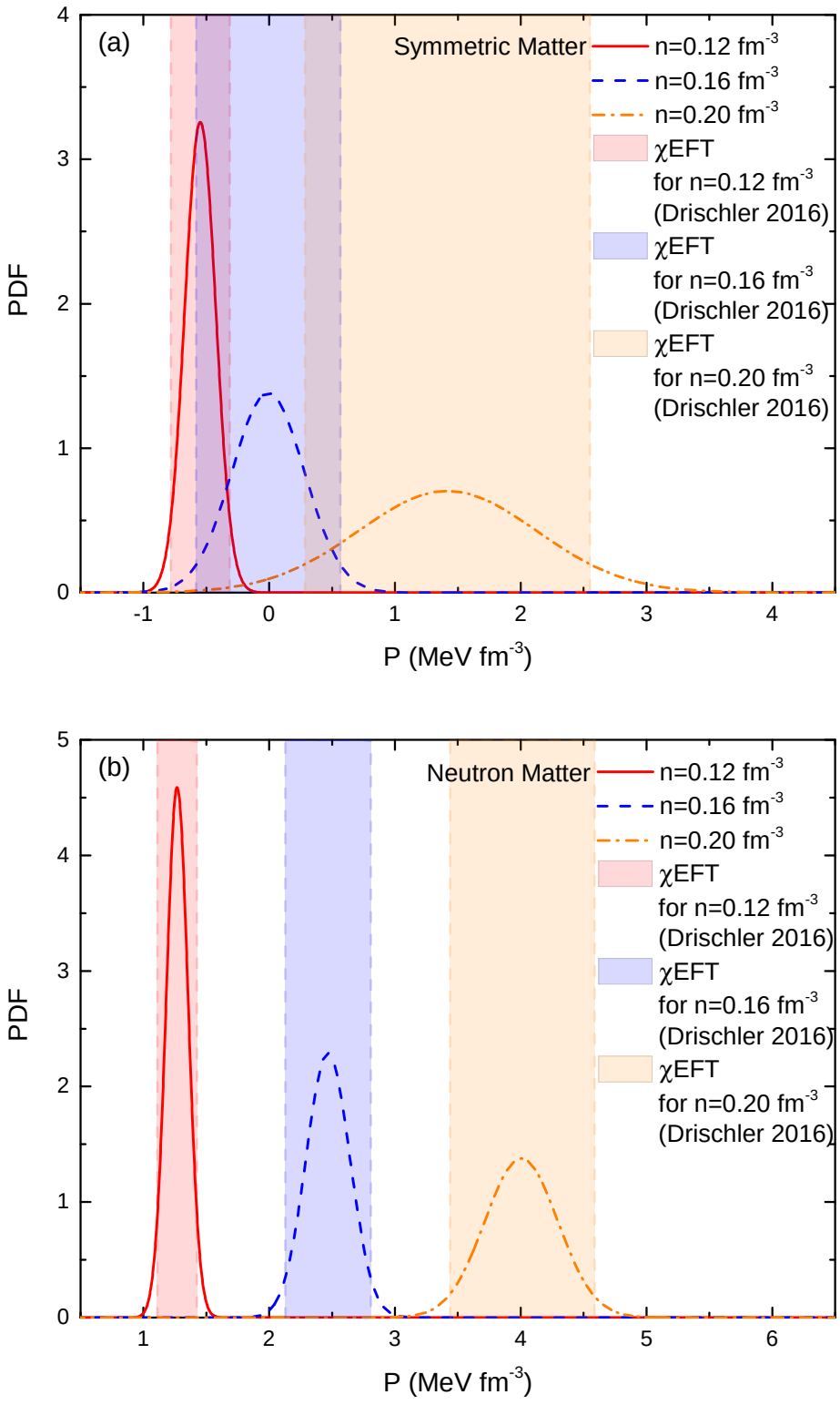

Fig. 3.4: Pressure posterior functions in neutron matter (NM) (a) and symmetric matter (SM) (b) obtained from the constraint C3 associated to the χEFT bands calculated in Ref. [DHS16].

of meta-models,

$$\chi^2_{2,\chi EFT} = \frac{1}{N_{data}} \sum_{i=1}^{N_{data}} \left(\frac{o_i^{data} - o_i(\{a_i\})}{\sigma_i} \right)^2 . \tag{3.61}$$

where $N_{data} = 20$ is the number of data o_i^{data} considered here, $o_i(\{a_i\})$ is the prediction of the model and σ_i is associated to the uncertainties in the data and the accepted model dispersion. We consider 5 density points uniformly distributed between 0.12 fm^{-3} and 0.20 fm^{-3}. If Δ_i is the width of the band at each density point, we fix $\sigma_i = \Delta_i/2$ to ensure that 95% of the models lie inside the band. The small tolerance of 5% of the models outside the band is there to smoothly reduce the probability of marginal meta-models. The associated probability is thus deduced from the usual Gaussian expression,

$$p_{\chi EFT} = \exp\left(-\frac{1}{2} \chi_{2,\chi EFT} \right) . \tag{3.62}$$

An example of likelihood function associated to the pressure for a few densities (0.12, 0.16 and 0.20 fm^{-3}) is shown in Fig. 3.4 for SM (a) and NM (b), where only the constraint C3 is imposed. There is a nice overlap with all models inside χEFT bands with 95% confidence level (shaded regions of Fig. 3.4).

The last constraint (C4) is obtained from a recent analysis of the ISGMR in finite nuclei [KMV12, KM13]. Theoretical models designed to describe finite nuclei and applied to the calculation of the ISGMR centroid energy in ^{120}Sn and ^{208}Pb suggest that the slope of the incompressibility M_c at $n_c = 0.11$ fm^{-3} is well correlated to the experimental data. M_c is defined as

$$M_c = 3n_c \left. \frac{dK(n_0)}{dn_0} \right|_{n_0=n_c} , \tag{3.63}$$

where the incompressibility $K(n_0)$ in SM ($\delta = 0$) is, χ being the compressibility,

$$K(n_0) = \frac{9n_0}{\chi(n_0)} = 9n_0^2 \frac{d^2e(n_0)}{dn_0^2} + \frac{18}{n_0} P(n_0) , \tag{3.64}$$

and the pressure is

$$P(n_0) = n_0^2 \frac{de(n_0)}{dn_0}\,, \tag{3.65}$$

It is found that $M_c = 1050\ \text{MeV} \pm 50\ \text{MeV}$ [KMV12, KM13]. The interesting feature of this parameter is that it is much less model dependent that the more frequently considered incompressibility modulus $K_{sat} = K(n_{sat})$.

In practice, we calculate the value of M_c for each of our meta-models by assigning the following probability,

$$p_{ISGMR} = \exp\left\{-\frac{1}{2}\left(\frac{M_c(\{a_i\}) - 1050}{25}\right)^2\right\}\,, \tag{3.66}$$

where we associate the dispersion ± 50 MeV estimated in Refs. [KMV12, KM13] to the distribution of 95% of the meta-models.

3.10. Concluding Remarks

Since the model dependency is a major problem to understand universal specifications of the nuclear interactions, we used the metamodel which can reproduce majority of models in nuclear physics with the help of the unique set of nuclear EoS parameters. Dealing with nuclear EoS parameters, we got 10 empirical parameters from the Taylor expansion (E_{sat}, n_{sat}, K_{sat}, Q_{sat}, Z_{sat}, E_{sym}, L_{sym}, K_{sym}, Q_{sym}, and Z_{sym}) and 2 parameters from Landau effective mass (m^*_{sat} and Δm^*_{sat}). In order to calculate NS properties and their related probabilities, we defined nuclear EoS parameters in an uniform grid by grouping them as a priori to our calculation. The first one is prior set #1 in which the boundaries of the empirical parameters are unconstrained by any background information or bias. The second one is prior set #2: The boundaries of the empirical parameters are defined from the expectations of the nuclear physics. We then have calculated the β equilibrium nuclear matter by using the meta-model and put them into the general relativistic equations for generating mass radius and tidal deformability. Besides, we defined constraints from nuclear physics (χEFT and ISGMR) and the tidal deformabilities from the GW170817 event.

On the nuclear physic side, we used χEFT predictions at near/below of the saturation density ($n_{\rm sat}$) from Ref. [DHS16] and the experimental value of M_c from the results of the ISGMR from the Refs. [KMV12, KM13]. Additionally, three types of tidal deformability probability distribution functions were considered: TD-LVC-2018, TD-De-2018 and TD-Coughlin-2019. TD-LVC-2018 is the result of the latest analysis from the LIGO-Virgo collaboration [AAA+19] while TD-De-2018 is an independent analysis proposed in Ref. [DFL+18] and TD-Coughlin-2019 is a combined analysis including the electro-magnetic and GRB counterpart observations from Ref. [CDMM19]. Finally, we showed how to generate posterior probabilities of each empirical parameters ($L_{\rm sym}$, $K_{\rm sym}$, $Q_{\rm sat}$ and $Q_{\rm sym}$) and NS properties ($P(2n_{\rm sat})$ and $R_{1.4}$) by taking advantage of the Bayesian framework.

4

Neutron Stars: Properties and Nuclear Equation of State Parameters

4.1. An Overview

Taking advantages of the Bayesian framework, we analyze the impact of the constraints (C2)-(C4) (see Sec. 3.9.1 for details) to analyze each individual contribution coming from $\tilde{\Lambda}$, χEFT and ISGMR on the final posterior probability. Both joint and single posterior probabilities will be shown. The influence of the prior set and two $p_{\tilde{\Lambda}}$ are also discussed. The uncertainty on probabilities are defined as the 68% confidence level around the centroid values of PDF.

In the present statistical analysis, we generate a large enough sample of 294 151 parameter sets for prior set #1 and 203 643 for prior set #2 before the filtering (see Table 3.2). For each set, the probabilities $p_{\tilde{\Lambda}}$, $p_{\chi\mathrm{EFT}}$ and p_{ISGMR} are calculated according to Eqs. (3.60), (3.62) and (3.66). The total likelihood probability is calculated from Eq. (3.59). The reduction from the multi-dimension PDF to the one- or two-parameter probabilities are obtained

from the marginalization principle (see Eqs. (3.57) and (3.58) for details). We analyze the PDF for $L_{\rm sym}$, $K_{\rm sym}$, $Q_{\rm sat}$, $Q_{\rm sym}$, $R_{1.4}$, $P(2n_{\rm sat})$ and the correlations between the parameters $L_{\rm sym}$-$K_{\rm sym}$ and $K_{\rm sat}$-$Q_{\rm sat}$ under the influence of each constraint associated to $p_{\tilde{\Lambda}}$ (TD-LVC-2018, TD-Le-2018 and TD-Coughlin-2019 as named in figures), $p_{\chi\rm EFT}$ (χEFT as named in figures) and $p_{\rm ISGMR}$ (GMR as named in figures). We also investigated the PDF for K_{sat}. However it is not shown here since K_{sat} has only a weak impact on $p_{\tilde{\Lambda}}$.

4.2. Probability Distributions for the Nuclear EoS Parameters

We first study posterior distributions for nuclear EoS parameters: $L_{\rm sym}$, $K_{\rm sym}$, $Q_{\rm sat}$, $Q_{\rm sym}$.

4.2.1 The Slope of Symmetry Energy: L_{sym}

The empirical parameter $L_{\rm sym}$ is the slope of the symmetry energy at $n_{\rm sat}$. In Fig. 4.1 the detailed contributions of the constraints (C2)-(C4) as well as of the role of the $p_{\tilde{\Lambda}}$ and of the prior scenario #1 (panel a) or #2 (panel b) is shown. Note the noticeable tension between the PDF associated to χEFT and the $\tilde{\Lambda}$ one (TD-LVC-2018, TD-Le-2018, TD-Coughlin-2019). Being peaked at higher values for $\tilde{\Lambda}$, the TD-Coughlin-2019 PDF favors slightly larger $L_{\rm sym}$ values than the two others. The influence of the prior is weak, but interestingly, the prior set #1 produces more peaked posteriors than the prior set #2, which is inferred from analyses of nuclear physics models. This could be interpreted as a signal for the marked deviations from nuclear physics predictions: when the constraints from nuclear physics is relaxed (mainly the prior on $K_{\rm sym}$) in the set #1, there is a group of EoS which are clearly favored by the GW tidal deformability and which are located well outside the domain for $L_{\rm sym}$ suggested by nuclear physics.

The GMR constraint has no effect on $L_{\rm sym}$ since the GMR mainly contributes to parameters related to symmetric nuclear matter. The χ EFT constraint gives values for $L_{\rm sym} = 35.37^{+7.09}_{-10.10}/41.83^{+7.33}_{-15.82}$ MeV for the prior set #1/#2, while the tidal deformability favors low or even negative $L_{\rm sym}$ values. For instance, TD-LVC-2018 gives $L_{\rm sym} = 0.00^{+5.00}_{-3.00}/-3.44^{+18.34}_{-2.94}$ MeV

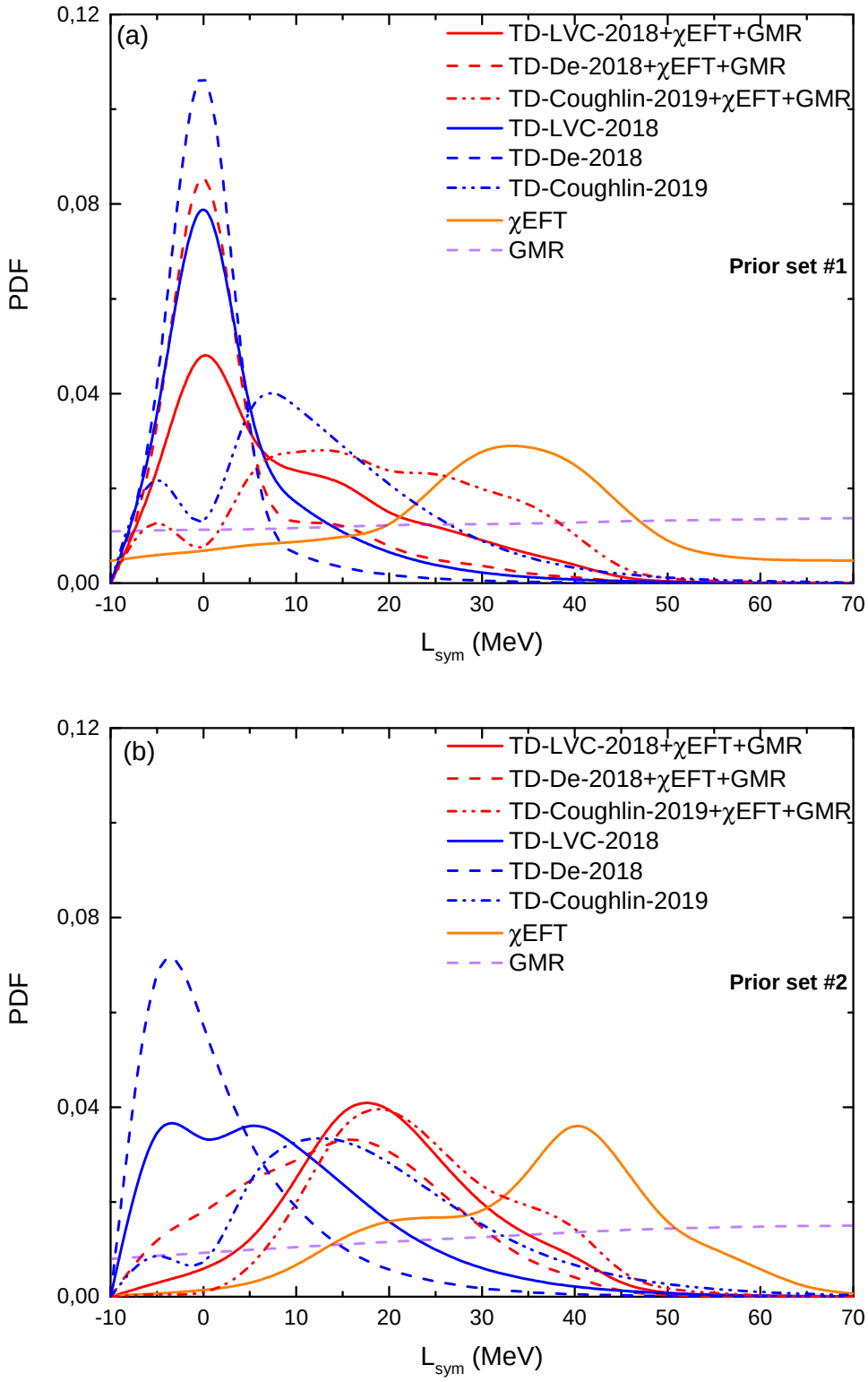

Fig. 4.1: The generated PDFs of $L_{\rm sym}$ for the prior set #1 (a) and the prior set #2 (b).

for the prior sets #1/#2. As expected, the prior set #2 allows some positive values for $L_{\rm sym}$ in the PDF shown in Fig. 4.1.

The joint probabilities naturally favor values for $L_{\rm sym}$ which are intermediate between the two extremes. The most probable value for TD-LVC-2018 (TD-De-2018 and TD-Coughlin-2019) is $L_{\rm sym} = 0.00^{+12.00}_{-4.00}/16.58^{+11.28}_{-6.79}$ MeV ($L_{\rm sym} = 0.00^{+2.01}_{-2.91}/15.47^{+11.24}_{-13.07}$ MeV and $L_{\rm sym} = 17.44^{+15.23}_{-15.23}/16.48^{+14.73}_{-5.43}$ MeV) for the prior set #1/#2. The difference between the prior sets #1 (panel a) and #2 (panel b) reflects the choice for the prior distribution: the upper bound for $K_{\rm sym}$ is fixed to be 1500 MeV for the prior set #1 and only 300 MeV for the prior set #2 (see Table 3.2). The distribution of $L_{\rm sym}$ is thus impacted by the knowledge from the next order empirical parameter $K_{\rm sym}$: The better defined $K_{\rm sym}$, the more peaked $L_{\rm sym}$. The correlation between $L_{\rm sym}$ and $K_{\rm sym}$ will be analysed in Sec. 4.4. Note that the influence of the unknown high order empirical parameters was originally stressed in Ref. [MG19].

Interestingly, the empirical parameter $L_{\rm sym}$ is investigated by a large number of experiments, see Ref. [LH13] and references therein. Confronting the predictions of various nuclear physics experiments, namely neutron skin thickness, heavy ion collisions, dipole polarizability, nuclear masses, giant dipole resonances and isobaric analog states, the values of $L_{\rm sym}$ vary between 30 and 70 MeV [LH13, MCG18a, RMCS18, DFL$^+$18]. It is however interesting to note that a few studies give for $L_{\rm sym}$ lower values, even negative ones, see Refs. [BT85, BFST88], from the charge radius of Sn and Pb isotopes using a droplet model. A detailed analysis based on a few Skyrme and Gogny interactions advocates also for low values for $L_{\rm sym}$ [BB16]. The measurement of the ^{208}Pb neutron skin thickness from the PREX collaboration (Lead Radius Experiment [AAA$^+$12]) is expected to provide a model independent estimation of $L_{\rm sym}$. The experiment has however not yet been very conclusive, with a measured neutron skin thickness $R^{208}_{\rm skin} = 0.33^{+0.16}_{-0.18}$ fm points a lower limit for $L_{\rm sym}$ which is about 20 MeV if one includes the correlation for $L_{\rm sym}$ and $R^{208}_{\rm skin}$ (see Ref. [BB16] for details).

Anticipating the results of Sec. 4.3, there is a strong correlation between the marginalized probability distribution as function of $L_{\rm sym}$ and the one as function of $R_{1.4}$: a low value of $L_{\rm sym}$ coincides with a low radius $R_{1.4}$. Hence the peak at low $L_{\rm sym}$ observed for the tidal deformabilities TD-LVC-2018

and TD-De-2018 reflects that the $\tilde{\Lambda}$ PDF favors NS with small radii. Since the physical implications are clearer in terms of radii, we further discuss the implication of low radii (equivalently low $L_{\rm sym}$) in Sec. 4.3.

4.2.2 The Curvature of the Symmetry Energy: K_{sym}

The empirical parameter $K_{\rm sym}$ encodes the curvature of the symmetry energy at $n_{\rm sat}$. It is different from the parameter K_τ which is defined as the curvature of the binding energy for a fixed proton fraction and can be related to other nuclear EoS parameters as follows [PC09b],

$$K_\tau \equiv K_{\rm sym} - 6L_{\rm sym} - Q_{\rm sat}L_{\rm sym}/K_{\rm sat}\,. \tag{4.1}$$

The isospin dependence of the isoscalar giant monopole resonance (ISGMR) is a natural observable to determine the parameter K_τ [PC09b]. $K_\tau = -550 \pm 100$ MeV has been extracted from the breathing mode of Sn isotopes (Refs. [LGL+07, GLO+07]) and also from isospin diffusion observables in nuclear reactions (Refs. [LC05, LCK08]). If $L_{\rm sym}$ and $Q_{\rm sat}$ were well determined, Eq. (4.1) would provide an equivalence between K_τ and $K_{\rm sym}$. However, the large uncertainties on $L_{\rm sym}$ and $Q_{\rm sat}$ induce a large error bar for $K_{\rm sym}$, of the order of ± 600 MeV [MCG18a]. Besides, the statistical analysis of various theoretical model predict a value $K_{\rm sym} = -100 \pm 100$ MeV [MCG18a]. This result is also in agreement with Ref. [CSY19], which GW analysis is done by using Taylor-Expanded EoSs. On the other hand, there is an experimental determination of $K_{\rm sym}$ by using latest ISGMR values of ^{90}Zr, ^{116}Sn and ^{208}Pb nuclei from Skyrme EDFs: $K_{\rm sym} = -120 \pm 40$ MeV from Ref. [SYC19]. The smaller error bar than the statistical analysis reveals the presence of correlations between $L_{\rm sym}$, $Q_{\rm sat}$ and $K_{\rm sym}$ which do not vary independently from each other.

In our analysis, we explore two priors for $K_{\rm sym}$, one which is pushed until the likelihood probability is quenched (prior set #1), and one which is compatible with the expectation $K_{\rm sym} = -100 \pm 100$ MeV (prior set #2). In Fig. 4.2, the posterior PDFs for $K_{\rm sym}$ are displayed for both prior sets. The posteriors are qualitatively similar between the prior sets #1 and #2. From χEFT, we obtain $K_{\rm sym} = 13.71^{+595.94}_{-265.02}/12.58^{+287.42}_{-410.00}$ MeV for the prior set #1/#2. The tidal deformability however favors positive values

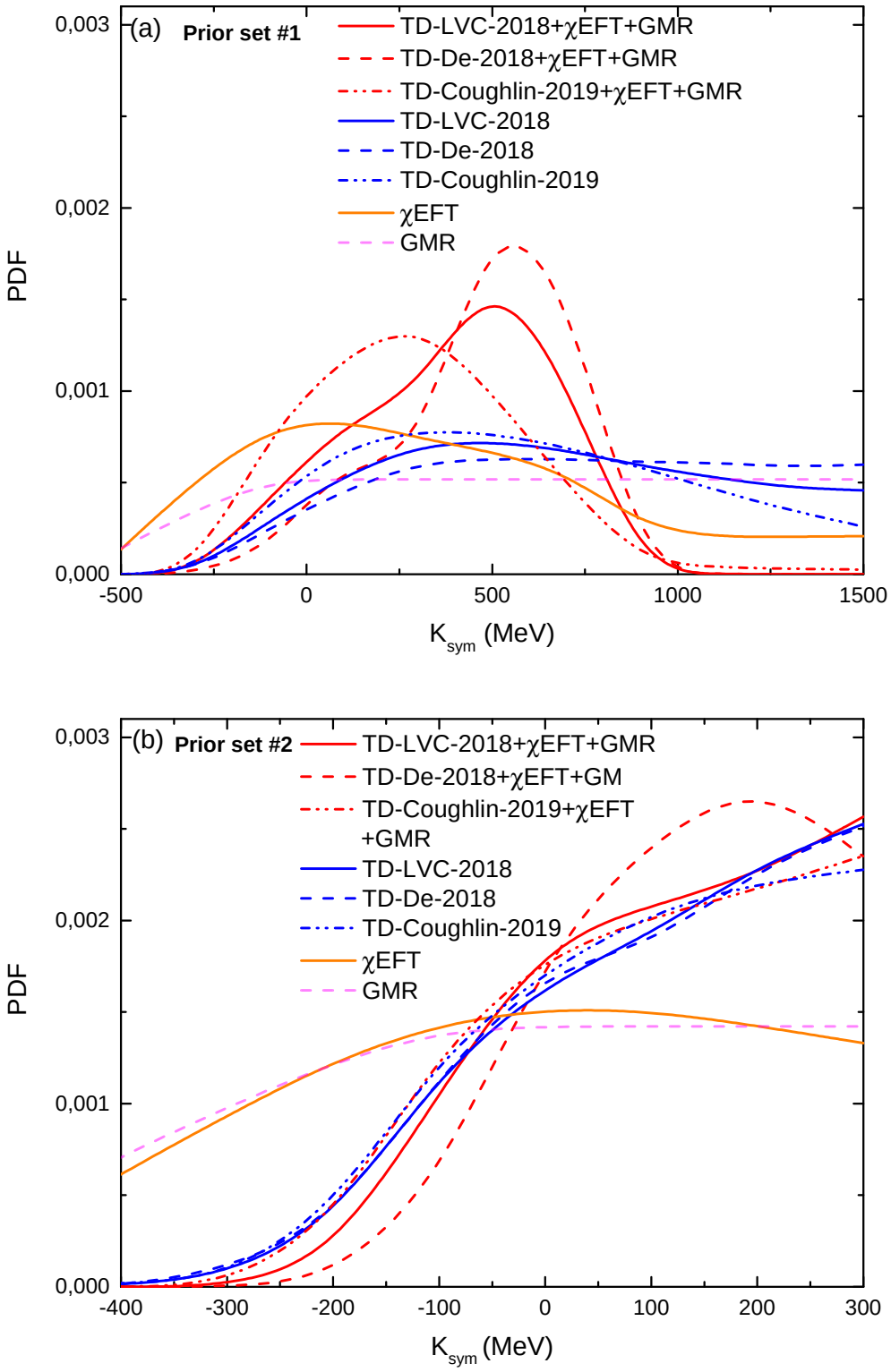

Fig. 4.2: The generated PDFs of $K_{\rm sym}$ for the prior set #1 (a) and #2 (b).

since TD-LVC-2018 (TD-De-2018 and TD-Coughlin-2019) predicts $K_{\rm sym} = 376.44^{+1123.46}_{-400}$ MeV ($K_{\rm sym} = 389.65^{+1110.45}_{-400}$ and $K_{\rm sym} = 273.82^{+888.16}_{-330.93}$ MeV) for the prior set #1. TD-Coughlin-2019 favors values for $K_{\rm sym}$ slightly below the distributions produced by TD-LVC-2018 and TD-De-2018. This can be understood from the $L_{\rm sym}$-$K_{\rm sym}$ anti-correlation originating in the causality condition. Although we cannot define centroid values of $K_{\rm sym}$ since the prior set #2 limits the posteriors to $K_{\rm sym} = 300$ MeV, shifting the prior set #1 to #2 adds 100 MeV to the minimum values of $K_{\rm sym}$. There is also a difference between the expectations from χEFT and from the tidal deformability, while at variance with $L_{\rm sym}$, the differences are here less marked. The impact of the ISGMR is also pretty small.

Finally, the joint probabilities shown in Fig. 4.2 give $K_{\rm sym} = 438.57^{+210.12}_{-210.12}$ MeV ($K_{\rm sym} = 561.20^{+150.23}_{-150.23}$ MeV and $K_{\rm sym} = 261.00^{+237.14}_{-237.14}$ MeV) for TD-LVC-2018 (TD-De-2018 and TD-Coughlin-2019). Considering the $-2\sigma_{\rm min}$ value for each centroid, one can define the lower limit for $K_{\rm sym}$: $K_{\rm sym} \geq 18.33$ MeV for TD-LVC-2018, $K_{\rm sym} \geq 260.74$ MeV for TD-De-2018 and $K_{\rm sym} \geq -213.28$ MeV for TD-Coughlin-2019. It should be noted that several analysis have been done on the bounds of $K_{\rm sym}$, providing $K_{\rm sym} \geq -500$ MeV to $K_{\rm sym} \geq -250$ MeV depending on considered models [MAD+17, CCK+09, YS06, DL09]. Besides, an interesting work about the lower limit of $K_{\rm sym}$ is the Unitary Gas (UG) limit for the NM, which is in a good agreement with our predictions [TLOK17]. Since the ground state energy per particle in the UG is proportional to the Fermi energy, one can describe a forbidden zone for energy per particle of EoS in terms of the Fermi energy for neutron matter. In Ref. [TLOK17], a suitable conjecture imposed from the UG limit is shown: $E_{\rm NM} \geq E_{\rm UG} = E^0_{\rm UG} n_0^{2/3}$. Eventually it leads to $K_{\rm sym} \geq -2E^0_{\rm UG} - K_{\rm sat}$ where $E^0_{\rm UG} = 12.6$ MeV is the Fermi energy of neutrons including Bertsch parameter ξ_0. Using the average value of $K_{\rm sat} = 230 \pm 20$ MeV (see Ref. [MCG18a] for a complete analysis about the parameter $K_{\rm sat}$), a minimum limit for $K_{\rm sym}$ can be obtained: $K_{\rm sym} \geq -255.2 \pm 20$ MeV. However, contrary to the UG, the NM includes effective-range effects and interactions in higher partial waves especially for densities $n \geq n_{\rm sat}$. Therefore, it is expected that the lower limit of $K_{\rm sym}$ should be higher then the one obtained from the UG.

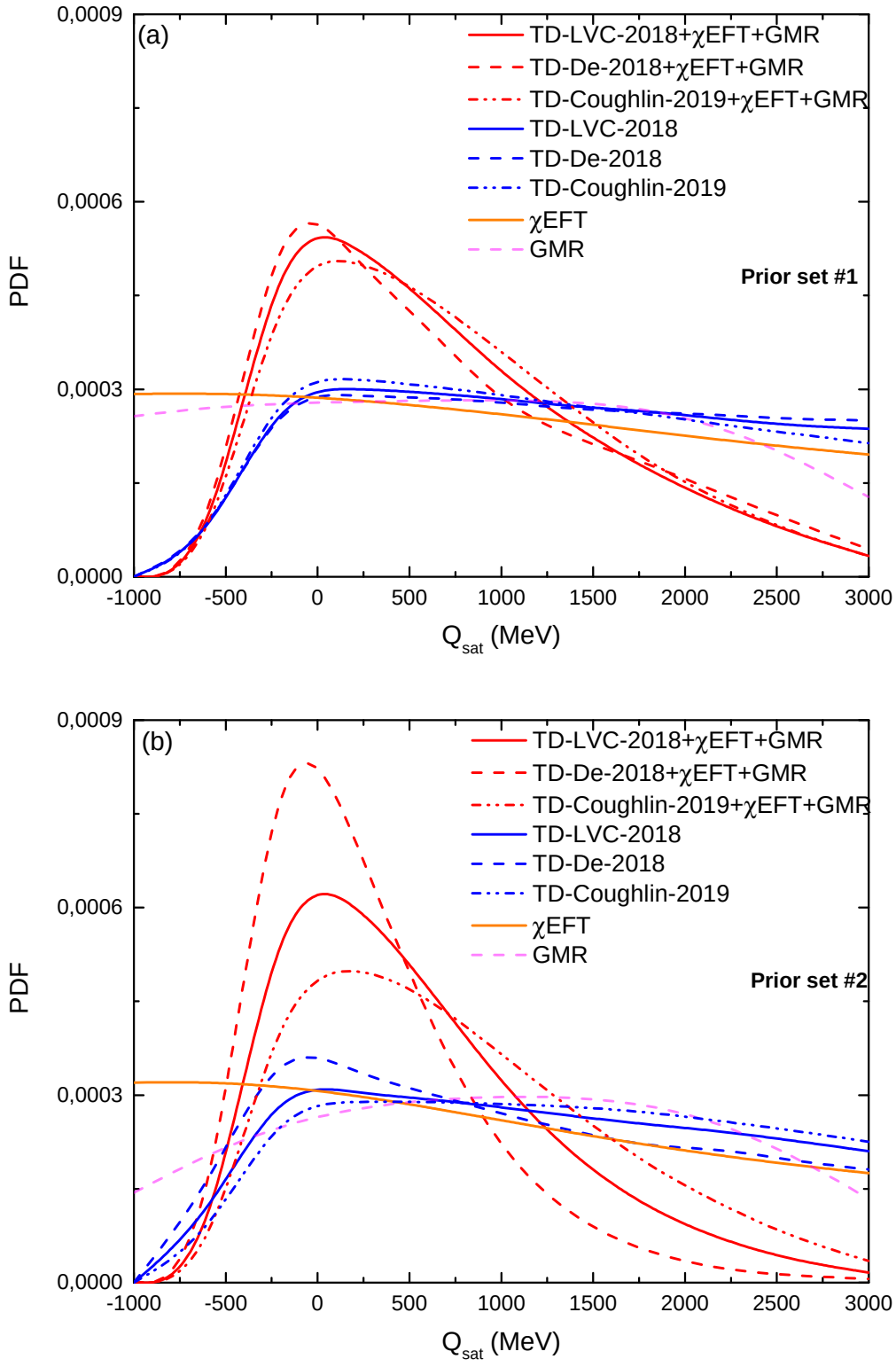

Fig. 4.3: The generated PDFs of $Q_{\rm sat}$ for the prior set #1 (a) and #2 (b).

4.2.3 The Skewness Parameter for Symmetric Matter: Q_{sat}

The skewness parameter $Q_{\rm sat}$ is the lowest order empirical parameter in SM which is almost unconstrained. While the incompressibility modulus $K_{\rm sat}$ is well defined, the density dependence of the incompressibility is poorly known and there are very scarce experimental analysis to determine its value. An analysis based on charge and mass radii of the Sn isotopes concluded that either $Q_{\rm sat} \approx 30$ MeV or $L_{\rm sym} \approx 0$ MeV [BFST88]. Another analysis based on the Skyrme functionals which are fitted according to the breathing modes concluded that $Q_{\rm sat} \approx 500$ MeV [FPT97]. A systematic analysis also suggests $Q_{\rm sat} = 300 \pm 400$ MeV based on a large number of theoretical models of the literature [MCG18a].

There are also other analysis based on various models from the RMF and SHF frameworks in which the tidal deformability of GW170817 constrains the parameter M_0 of the nuclear EoS defined as [MAF+18, CSY19],

$$M_0 = M(n_{\rm sat}) = 3n_{\rm sat}\frac{dK(n_0)}{dn_0}\bigg|_{n_0=n_{\rm sat}} . \tag{4.2}$$

The following predictions were obtained for M_0: $2254 \leq M_0 \leq 3631$ MeV or $1926 \leq M_0 \leq 3768$ MeV depending on $L_{\rm sym}$ [MAF+18] and $1526 \leq M_0 \leq 4971$ MeV [CSY19].

Using the relation $M_0 = 12K_{\rm sat} + Q_{\rm sat}$ (see Ref. [ASA15]), one can make a prediction for $Q_{\rm sat}$ by considering adequate $K_{\rm sat}$ value. Considering $K_{\rm sat} = 230 \pm 20$ MeV from Ref. [MCG18a], then $-800 \leq Q_{\rm sat} \leq 1100$ MeV for Ref. [MAF+18] and $-1200 \leq Q_{\rm sat} \leq 2100$ MeV for Ref. [CSY19].

In Fig. 4.3, the posterior PDFs of $Q_{\rm sat}$ are presented. It is clear that χEFT does not constrain $Q_{\rm sat}$. This is because $Q_{\rm sat}$ influences the EoS at densities well above saturation density, while the data from χEFT are relevant until $n_0 = 0.2$ fm^{-3}. The empirical parameter $Q_{\rm sat}$ is however better constrained by both the tidal deformability from GW170817 and the ISGMR while the predictions from prior set #1 and #2 are very similar. Despite that all posteriors of tidal deformability considering TD-LVC-2018, TD-De-2018 or TD-Coughlin-2019 independently agree on the lower limit of $Q_{\rm sat}$ ($Q_{\rm sat}^{\rm min} \approx -500$ MeV), the higher boundary of $Q_{\rm sat}$ requires by applying both the tidal

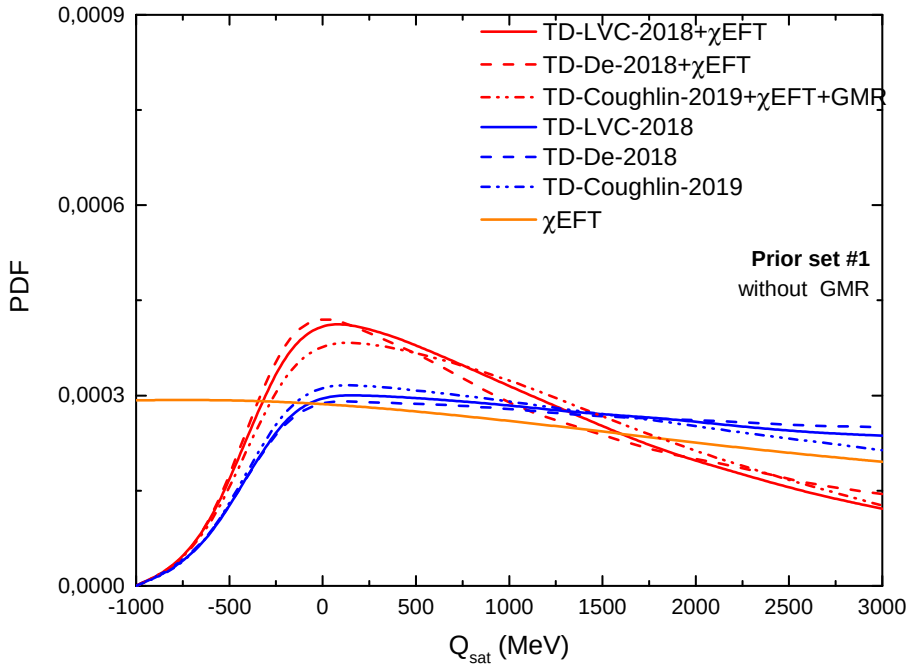

Fig. 4.4: Same as Fig. 4.3 for the prior set #1 without ISGMR.

deformability and the ISGMR constraints. The results from the joint posteriors are $Q_{\rm sat} = -180^{+1222}_{-175}/-162^{+935}_{-175}$ MeV ($Q_{\rm sat} = -220^{+1130}_{-150}/-214^{+652}_{-153}$ MeV and $Q_{\rm sat} = 93^{+1365}_{-250}/200^{+1107}_{-445}$ MeV) for TD-LVC-2018 (TD-De-2018 and TD-Coughlin-2019) for the prior set #1/#2, respectively.

Furthermore, we also study the impact of switching off the ISGMR constraint for the prior set #1 on the posterior probability in order to see its global effect on the joint posteriors, see Fig. 4.4. The new the joint posteriors are $Q_{\rm sat} = -134^{+1757}_{-250}$ MeV ($Q_{\rm sat} = -189^{+1800}_{-200}$ MeV and $Q_{\rm sat} = -130^{+2000}_{-250}$ MeV) for TD-LVC-2018 (TD-De-2018 and TD-Coughlin-2019). Removing the ISGMR constraints increases the uncertainty on the joint posteriors for $Q_{\rm sat}$ by about 500 MeV. This shows that M_c (see Sec. 3.9.3 for details) is an important constraint for defining the value of $Q_{\rm sat}$. Furthermore, a reduction of the uncertainty on M_c, by a systematical comparison of the meta-model predictions in finite nuclei for instance, would imply a more precise estimation for the empirical parameter $Q_{\rm sat}$.

4.2.4 The Skewness Parameter for Neutron Matter: Q_{sym}

The nuclear EoS parameter $Q_{\rm sym}$ controls the skewness of the symmetry energy at $n_{\rm sat}$. An analysis based on the various theoretical models (Skyrme Hartree Fock, Relativistic Hartree Fock, RMF and χEFT) suggests $Q_{\rm sym} = 0 \pm 400$ MeV but still its value runs over a large range from models to models, e.g. $-2000 \leq Q_{\rm sym} \leq 2000$ MeV [MCG18a]. Since $Q_{\rm sym}$ contributes to the EoS at supra-saturation densities, it is quite difficult to estimate the value of this empirical parameter from low-density χEFT or from terrestrial experiments in finite nuclei like the ISGMR. It furthermore requires systems which probe asymmetric nuclear matter. It is therefore completely unknown from nuclear physics traditional approach and one could easily understand that χEFT and ISGMR constraints are ineffective for constraining $Q_{\rm sym}$, as shown in Fig 4.5. The most effective constraint is provided by the tidal deformability, but it is interesting to remark that even if χEFT and ISGMR do not provide constraints taken individually, the joint posterior, including tidal deformability, χEFT and ISGMR, is narrower than the probability distribution considering $\tilde{\Lambda}$ alone. The joint posteriors from TD-LVC-2018 (TD-De-2018 and TD-Coughlin-2019) favor the following values: $Q_{\rm sym} = -270^{+1690}_{-1126} / -169^{+1376}_{-748}$ MeV ($Q_{\rm sym} = -677^{+1159}_{-597} / -376^{+835}_{-477}$ MeV and $Q_{\rm sym} = 218^{+1942}_{-1576} / 276^{+1815}_{-1242}$ MeV) for the prior set #1/#2. It shall also be noted that there is a marked correlation between $K_{\rm sym}$ and $Q_{\rm sym}$: the prior set #2, considering a tighter prior for $K_{\rm sym}$, (compared to the prior set #1) also predicts a narrower peak for $Q_{\rm sym}$. Although, the joint posteriors have a large uncertainty on $Q_{\rm sym}$, we point out that a more accurate PDF for $\tilde{\Lambda}$, could lead a better determination for $Q_{\rm sym}$.

4.3. Posteriors for Neutron Star Observables: Radius and Pressure

Let us discuss the impact of the posteriors on the NS properties. In the present section, we discuss the impact of the constraints on the posterior distribution for the NS radius at $1.4 M_\odot$: $R_{1.4}$, and the pressure at $2 n_{\rm sat}$: $P(2 n_{\rm sat})$.

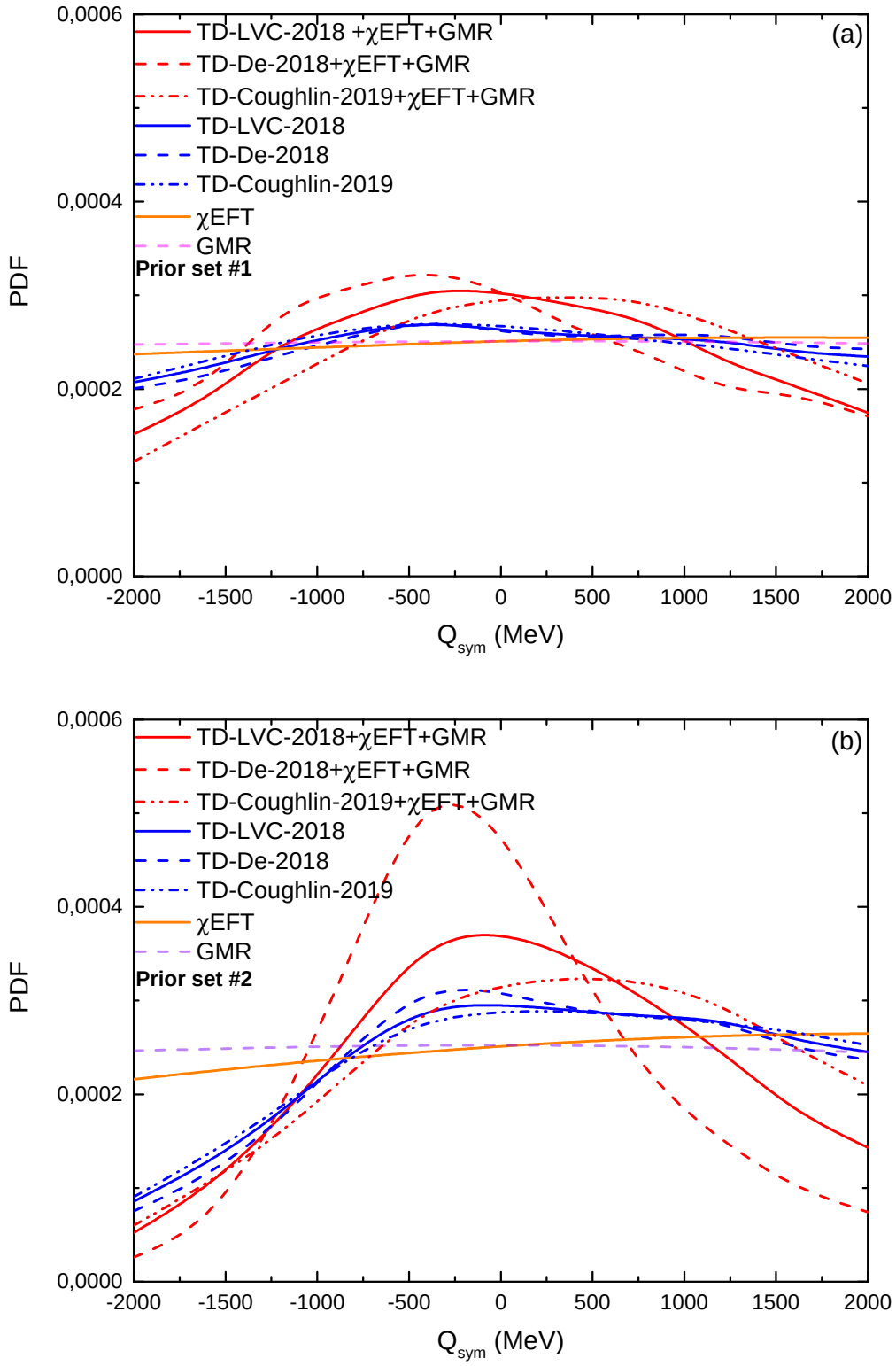

Fig. 4.5: The generated PDFs of $Q_{\rm sym}$ for the prior set #1 (a) and #2 (b).

4.3.1 The Neutron Star Radius at $1.4M_\odot$: $R_{1.4}$

As discussed in Sec. 3.2, X-ray observations of NS such as thermal emissions or X-ray bursts, advocate for the following limits of NS radii: $7.9 \leq R_{1.4} \leq 12.66$ km [SLB10, LS14, ÖF16, MDDS+18, dGM+19]. Moreover, GW analysis based on various models concluded to $11.80 \leq R_{1.4} \leq 12.80$ km in Ref. [KLK+18], $12.00 \leq R_{1.4} \leq 13.70$ km in Refs. [AGKV18, MWRSB18], and $11 \leq R_{1.4} \leq 13$ km considering $100 \leq \tilde{\Lambda} \leq 600$ in Ref. [LH18]. While being consistent among them, these predictions are slightly different, reflecting the small model dependence in the theoretical models employed.

We show in Fig. 4.6 the posteriors PDFs for the NS radius $R_{1.4}$ for the different individual constraints and for the joint one. The predictions from TD-LVC-2018 and TD-De-2018 are $R_{1.4} = 10.65^{+2.1}_{-0.26}/10.51^{+1.29}_{-0.17}$ km for the prior set #1/#2 at variance with the prediction from TD-Coughlin-2019 $R_{1.4} = 13.13^{+0.51}_{-0.51}$ km, which are consistent with the predictions from nuclear physics (χEFT): $R_{1.4} = 12.99^{+0.76}_{-1.21}/12.72^{+0.82}_{-0.61}$ km for the prior set #1/#2. If the $\tilde{\Lambda}$ distribution suggested by TD-LVC-2018 and TD-De-2018 is correct, there is a difference of about 1.5 km for the most probable radii compared to the prediction from χEFT. This difference is larger that the standard deviation for each PDF, indicating a possible source of tension, as also observed for the PDF of $L_{\rm sym}$. Finally, the joint probabilities shown in Fig. 4.6 give $R_{1.4} = 11.00^{+1.30}_{-0.25}/10.98^{+1.90}_{-0.25}$ or $R_{1.4} = 12.00^{+0.30}_{-1.25}/10.98^{+1.90}_{-0.25}$ km ($R_{1.4} = 11.00^{+1.25}_{-0.25}/10.99^{+1.70}_{-0.25}$ or $R_{1.4} = 12.00^{+0.25}_{-1.25}/10.99^{+1.70}_{-0.25}$ km and $R_{1.4} = 12.91^{+0.43}_{-0.43}/12.50^{+0.54}_{-0.27}$ km) for TD-LVC-2018 (TD-De-2018 and TD-Coughlin-2019) for the prior set #1/#2. Interestingly, the joint posteriors suggested by TD-LVC-2018 and TD-De-2018 predicts a double peak, where the first one is around 11 km and the second one is around 12 km for the prior set #1.

Our prediction for $R_{1.4}$ favored by GW170817 only (TD-LVC-2018 and TD-De-2018 but not TD-Coughlin-2019) is very similar to the one recently performed in Ref. [CTB+19], where $R_{1.4} = 11 \pm 1$ km is obtained from the analysis of the GW waveforms and the constraint from the maximum mass. This is not entirely surprising: even if the analysis is different from ours, namely relaying on the bare data of Ref. [CTB+19] and based on the post-processed analysis in terms of $\tilde{\Lambda}$ in our case, the physics issued from GW is

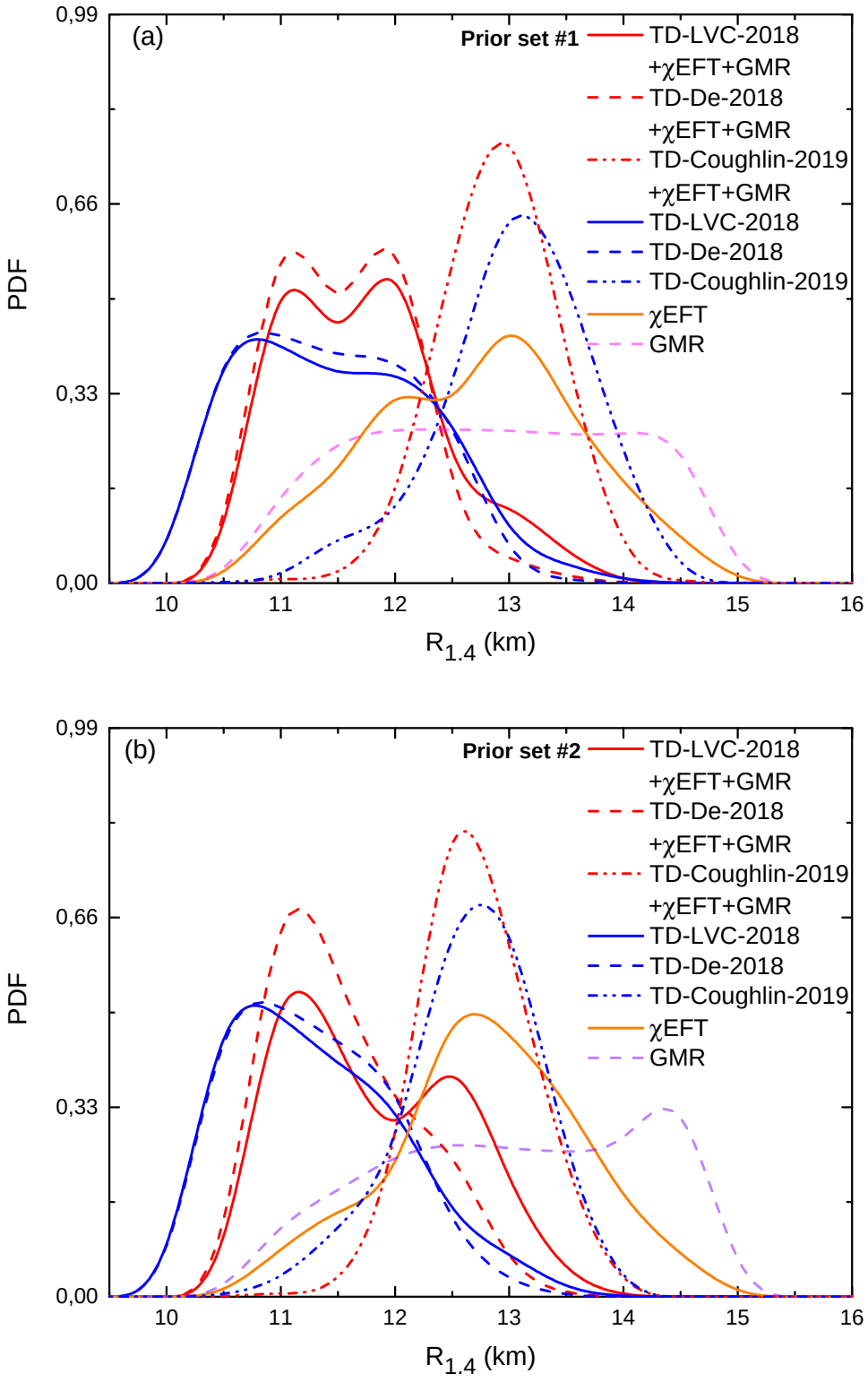

Fig. 4.6: The generated PDFs of NS radius $R_{1.4}$ for the prior set #1 (a) and #2 (b).

the same. A low value for the radius $R_{1.4} \approx 11$ km is marginal with nuclear physics (represented here by the χEFT and GMR constraints). This results of low value for the radius suggest that the low peak value for $\tilde{\Lambda} \approx 200$ needs a softening of the EoS that nuclear degrees of freedom could not produce for the typical masses estimated from GW170817, which are around $1.3-1.5M_{\odot}$ (coinciding to central densities of about $2-3\rho_{sat}$). This softening could be obtained by the onset of new degrees of freedom, such as pion or kaon condensation, hyperonization of matter or a first order phase transition to quark matter. The requirement to reach about $2M_{\odot}$ also limits the softening, which could be obtained assuming a transition to quark matter [MTHR19].

4.3.2 The Pressure at $2n_{sat}$: $P(2n_{sat})$

It was recently proposed to analyze the constraint from the tidal deformability from GW170817 in terms of the pressure at $2n_{\rm sat}$ [AAA+18]. An analysis done by Ligo-Virgo collaborations [AAA+18] obtained (with 90% confidence interval) a pressure $P(2n_{\rm sat}) = 21.80^{+15.76}_{-10.55}$ MeV fm^{-3} where the error bars represent 90% confidence level (corresponding to $P(2n_{\rm sat}) = 21.80^{+9.58}_{-6.41}$ MeV fm^{-3} for 65% confidence level). Another analysis based on χEFT [LH18] concluded that $15 \leq P(2n_{\rm sat}) \leq 25$ MeV fm^{-3} considering $100 \leq \tilde{\Lambda} \leq 600$.

We thus further extend this approach by also imposing nuclear physics constraints on top of the tidal deformability, in the same spirit of the previous plots (Fig.4.7). We have also added $P(2n_{\rm sat})$ from Ref. [AAA+18] for comparison. The constraints from χEFT and ISGMR generate a rather flat distribution between the boundaries with small and marginal peaks. The tidal deformability imposes slightly stronger constraints, with $P(2n_{\rm sat}) \geq 15$ MeV for the prior set #1 and #2. It is however interesting to note that here also, the joint posteriors predicts a peak narrower when including all three constraints: $P(2n_{\rm sat}) = 24.61^{+24.42}_{-5.00}/26.02^{+13.58}_{-5.00}$ MeV fm^{-3} ($P(2n_{\rm sat}) = 23.69^{+27.95}_{-5.00}/25.00^{+7.82}_{-5.21}$ MeV fm^{-3} and $P(2n_{\rm sat}) = 25.00^{+19.91}_{-5.00}/30.00^{+18.29}_{-6.69}$ MeV fm^{-3}) for TD-LVC-2018 (TD-De-2018 and TD-Coughlin-2019) for the prior set #1/#2. Although the centroid value of each tidal deformabilities are quite similar between the priors, the prior set #2 gives less uncertainty in the TD-LVC-2018 and TD-De-2018 cases. All in all, we conclude that the limits

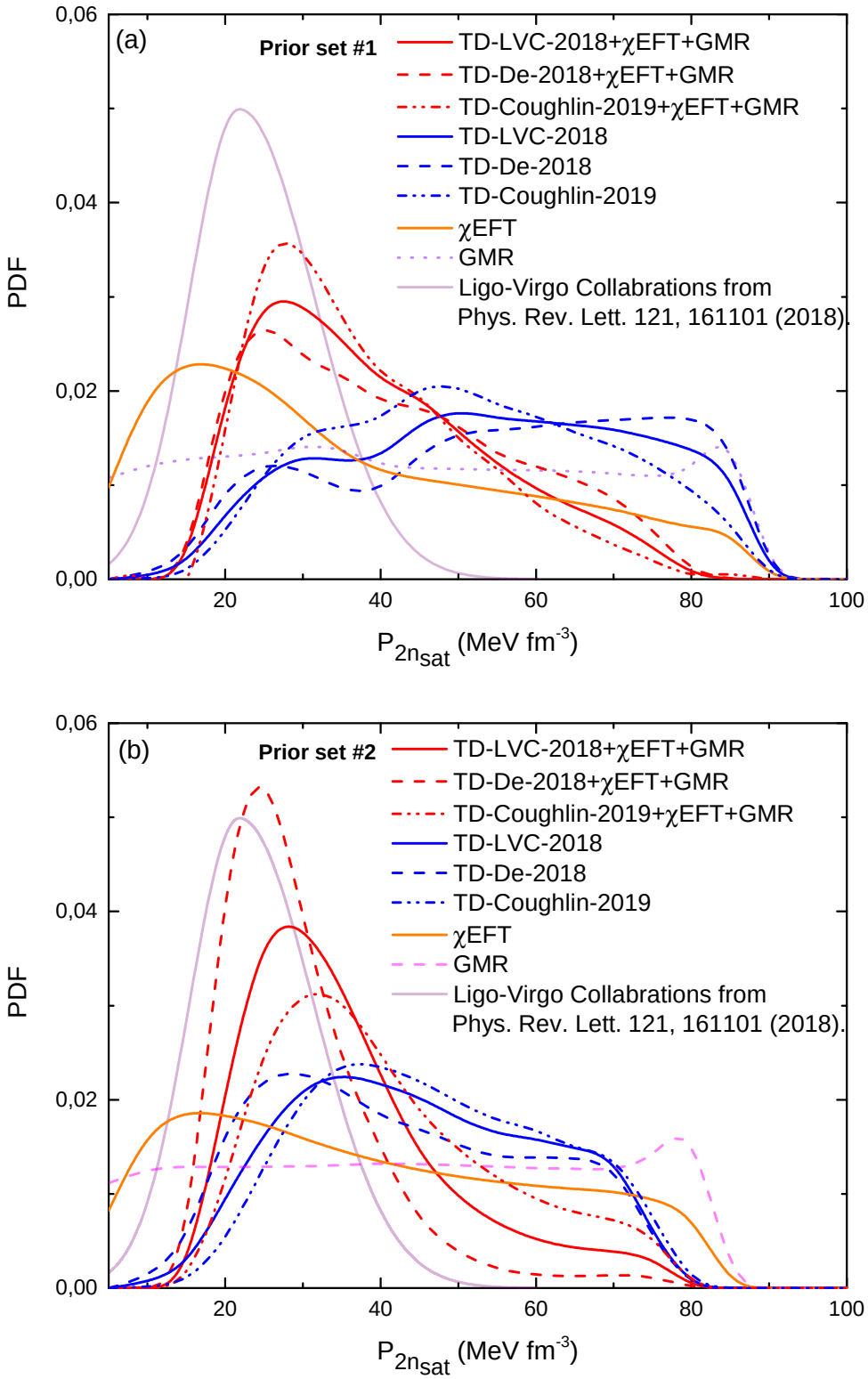

Fig. 4.7: The generated PDFs of the pressure at $2n_{\rm sat}$ for the prior set #1 (a) and #2 (b).

of the pressure at $2n_{\rm sat}$ is: $19 \leq P(2n_{\rm sat}) \leq 50$ MeV fm^{-3}. Besides, considering the prior set #2 which has a tighter bound for $K_{\rm sym}$, our prediction is in good agreement with the one proposed from Ligo-Virgo (Ref. [AAA+18]). The smaller dispersion is shown to come from the ISGMR, χEFT and tidal deformability considered all together. However, there is a noticeable difference between PDFs of GW and the one from Ligo-Virgo where polytropic EoSs are used to obtain pressure profiles [AAA+18]. The reason of this difference could be impacted by higher order terms of the symmetry energy which may not supported by polytropic EoSs considered by Ligo-Virgo. There is however no inclusion of quark phase transition in the present analysis, which is expected to increase the width of the prediction [TMR18, TMR19].

4.4. Analysis of the Correlations Among the Nuclear Empirical Parameters

It is interesting to study the correlations among empirical parameters since they could sometimes reveal physical and universal correlations, or spurious correlations generated by the reduced number of free parameters. Therefore, the correlations $E_{\rm sym} - L_{\rm sym}$, $L_{\rm sym} - K_{\rm sym}$ and $K_{\rm sat} - Q_{\rm sat}$ are widely discussed [KMV12, KM13, MAD+17, CCK+09, YS06, DL09, VPPR09, DMPV11, DZGL12, SDLmcD14]. For instance, the correlation between $K_{\rm sat}$ and $Q_{\rm sat}$ typically found for Skyrme and Gogny interactions, is related to the presence of a single density dependent term in the nuclear force [KMV12, KM13]. Hence, a recent analysis of several of these correlations can be found in Ref. [MG19]. In the present section we provide an analysis on $L_{\rm sym} - K_{\rm sym}$ and $K_{\rm sat} - Q_{\rm sat}$ correlations under the influence of each constraint associated to $p_{\tilde{\Lambda}}$, $p_{\chi\rm EFT}$ and $p_{\rm ISGMR}$. The correlation between $E_{\rm sym}$ and $L_{\rm sym}$ is not shown here since we used a fixed $E_{\rm sym}$ value for prior sets #1/#2 (see Table 3.1 for details).

4.4.1 The Correlation between L_{sym} and K_{sym}

We first explore the correlation between $L_{\rm sym}$ and $K_{\rm sym}$ (see Figs. 4.8), which was also explored in Refs. [MAD+17, CCK+09, YS06, DL09, VPPR09, DMPV11, DZGL12, SDLmcD14]. We remind that the influence of the prior

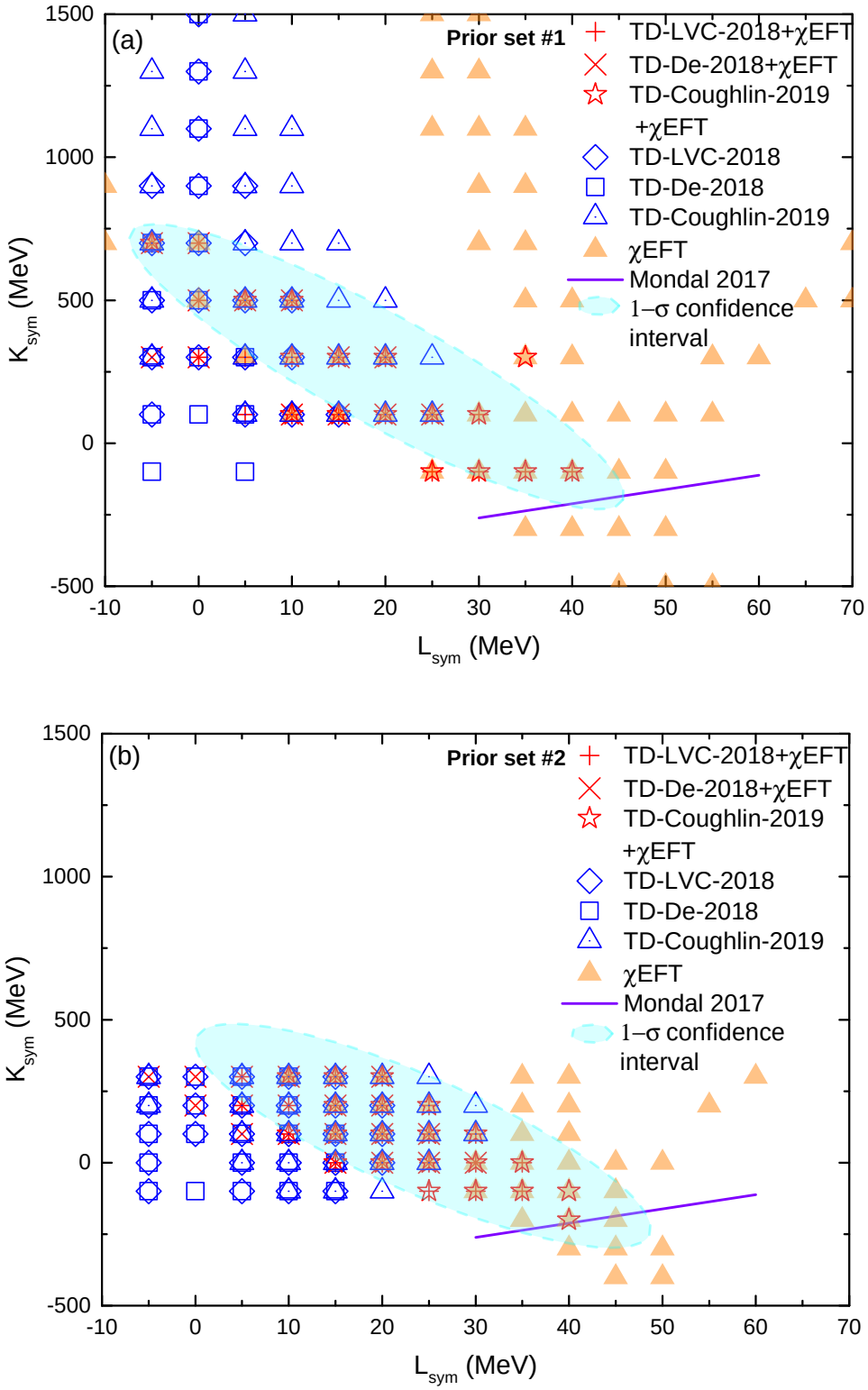

Fig. 4.8: The values of the $L_{\rm sym}$ and $K_{\rm sym}$ inside of the 1-σ probability for the prior set #1 (a) and #2 (b) with the fit from Ref. [MAD+17].

sets on the PDF related to $L_{\rm sym}$ (Fig. 4.1), was suggesting the presence of a correlation between $L_{\rm sym}$ and $K_{\rm sym}$. Here also we find a noticeable difference between the $L_{\rm sym} - K_{\rm sym}$ domain favored by the GW constrain (low $L_{\rm sym}$ values) and the one favored by the χEFT one (high $L_{\rm sym}$ values). The lower bounds in $L_{\rm sym}$ and $K_{\rm sym}$ are imposed by the stability and $M_{\rm max}^{\rm obs}$ constraints, while the upper bounds are fixed by the causality one. Note that the $L_{\rm sym} - K_{\rm sym}$ domain favored by the TD-De-2018 $\tilde{\Lambda}$-PDF is a bit smaller than the one favored by TD-LVC-2018. Moreover, the prior set #2 exploring a smaller parameter space than the prior set #1 (see Tab. 3.2), the correlation domain is smaller for prior set #2 compared to #1. Despite this main difference, there is still a small but noticeable impact of the prior set.

Exploring a large set of RMF and Skyrme EDFs, the following relation $K_{\rm sym} = \beta(3E_{\rm sym} - L_{\rm sym}) + \alpha$, with $\beta = -4.97 \pm 0.07$ and $\alpha = 66.80 \pm 2.14$ MeV, was suggested [MAD+17]. Fixing $E_{\rm sym} = 32$ MeV (actually $E_{\rm sym} = 32.1 \pm 0.3$ MeV is taken in Ref [MAD+17], but we keep fixed $E_{\rm sym} = 32$ MeV in our analysis, for details see Table. 3.1 and related explanations), this correlation is shown in Fig. 4.8 with the legend Mondal 2017. This correlation was shown to originate from the physical condition that the energy per particle in NM should be zero at zero density [MG19]. Using the meta-model, the validity of this correlation has been confirmed and the contribution of higher order parameter ($Q_{\rm sym}$, $Q_{\rm sat}$, $Z_{\rm sym}$ and $Z_{\rm sat}$) has also been investigated, adding about 200 MeV uncertainty to $K_{\rm sym}$ [MG19]. There is an overlap between the Mondal 2017 correlation line and the χEFT favored domain, as expected (Fig. 4.8). However, the χEFT favored domain is much larger since we have considered only the $n_0 \geq 0.12$ fm^{-3} energy band in NM. The constrain at very low density is thus not included in the χEFT favored domain.

We have also analyzed the impact of the ISGMR constraints on the $L_{\rm sym} - K_{\rm sym}$ correlation, but since this is a correlation among isovector empirical parameter, there is no impact of the ISGMR constraint.

Finally, the blue contours in Figs. 4.8 represent the 1σ ellipses including both the GW and χEFT constraints together while blue symbols are tidal deformability and yellow symbols are χEFT PDFs for the 1σ probability interval on $L_{\rm sym} - K_{\rm sym}$ plane. Note that, left branch of χEFT PDF supports the low $L_{\rm sym}$ high $K_{\rm sym}$ case and overlaps with PDfs of tidal deformability, creating the 1σ ellipses. This ellipse is only weakly dependent on the prior

sets #1 and #2. We therefore propose a new correlation which reproduces the joint probability as,

$$K_{\rm sym} = \alpha_1 L_{\rm sym} + \beta_1, \tag{4.3}$$

where $\alpha_1 = -18.83^{+3.00}_{-2.00}$ and $\beta_1 = 616^{+140}_{-180}$ MeV.

4.4.2 The Correlation between K_{sat} and Q_{sat}

The second correlation we analyze here is the one between $K_{\rm sat}$ and $Q_{\rm sat}$. The physical origin of this correlation is related to the ISGMR constraint reflected into the parameter M_c defined below saturation density at $n_c \approx 0.11$ fm^{-3} [KMV12, KM13]. Setting $n_0 = n_c$ in the isoscalar channel ($\delta = 0$) of the meta-model, one can obtain the following relation: $M_c \approx 4.6K_{\rm sat} - 0.18Q_{\rm sat} - 0.007Z_{\rm sat}$ [MG19]. Fixing $M_c = 1050 \pm 100$ MeV, this relation induces a correlation between $K_{\rm sat}$ and $Q_{\rm sat}$. However, a general analysis based on meta-model shows that this correlation is rather weak from the various EDFs, and the parameter $Q_{\rm sat}$ is yet unknown [MG19]. Since $Q_{\rm sat}$ can be constrained by the GW data, it is worth analyzing the correlation $K_{\rm sat} - Q_{\rm sat}$ under the influence of GWs.

In Figs. 4.9, the $K_{\rm sat} - Q_{\rm sat}$ correlations are shown for various constraints with a spurious correlation found for Skyrme and Gogny EDFs from Ref. [KM13] as the legend Khan 2013. The source of this correlation is the density dependent term from Skyrme and Gogny EDFs(see Ref. [KM13] for details). First, it should be stressed that the χEFT constraint is included for all joint posteriors, but its effect was found negligible in this case. The domain allowed from the ISGMR constraint is shown with purple large dots, as previously discussed. A lower bound $Q_{\rm sat} \geq -500$ MeV is shown, originating from the GW constraint has previously discussed in Fig. 4.3. Finally we represent the domain allowed by the GW data with the "+" (TD-LVC-2018), "x" (TD-De-2018) and "$\star$" (TD-Coughlin-2019) symbols. There is a nice overlap between the GW data and the ISGMR. Furthermore, the confrontation of the GW data to the ISGMR correlation band allows to identify a smaller domain in $K_{\rm sat} - Q_{\rm sat}$, which is represented by the blue 1σ ellipse. However there is a discrepancy between the correlations from Skyrme and Gogny EDFs from Ref [KM13] and the GW, since the GW favors $-500 \leq Q_{\rm sat} \leq 1500$ MeV

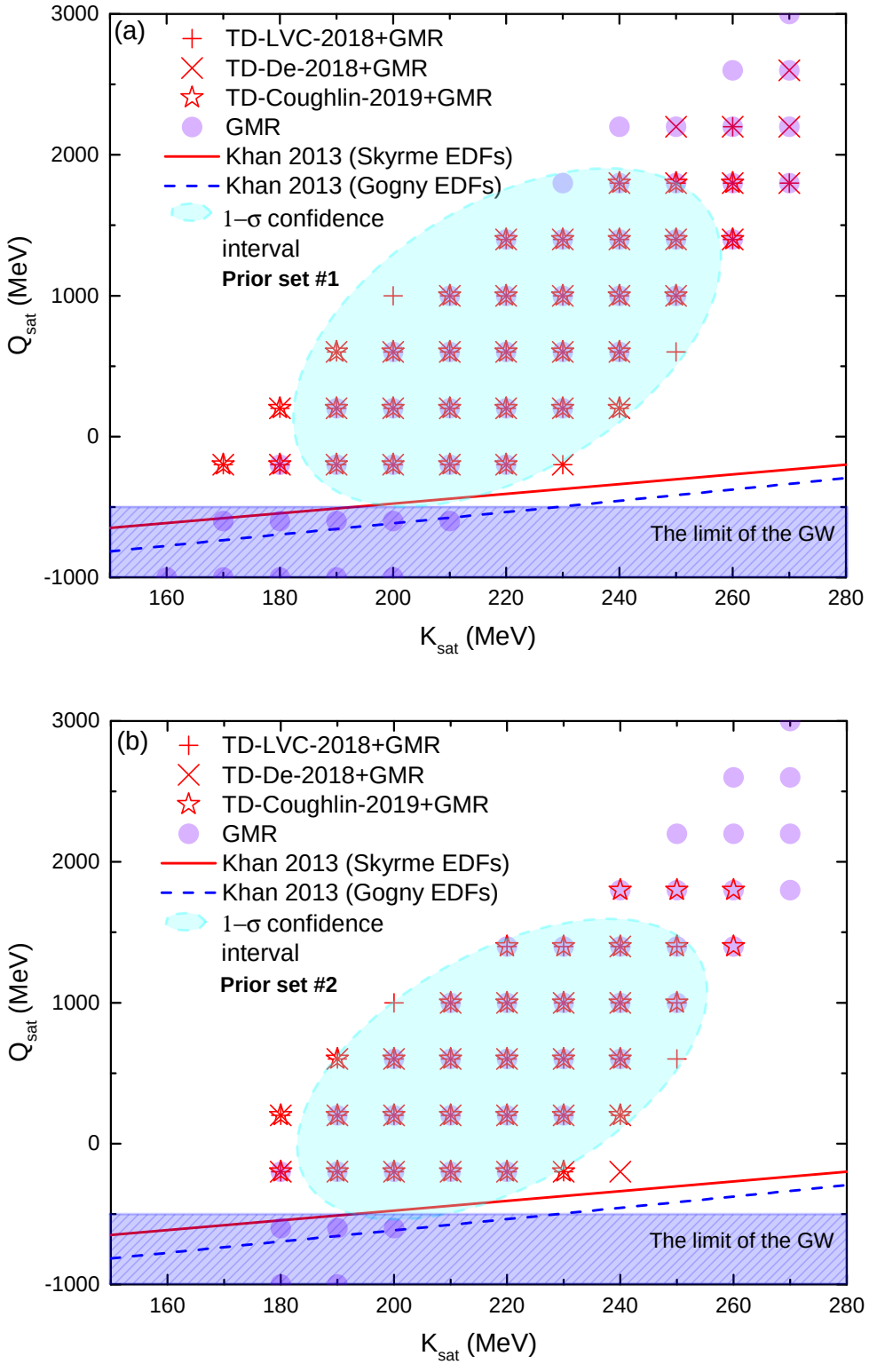

Fig. 4.9: The values of the $K_{\rm sat}$ and $Q_{\rm sat}$ inside of the 1-σ probability for the prior set #1 (a) and #2 (b) with a spurious correlation found for Skyrme and Gogny EDFs from Ref [KM13]. Note that the χEFT constraint is included for all joint posteriors.

and it forbids $Q_{\rm sat} \leq -500$ MeV. The difference of this divergence can also be a hint for a phase transition.

From the 1σ confidence interval one can derive the following relation:

$$K_{\rm sat} = \alpha_2 Q_{\rm sat} + \beta_2, \tag{4.4}$$

where $\alpha_2 = 0.035^{+0.010}_{-0.010}$ and $\beta_2 = 199^{+20}_{-30}$. Furthermore, it seems that the ISGMR effectively constrains $K_{\rm sat}$ while GW limits the lower value of $Q_{\rm sat}$. Consequently, joint posteriors predict $170/180 \leq K_{\rm sat} \leq 250/240$ MeV and $-500/-500 \leq Q_{\rm sat} \leq 1200/1000$ MeV for the prior set #1/#2, respectively. An increased resolution of both constraints shall lead to more accurate determination of $K_{\rm sat}$ and $Q_{\rm sat}$.

4.5. Concluding Remarks

In the present chapter, the main result is a marked tension between nuclear physics constraints (χEFT and ISGMR) and the astrophysical constraints from GW170817 and M^{obs}_{max}, assuming the PDF from Refs. [AAA+19, DFL+18]. The posteriors of GW for these two PDF favors $-4 \leq L_{\rm sym} \leq 27$ MeV and $218 \leq K_{\rm sym} \leq 648$ MeV while posteriors of χEFT predicts $25 \leq L_{\rm sym} \leq 49$ MeV and $-265 \leq K_{\rm sym} \leq 608$ MeV. Consequently, the neutron star properties, $R_{1.4}$ and $P(2n_{\rm sat})$, also exhibit intriguing tensions between these two constraints: the $p_{\tilde{\Lambda}}$ suggests smaller radii at $1.4M_\odot$ and higher pressure at $2n_{sat}$ at variance with nuclear physics. Since $K_{\rm sym}$ is responsible for the pressure at high density, but not for the radius at $1.4M_\odot$, this effect can be understood as a consequence of the low $L_{\rm sym}-$ high $K_{\rm sym}$ case. However the models of nuclear physics predict high $L_{\rm sym}-$ low $K_{\rm sym}$, in an opposite way. This tension may be a hint for a quark phase transition which would lower the radius of NS with masses larger than about $1.3M_\odot$, i.e. densities larger than about $2n_{sat}$. This conclusion should however be contrasted with the results obtained from a third analysis exploiting the multi-messenger signals from GW170817 (GW, EM and GRB), which favors a larger value of tidal deformability ($\tilde{\Lambda} \approx 600$). In this case, the tension with nuclear physics on radii is solved and typical radii $R_{1.4} \approx 12.5 - 13$ km are obtained. However, noticeable differences on nuclear empirical parameters

are still exist. The reason that the GW constrain the radius better than the nuclear empirical parameters where the nuclear empirical parameters include more uncertainties on the high density regime of NS EoS could lead to noticeable differences of PDFs. Note that the multi-messenger analysis is based on the present state-of-the-art numerical simulations as well as on the single GW170817 event. Future improvements of the simulations as well as more binary neutron star events will potentially influence the result of the present Bayesian analysis. This illustrates the complexity of the multi-messenger analysis, which can be contrasted with the GW waveform analysis which is almost only based on general relativity theory and the assumption of low spin of the NS.

The second main result is that we could extract boundaries for a set of nuclear empirical parameters from the joint probability from TD-LVC-2018:

(1) $L_{\rm sym} = 0.00^{+12.00}_{-4.00}/16.58^{+11.28}_{-6.79}$ MeV,

(2) $K_{\rm sym} = 438.57^{+210.12}_{-210.12}$ MeV (see related discussion for the prior set #2),

(3) $Q_{\rm sat} = -180^{+1222}_{-175}/-162^{+935}_{-175}$ MeV,

(4) $Q_{\rm sym} = -270^{+1690}_{-1126}/-169^{+1376}_{-748}$ MeV,

for the prior set #1/#2, respectively. It is also concluded that $Q_{\rm sat}$ is constrained by both GW and ISGMR analyses.

With the use of these nuclear parameters, we obtained the following values for the NS properties:

(5) $R_{1.4} = 11.00^{+1.30}_{-0.25}/10.98^{+1.90}_{-0.25}$ or $R_{1.4} = 12.00^{+0.30}_{-1.25}/10.98^{+1.90}_{-0.25}$ km and

(6) $P(2n_{\rm sat}) = 24.61^{+24.42}_{-5.00}/26.02^{+13.58}_{-5.00}$ MeV fm^{-3}

for prior set #1/#2, respectively. It should be noted that these last results are in a good agreement with other recent analyses using GW [AAA+18, LH18, MAD+19].

Finally we have analyzed the $L_{\rm sym}$-$K_{\rm sym}$ and $K_{\rm sat}$-$Q_{\rm sat}$ correlations under the influence of GW170817, χEFT and ISGMR constraints and proposed fits

for our joint probability correlations. A different relation from nuclear physics is found: $K_{\rm sym} = \alpha_1 L_{\rm sym} + \beta_1$ where $\alpha_1 = -18.83^{+3.00}_{-2.00}$ and $\beta_1 = 616^{+140}_{-180}$ MeV. Another correlation which we found is the $K_{\rm sat} - Q_{\rm sat}$ one. As one expects, this relation is highly correlated with the ISGMR [KMV12, KM13]. However we showed that GW has also a decisive role in determining these parameters since it constrains $Q_{\rm sat}$. Consequently, we found the following relation: $K_{\rm sat} = \alpha_2 Q_{\rm sat} + \beta_2$ where $\alpha_2 = 0.035^{+0.010}_{-0.010}$ and $\beta_2 = 199^{+20}_{-30}$. All things considered, increasing the accuracy on the determination of tidal deformability from GW, as well as M_c from the ISGMR, will lead to a better determination of $K_{\rm sat}$ and $Q_{\rm sat}$.

Conclusions and Outlook

In the present thesis, we have investigated the nuclear equation of state (EoS), impacting the structure of neutron stars (NS). On this purpose, we first discussed Λ hyperons in the nuclear structure which is related to the phase transition to hypernuclear matter and we investigate the traditional nuclear matter approach with observational constraints.

Hypernuclear matter for NSs is problematic since hypernuclear equation of states decrease the pressure inside the NS core [CS13, ZH13, MKV15, CV16, FAPVn17, GCS19] leading to smaller maximum mass than the observational maximum mass for NS ($2M_{\odot}$ [AFW^{+}13, ABBS^{+}18]). One of the solution to this "puzzle" could be better understanding of the hyperon interaction inside the nuclear medium, which can be extracted from experiments on multi-strange hypernuclei. Although current experiments are limited to measure up to a few double-Λ hypernuclei, we hope that future experiments will produce enough number of multi-strange hypernuclei to extend our knowledge about to this problem. In this case superfluidity (or pairing) in hypernuclei could impact the interpretation of the experiments. Therefore, the Λ pairing channel was studied for multi-strange hypernuclei in the first part of the thesis. For this purpose, we considered Hartree-Fock-Bogoliubov (or Bogoliubov-de Gennes) formalism [DFT84, BD05] to evaluate ground state properties of ${}^{40}_{-S\Lambda}$Ca, ${}^{132}_{-S\Lambda}$Sn and ${}^{208}_{-S\Lambda}$Pb hypernuclei which have closed proton and neutron shells, since the semi-magicity often guarantees that nuclei remain at, or close to, sphericity. We first investigated the possibility of NΛ (N=proton or neutron) pairing channel by comparing the Fermi energies of

each nucleons and Λ by using the Hartree-Fock approach. Since the energy difference between nucleons and Λ Fermi levels is usually large (more than 5 MeV) in the considered nuclei, the NΛ pairing is quenched in most of the cases. We then fit a ΛΛ pairing interaction into the Hartree-Fock-Bogoliubov equations, where the magnitude of ΛΛ pairing is calibrated to be consistent with the maximum predictions for the Λ pairing gap in hypernuclear matter [TMC03]. Generally, we found that ΛΛ pairing could be active if the energy gap between orbitals is smaller than 3 MeV. Under this condition, Λ pairing could impact densities and binding energies. Since only a weak spin-orbit interaction is expected in the Λ channel, Λ states are highly degenerated and usually distant by more than 3 MeV in energy. Therefore, Λ-related pairing effects can usually be neglected in most of hypernuclei, except for hypernuclei which have a single particle gap lower than 3 MeV around the Fermi level.

With the advent of a first gravitational wave detection from a binary NS merger (GW170817) [AAA+17, AAA+18], a new era for nuclear astrophysics has begun, since it has provided an additional observable related to the EoS of NS: Tidal deformability ($\tilde{\Lambda}$) [Hin08, FH08, DN09]. It has also opened a possibility to test different EoSs for NSs. Taking advantage of GW constraints on tidal deformability, we tested the validity of the traditional nuclear matter hypothesis in the second part of the thesis. On this purpose, nuclear EoSs were generated by using observational data such as the maximum mass ($2M_{\odot}$ see Refs. [AFW+13, ABBS+18] for details) and $\tilde{\Lambda}$ constrained from the gravitational wave event of GW170817 [AAA+17, DFL+18, AAA+19, CDMM19], as well as predictions from nuclear physics such as Chiral Effective Field Theory (χEFT) [DHS16] and Isoscalar Giant Monopole Resonance (ISGMR) [KMV12, KM13]. Our main results are the presence of noticeable tensions between various analyses of the GW signal from GW170817, depending on the inclusion or absence of multi-messenger additional constraints, and also noticeable tensions between astrophysical and nuclear physics constraints. For instance, the posteriors using the Ref. [DFL+18] (TD-De-2018) favors $L_{\rm sym} = 0^{+2}_{-3}$ MeV, $K_{\rm sym} = 390^{+1110}_{-400}$ MeV, while Ref. [CDMM19] (TD-Coughlin-2019) favours, $L_{\rm sym} = 17^{+15}_{-15}$ MeV, $K_{\rm sym} = 275^{+890}_{-330}$ MeV. The posterior predictions using $\tilde{\Lambda}$ from Ref. [AAA+19] (TD-LVC-2018) are intermediate between these two cases. This tension also exists for the radius predictions $R_{1.4}$, since $R_{1.4} = 10.7^{+2.1}_{-0.3}$ km in the case of TD-De-2018 and TD-LVC-2018,

while it is $R_{1.4} = 13.1^{+0.5}_{-0.5}$ km in the case of TD-Coughlin-2019. These probability density functions (PDFs) of $\tilde{\Lambda}$ are however more consistent in their predictions for the pressure and we have found $P(2n_{\rm sat}) = 45^{+35}_{-25}$ MeV fm^{-3} for prior set #1 (see Sec. 3.8 for details). Besides, these predictions are also in noticeable tension with the posteriors obtained from χEFT which predict $L_{\rm sym} = 35^{+7}_{-10}$ MeV, $K_{\rm sym} = 14^{+600}_{-265}$ MeV, $R_{1.4} = 13.0^{+0.8}_{-1.2}$ km and $P(2n_{\rm sat}) = 12^{+23}_{-4}$ MeV fm^{-3} for prior set #1. It is interesting to note that there is a marked tension in the values for $L_{\rm sym}$ between all $\tilde{\Lambda}$-PDF analyses and the χEFT one. However, it should be noted that for the radius $R_{1.4}$ the multi-messenger $\tilde{\Lambda}$-PDF from Ref. [CDMM19], which is peaked at $\tilde{\Lambda} \approx 600$ is in good agreement with χEFT predictions.

The tensions presented here between the posterior predictions are important, but still consistent at 2-3σ. The reduction of the uncertainties in our predictions requires a reduction of the observational or experimental uncertainties. Hence increasing the accuracy on the determination of tidal deformability from gravitational wave, as well as M_c from the ISGMR, will lead to a better determination of $K_{\rm sat}$ and $Q_{\rm sat}$ and NS properties. Increasing the number of gravitational wave signals of binary NS merger is also a way to refine our present analysis and conclude on the strength of the tension between multi-physics constraints. Ultimately including hyperon degree of freedom in the GW constrained EoS, shall allow to bridge the two main parts of the present work in a unified form.

Résumé en Français

Dans cette thése nous avons d'abord étudié l'effet du paring Lambda sur les propriétés des hypernoyaux dans le formalisme Hartree-Fock Bogoliubov. La fonctionnelle de Skyrme SLy5 est utilisée dans le canal nucleon-nucleon alors que 3 fonctionelles fittées sur les calculs microscopiques Brueckner Hartree-Fock sont utilisées dans le canal NΛ: DF-NSC89, DF-NSC97a et DF-NSC97f. Ces fonctionelles décrivent la séquence des énergies de liaison expérimentales à un Λ, des hypernoyaux légers aux hypernoyaux lourds. Dans le cas du canal ΛΛ, nous avons utilisé la prescription empirique EmpC, ajustée à 1 MeV sur l'énergie expérimentale de liaison dans le $^{6}\mathrm{He}_{\Lambda\Lambda}$. A l'aide de cette approche de la fonctionelle de la densité, plusieurs noyaux ont été étudiés, avec des couches nucléoniques fermées et des couches ouvertes en Λ. Une interaction d'appariement Lambda-Lambda est introduite, dont la magnitude est ajustée pour être consistante avec la valeur maximale des prédictions BCS pour le gap d'appariement Λ dans la matière hyperonique. Nous donnons ainsi une valeur maximale pour la prédiction du gap d'appariement Λ et ses effets dans les hypernoyaux. Nous avons montré que les effets de l'appariement ΛΛ dependent de l'hypernoyau considéré. L'énergie correspondante de condensation est de l'ordre de 3 MeV au maximum, ce qui entraine de faibles corrections sur les distributions de densité et la structure en couches. De manière générale, nous avons trouvé que l'appariement ΛΛ peut être important si l'écart en énergie entre les couches est plus petit que 3 MeV. A cette condition, l'appariement Lambda peut impacter les densité et les énergies de liaison. En résumé, il est montré que l'effet de l'appariement relié aux Λ peut être en général négligé dans la plupart des hypernoyaux, sauf pour les ceux

ayant un écart typique dans le spectre à une particule plus petit que 3 MeV autour du niveau de Fermi. De plus, les conditions sur à la fois les énergies de Fermi et les moments angulaire orbitaux atténuent l'appariement nucleon-Λ pour la plupart des hypernoyaux. La deuxième partie de la thèse est dévolue aux équations d'état dans les étoiles à neutrons. Nous avons confronté les valeurs des déformabilités de marée extraites de l'évènement d'onde gravitationnelle GW170817, aux contraintes issues de la physique nucléaire à l'aide d'une approche semi-agnostique pour l'équation d'état de la matière dense. Nous avons utilisé les statistiques Bayesienne pour combiner les données de physique nucléaire à basse densité, comme les prédictions ab initio provenant des interactions chirales EFT ou la resonance géante monopolaire isoscalaire, et les contraintes astrophysiques sur les étoiles à neutrons, comme leur masse maximale, ou la fonction densité de probabilité de la déformabilité de marée obtenue de l'événement GW170817. Les fonctions postérieures de densité de probabilité sont marginalisées sur plusieurs paramètres nucléaires empiriques ($L_{\rm sym}$, $K_{\rm sym}$, $Q_{\rm sat}$ et $Q_{\rm sym}$), et aussi sur des grandeurs observationnelles des étoiles à neutrons comme la masse et le rayon à 1.4 masses solaires, ou la pression à deux fois la densité de saturation $P(2n_{\rm sat})$. Les correlations entre $L_{\rm sym}$ et $K_{\rm sym}$, et entre $K_{\rm sat}$ et $Q_{\rm sat}$ sont aussi analysées. Une tension importante entre les données observationnelles d'ondes gravitationnelles et les inputs de physique nucléaire est trouvée pour les distributions marginales de probabilité de Lsym et $R_{1.4}$. Ceci pourrait être une indication d'une transition de phase de nucléons vers des particules plus exotiques dans le coeur des étoiles à neutrons. Nous trouvons aussi qu'augmenter la précision sur la détermination de la déformabilité de marée à partir des ondes gravitationnelles, ou sur M_c à partir de la résonance géantes monopolaire, devrait aboutir à une meilleure determination de $K_{\rm sat}$ et $Q_{\rm sat}$. Les résultats obtenus ouvrent la perspective de mieux contraindre les paramètres empiriques de l'équation d'état nucléaire. En particulier, la valeur de Lsym contrainte par les observations d'ondes gravitationnelles, diffère significativement de celle provenant des contrainte nucléaire. Une étude de l'impact d'une éventuelle phase de quark dans les étoiles à neutrons est suggérée, afin de lever cette tension.

Bibliography

[AAA+12] S. Abrahamyan, Z. Ahmed, H. Albataineh, K. Aniol, D. S. Armstrong, W. Armstrong, T. Averett, B. Babineau, A. Barbieri, V. Bellini, R. Beminiwattha, J. Benesch, F. Benmokhtar, T. Bielarski, W. Boeglin, A. Camsonne, M. Canan, P. Carter, G. D. Cates, C. Chen, J.-P. Chen, O. Hen, F. Cusanno, M. M. Dalton, R. De Leo, K. de Jager, W. Deconinck, P. Decowski, X. Deng, A. Deur, D. Dutta, A. Etile, D. Flay, G. B. Franklin, M. Friend, S. Frullani, E. Fuchey, F. Garibaldi, E. Gasser, R. Gilman, A. Giusa, A. Glamazdin, J. Gomez, J. Grames, C. Gu, O. Hansen, J. Hansknecht, D. W. Higinbotham, R. S. Holmes, T. Holmstrom, C. J. Horowitz, J. Hoskins, J. Huang, C. E. Hyde, F. Itard, C.-M. Jen, E. Jensen, G. Jin, S. Johnston, A. Kelleher, K. Kliakhandler, P. M. King, S. Kowalski, K. S. Kumar, J. Leacock, J. Leckey, J. H. Lee, J. J. LeRose, R. Lindgren, N. Liyanage, N. Lubinsky, J. Mammei, F. Mammoliti, D. J. Margaziotis, P. Markowitz, A. McCreary, D. McNulty, L. Mercado, Z.-E. Meziani, R. W. Michaels, M. Mihovilovic, N. Muangma, C. Muñoz Camacho, S. Nanda, V. Nelyubin, N. Nuruzzaman, Y. Oh, A. Palmer, D. Parno, K. D. Paschke, S. K. Phillips, B. Poelker, R. Pomatsalyuk, M. Posik, A. J. R. Puckett, B. Quinn, A. Rakhman, P. E. Reimer, S. Riordan, P. Rogan, G. Ron, G. Russo, K. Saenboonruang, A. Saha, B. Sawatzky, A. Shahinyan, R. Silwal, S. Sirca, K. Slifer, P. Solvignon, P. A. Souder, M. L. Sperduto, R. Subedi, R. Suleiman, V. Sulkosky, C. M. Sutera, W. A. To-

bias, W. Troth, G. M. Urciuoli, B. Waidyawansa, D. Wang, J. Wexler, R. Wilson, B. Wojtsekhowski, X. Yan, H. Yao, Y. Ye, Z. Ye, V. Yim, L. Zana, X. Zhan, J. Zhang, Y. Zhang, X. Zheng, and P. Zhu. Measurement of the Neutron Radius of ^{208}Pb through Parity Violation in Electron Scattering. *Physical Review Letters*, 108:112502, 2012.

[AAA+13] J. K. Ahn, H. Akikawa, S. Aoki, K. Arai, S. Y. Bahk, K. M. Baik, B. Bassalleck, J. H. Chung, M. S. Chung, D. H. Davis, T. Fukuda, K. Hoshino, A. Ichikawa, M. Ieiri, K. Imai, K. Itonaga, Y. H. Iwata, Y. S. Iwata, H. Kanda, M. Kaneko, T. Kawai, M. Kawasaki, C. O. Kim, J. Y. Kim, S. H. Kim, S. J. Kim, Y. Kondo, T. Kouketsu, H. N. Kyaw, Y. L. Lee, J. W. C. McNabb, A. A. Min, M. Mitsuhara, K. Miwa, K. Nakazawa, Y. Nagase, C. Nagoshi, Y. Nakanishi, H. Noumi, S. Ogawa, H. Okabe, K. Oyama, B. D. Park, H. M. Park, I. G. Park, J. Parker, Y. S. Ra, J. T. Rhee, A. Rusek, A. Sawa, H. Shibuya, K. S. Sim, P. K. Saha, D. Seki, M. Sekimoto, J. S. Song, H. Takahashi, T. Takahashi, F. Takeutchi, H. Tanaka, K. Tanida, K. T. Tint, J. Tojo, H. Torii, S. Torikai, D. N. Tovee, T. Tsunemi, M. Ukai, N. Ushida, T. Wint, K. Yamamoto, N. Yasuda, J. T. Yang, C. J. Yoon, C. S. Yoon, M. Yosoi, T. Yoshida, and L. Zhu. Double-Λ hypernuclei observed in a hybrid emulsion experiment. *Physical Review C*, 88(1), July 2013.

[AAA+17] Benjamin P Abbott, Rich Abbott, TD Abbott, Fausto Acernese, Kendall Ackley, Carl Adams, Thomas Adams, Paolo Addesso, RX Adhikari, VB Adya, et al. Gw170817: observation of gravitational waves from a binary neutron star inspiral. *Physical Review Letters*, 119(16):161101, 2017.

[AAA+18] B. P. Abbott, R. Abbott, T. D. Abbott, F. Acernese, K. Ackley, C. Adams, T. Adams, P. Addesso, R. X. Adhikari, V. B. Adya, C. Affeldt, B. Agarwal, M. Agathos, K. Agatsuma, N. Aggarwal, O. D. Aguiar, L. Aiello, A. Ain, P. Ajith, B. Allen, G. Allen, A. Allocca, M. A. Aloy, P. A. Altin, A. Amato, A. Ananyeva, S. B. Anderson, W. G. Anderson, S. V. Angelova, S. Antier, S. Appert, K. Arai, M. C. Araya, J. S. Areeda,

M. Arène, N. Arnaud, K. G. Arun, S. Ascenzi, G. Ashton, M. Ast, S. M. Aston, P. Astone, D. V. Atallah, F. Aubin, P. Aufmuth, C. Aulbert, K. AultONeal, C. Austin, A. Avila-Alvarez, S. Babak, P. Bacon, F. Badaracco, M. K. M. Bader, S. Bae, P. T. Baker, F. Baldaccini, G. Ballardin, S. W. Ballmer, S. Banagiri, J. C. Barayoga, S. E. Barclay, B. C. Barish, D. Barker, K. Barkett, S. Barnum, F. Barone, B. Barr, L. Barsotti, M. Barsuglia, D. Barta, J. Bartlett, I. Bartos, R. Bassiri, A. Basti, J. C. Batch, M. Bawaj, J. C. Bayley, M. Bazzan, B. Bécsy, C. Beer, M. Bejger, I. Belahcene, A. S. Bell, D. Beniwal, M. Bensch, B. K. Berger, G. Bergmann, S. Bernuzzi, J. J. Bero, C. P. L. Berry, D. Bersanetti, A. Bertolini, J. Betzwieser, R. Bhandare, I. A. Bilenko, S. A. Bilgili, G. Billingsley, C. R. Billman, J. Birch, R. Birney, O. Birnholtz, S. Biscans, S. Biscoveanu, A. Bisht, M. Bitossi, M. A. Bizouard, J. K. Blackburn, J. Blackman, C. D. Blair, D. G. Blair, R. M. Blair, S. Bloemen, O. Bock, N. Bode, M. Boer, Y. Boetzel, G. Bogaert, A. Bohe, F. Bondu, E. Bonilla, R. Bonnand, P. Booker, B. A. Boom, C. D. Booth, R. Bork, V. Boschi, S. Bose, K. Bossie, V. Bossilkov, J. Bosveld, Y. Bouffanais, A. Bozzi, C. Bradaschia, P. R. Brady, A. Bramley, M. Branchesi, J. E. Brau, T. Briant, F. Brighenti, A. Brillet, M. Brinkmann, V. Brisson, P. Brockill, A. F. Brooks, D. D. Brown, S. Brunett, C. C. Buchanan, A. Buikema, T. Bulik, H. J. Bulten, A. Buonanno, D. Buskulic, C. Buy, R. L. Byer, M. Cabero, L. Cadonati, G. Cagnoli, C. Cahillane, J. Calderón Bustillo, T. A. Callister, E. Calloni, J. B. Camp, M. Canepa, P. Canizares, K. C. Cannon, H. Cao, J. Cao, C. D. Capano, E. Capocasa, F. Carbognani, S. Caride, M. F. Carney, G. Carullo, J. Casanueva Diaz, C. Casentini, S. Caudill, M. Cavaglià, F. Cavalier, R. Cavalieri, G. Cella, C. B. Cepeda, P. Cerdá-Durán, G. Cerretani, E. Cesarini, O. Chaibi, S. J. Chamberlin, M. Chan, S. Chao, P. Charlton, E. Chase, E. Chassande-Mottin, D. Chatterjee, K. Chatziioannou, B. D. Cheeseboro, H. Y. Chen, X. Chen, Y. Chen, H.-P. Cheng, H. Y. Chia, A. Chincarini, A. Chiummo, T. Chmiel, H. S. Cho, M. Cho, J. H. Chow, N. Christensen, Q. Chu, A. J. K. Chua, S. Chua,

K. W. Chung, S. Chung, G. Ciani, A. A. Ciobanu, R. Ciolfi, F. Cipriano, C. E. Cirelli, A. Cirone, F. Clara, J. A. Clark, P. Clearwater, F. Cleva, C. Cocchieri, E. Coccia, P.-F. Cohadon, D. Cohen, A. Colla, C. G. Collette, C. Collins, L. R. Cominsky, M. Constancio, L. Conti, S. J. Cooper, P. Corban, T. R. Corbitt, I. Cordero-Carrión, K. R. Corley, N. Cornish, A. Corsi, S. Cortese, C. A. Costa, R. Cotesta, M. W. Coughlin, S. B. Coughlin, J.-P. Coulon, S. T. Countryman, P. Couvares, P. B. Covas, E. E. Cowan, D. M. Coward, M. J. Cowart, D. C. Coyne, R. Coyne, J. D. E. Creighton, T. D. Creighton, J. Cripe, S. G. Crowder, T. J. Cullen, A. Cumming, L. Cunningham, E. Cuoco, T. Dal Canton, G. Dálya, S. L. Danilishin, S. D'Antonio, K. Danzmann, A. Dasgupta, C. F. Da Silva Costa, V. Dattilo, I. Dave, M. Davier, D. Davis, E. J. Daw, B. Day, D. DeBra, M. Deenadayalan, J. Degallaix, M. De Laurentis, S. Deléglise, W. Del Pozzo, N. Demos, T. Denker, T. Dent, R. De Pietri, J. Derby, V. Dergachev, R. De Rosa, C. De Rossi, R. DeSalvo, O. de Varona, S. Dhurandhar, M. C. Díaz, T. Dietrich, L. Di Fiore, M. Di Giovanni, T. Di Girolamo, A. Di Lieto, B. Ding, S. Di Pace, I. Di Palma, F. Di Renzo, A. Dmitriev, Z. Doctor, V. Dolique, F. Donovan, K. L. Dooley, S. Doravari, I. Dorrington, M. Dovale Álvarez, T. P. Downes, M. Drago, C. Dreissigacker, J. C. Driggers, Z. Du, P. Dupej, S. E. Dwyer, P. J. Easter, T. B. Edo, M. C. Edwards, A. Effler, H.-B. Eggenstein, P. Ehrens, J. Eichholz, S. S. Eikenberry, M. Eisenmann, R. A. Eisenstein, R. C. Essick, H. Estelles, D. Estevez, Z. B. Etienne, T. Etzel, M. Evans, T. M. Evans, V. Fafone, H. Fair, S. Fairhurst, X. Fan, S. Farinon, B. Farr, W. M. Farr, E. J. Fauchon-Jones, M. Favata, M. Fays, C. Fee, H. Fehrmann, J. Feicht, M. M. Fejer, F. Feng, A. Fernandez-Galiana, I. Ferrante, E. C. Ferreira, F. Ferrini, F. Fidecaro, I. Fiori, D. Fiorucci, M. Fishbach, R. P. Fisher, J. M. Fishner, M. Fitz-Axen, R. Flaminio, M. Fletcher, H. Fong, J. A. Font, P. W. F. Forsyth, S. S. Forsyth, J.-D. Fournier, S. Frasca, F. Frasconi, Z. Frei, A. Freise, R. Frey, V. Frey, P. Fritschel, V. V. Frolov, P. Fulda, M. Fyffe, H. A. Gabbard, B. U. Gadre, S. M. Gaebel, J. R. Gair, L. Gam-

maitoni, M. R. Ganija, S. G. Gaonkar, A. Garcia, C. García-Quirós, F. Garufi, B. Gateley, S. Gaudio, G. Gaur, V. Gayathri, G. Gemme, E. Genin, A. Gennai, D. George, J. George, L. Gergely, V. Germain, S. Ghonge, Abhirup Ghosh, Archisman Ghosh, S. Ghosh, B. Giacomazzo, J. A. Giaime, K. D. Giardina, A. Giazotto, K. Gill, G. Giordano, L. Glover, E. Goetz, R. Goetz, B. Goncharov, G. González, J. M. Gonzalez Castro, A. Gopakumar, M. L. Gorodetsky, S. E. Gossan, M. Gosselin, R. Gouaty, A. Grado, C. Graef, M. Granata, A. Grant, S. Gras, C. Gray, G. Greco, A. C. Green, R. Green, E. M. Gretarsson, P. Groot, H. Grote, S. Grunewald, P. Gruning, G. M. Guidi, H. K. Gulati, X. Guo, A. Gupta, M. K. Gupta, K. E. Gushwa, E. K. Gustafson, R. Gustafson, O. Halim, B. R. Hall, E. D. Hall, E. Z. Hamilton, H. F. Hamilton, G. Hammond, M. Haney, M. M. Hanke, J. Hanks, C. Hanna, M. D. Hannam, O. A. Hannuksela, J. Hanson, T. Hardwick, J. Harms, G. M. Harry, I. W. Harry, M. J. Hart, C.-J. Haster, K. Haughian, J. Healy, A. Heidmann, M. C. Heintze, H. Heitmann, P. Hello, G. Hemming, M. Hendry, I. S. Heng, J. Hennig, A. W. Heptonstall, F. J. Hernandez, M. Heurs, S. Hild, T. Hinderer, W. C. G. Ho, D. Hoak, S. Hochheim, D. Hofman, N. A. Holland, K. Holt, D. E. Holz, P. Hopkins, C. Horst, J. Hough, E. A. Houston, E. J. Howell, A. Hreibi, E. A. Huerta, D. Huet, B. Hughey, M. Hulko, S. Husa, S. H. Huttner, T. Huynh-Dinh, A. Iess, N. Indik, C. Ingram, R. Inta, G. Intini, B. S. Irwin, H. N. Isa, J.-M. Isac, M. Isi, B. R. Iyer, K. Izumi, T. Jacqmin, K. Jani, P. Jaranowski, D. S. Johnson, W. W. Johnson, D. I. Jones, R. Jones, R. J. G. Jonker, L. Ju, J. Junker, C. V. Kalaghatgi, V. Kalogera, B. Kamai, S. Kandhasamy, G. Kang, J. B. Kanner, S. J. Kapadia, S. Karki, K. S. Karvinen, M. Kasprzack, M. Katolik, S. Katsanevas, E. Katsavounidis, W. Katzman, S. Kaufer, K. Kawabe, N. V. Keerthana, F. Kéfélian, D. Keitel, A. J. Kemball, R. Kennedy, J. S. Key, F. Y. Khalili, B. Khamesra, H. Khan, I. Khan, S. Khan, Z. Khan, E. A. Khazanov, N. Kijbunchoo, Chunglee Kim, J. C. Kim, K. Kim, W. Kim, W. S. Kim, Y.-M. Kim, E. J. King, P. J. King, M. Kinley-Hanlon,

R. Kirchhoff, J. S. Kissel, L. Kleybolte, S. Klimenko, T. D. Knowles, P. Koch, S. M. Koehlenbeck, S. Koley, V. Kondrashov, A. Kontos, M. Korobko, W. Z. Korth, I. Kowalska, D. B. Kozak, C. Krämer, V. Kringel, B. Krishnan, A. Królak, G. Kuehn, P. Kumar, R. Kumar, S. Kumar, L. Kuo, A. Kutynia, S. Kwang, B. D. Lackey, K. H. Lai, M. Landry, P. Landry, R. N. Lang, J. Lange, B. Lantz, R. K. Lanza, A. Lartaux-Vollard, P. D. Lasky, M. Laxen, A. Lazzarini, C. Lazzaro, P. Leaci, S. Leavey, C. H. Lee, H. K. Lee, H. M. Lee, H. W. Lee, K. Lee, J. Lehmann, A. Lenon, M. Leonardi, N. Leroy, N. Letendre, Y. Levin, J. Li, T. G. F. Li, X. Li, S. D. Linker, T. B. Littenberg, J. Liu, X. Liu, R. K. L. Lo, N. A. Lockerbie, L. T. London, A. Longo, M. Lorenzini, V. Loriette, M. Lormand, G. Losurdo, J. D. Lough, C. O. Lousto, G. Lovelace, H. Lück, D. Lumaca, A. P. Lundgren, R. Lynch, Y. Ma, R. Macas, S. Macfoy, B. Machenschalk, M. MacInnis, D. M. Macleod, I. Magaña Hernandez, F. Magaña Sandoval, L. Magaña Zertuche, R. M. Magee, E. Majorana, I. Maksimovic, N. Man, V. Mandic, V. Mangano, G. L. Mansell, M. Manske, M. Mantovani, F. Marchesoni, F. Marion, S. Márka, Z. Márka, C. Markakis, A. S. Markosyan, A. Markowitz, E. Maros, A. Marquina, F. Martelli, L. Martellini, I. W. Martin, R. M. Martin, D. V. Martynov, K. Mason, E. Massera, A. Masserot, T. J. Massinger, M. Masso-Reid, S. Mastrogiovanni, A. Matas, F. Matichard, L. Matone, N. Mavalvala, N. Mazumder, J. J. McCann, R. McCarthy, D. E. McClelland, S. McCormick, L. McCuller, S. C. McGuire, J. McIver, D. J. McManus, T. McRae, S. T. McWilliams, D. Meacher, G. D. Meadors, M. Mehmet, J. Meidam, E. Mejuto-Villa, A. Melatos, G. Mendell, D. Mendoza-Gandara, R. A. Mercer, L. Mereni, E. L. Merilh, M. Merzougui, S. Meshkov, C. Messenger, C. Messick, R. Metzdorff, P. M. Meyers, H. Miao, C. Michel, H. Middleton, E. E. Mikhailov, L. Milano, A. L. Miller, A. Miller, B. B. Miller, J. Miller, M. Millhouse, J. Mills, M. C. Milovich-Goff, O. Minazzoli, Y. Minenkov, J. Ming, C. Mishra, S. Mitra, V. P. Mitrofanov, G. Mitselmakher, R. Mittleman, D. Moffa, K. Mogushi, M. Mohan, S. R. P. Mohapatra, M. Montani,

C. J. Moore, D. Moraru, G. Moreno, S. Morisaki, B. Mours, C. M. Mow-Lowry, G. Mueller, A. W. Muir, Arunava Mukherjee, D. Mukherjee, S. Mukherjee, N. Mukund, A. Mullavey, J. Munch, E. A. Muñiz, M. Muratore, P. G. Murray, A. Nagar, K. Napier, I. Nardecchia, L. Naticchioni, R. K. Nayak, J. Neilson, G. Nelemans, T. J. N. Nelson, M. Nery, A. Neunzert, L. Nevin, J. M. Newport, K. Y. Ng, S. Ng, P. Nguyen, T. T. Nguyen, D. Nichols, A. B. Nielsen, S. Nissanke, A. Nitz, F. Nocera, D. Nolting, C. North, L. K. Nuttall, M. Obergaulinger, J. Oberling, B. D. O'Brien, G. D. O'Dea, G. H. Ogin, J. J. Oh, S. H. Oh, F. Ohme, H. Ohta, M. A. Okada, M. Oliver, P. Oppermann, Richard J. Oram, B. O'Reilly, R. Ormiston, L. F. Ortega, R. O'Shaughnessy, S. Ossokine, D. J. Ottaway, H. Overmier, B. J. Owen, A. E. Pace, G. Pagano, J. Page, M. A. Page, A. Pai, S. A. Pai, J. R. Palamos, O. Palashov, C. Palomba, A. Pal-Singh, Howard Pan, Huang-Wei Pan, B. Pang, P. T. H. Pang, C. Pankow, F. Pannarale, B. C. Pant, F. Paoletti, A. Paoli, M. A. Papa, A. Parida, W. Parker, D. Pascucci, A. Pasqualetti, R. Passaquieti, D. Passuello, M. Patil, B. Patricelli, B. L. Pearlstone, C. Pedersen, M. Pedraza, R. Pedurand, L. Pekowsky, A. Pele, S. Penn, A. Perego, C. J. Perez, A. Perreca, L. M. Perri, H. P. Pfeiffer, M. Phelps, K. S. Phukon, O. J. Piccinni, M. Pichot, F. Piergiovanni, V. Pierro, G. Pillant, L. Pinard, I. M. Pinto, M. Pirello, M. Pitkin, R. Poggiani, P. Popolizio, E. K. Porter, L. Possenti, A. Post, J. Powell, J. Prasad, J. W. W. Pratt, G. Pratten, V. Predoi, T. Prestegard, M. Principe, S. Privitera, G. A. Prodi, L. G. Prokhorov, O. Puncken, M. Punturo, P. Puppo, M. Pürrer, H. Qi, V. Quetschke, E. A. Quintero, R. Quitzow-James, F. J. Raab, D. S. Rabeling, H. Radkins, P. Raffai, S. Raja, C. Rajan, B. Rajbhandari, M. Rakhmanov, K. E. Ramirez, A. Ramos-Buades, Javed Rana, P. Rapagnani, V. Raymond, M. Razzano, J. Read, T. Regimbau, L. Rei, S. Reid, D. H. Reitze, W. Ren, F. Ricci, P. M. Ricker, G. M. Riemenschneider, K. Riles, M. Rizzo, N. A. Robertson, R. Robie, F. Robinet, T. Robson, A. Rocchi, L. Rolland, J. G. Rollins, V. J. Roma, R. Romano, C. L. Romel, J. H. Romie,

D. Rosińska, M. P. Ross, S. Rowan, A. Rüdiger, P. Ruggi, G. Rutins, K. Ryan, S. Sachdev, T. Sadecki, M. Sakellariadou, L. Salconi, M. Saleem, F. Salemi, A. Samajdar, L. Sammut, L. M. Sampson, E. J. Sanchez, L. E. Sanchez, N. Sanchis-Gual, V. Sandberg, J. R. Sanders, N. Sarin, B. Sassolas, B. S. Sathyaprakash, P. R. Saulson, O. Sauter, R. L. Savage, A. Sawadsky, P. Schale, M. Scheel, J. Scheuer, P. Schmidt, R. Schnabel, R. M. S. Schofield, A. Schönbeck, E. Schreiber, D. Schuette, B. W. Schulte, B. F. Schutz, S. G. Schwalbe, J. Scott, S. M. Scott, E. Seidel, D. Sellers, A. S. Sengupta, D. Sentenac, V. Sequino, A. Sergeev, Y. Setyawati, D. A. Shaddock, T. J. Shaffer, A. A. Shah, M. S. Shahriar, M. B. Shaner, L. Shao, B. Shapiro, P. Shawhan, H. Shen, D. H. Shoemaker, D. M. Shoemaker, K. Siellez, X. Siemens, M. Sieniawska, D. Sigg, A. D. Silva, L. P. Singer, A. Singh, A. Singhal, A. M. Sintes, B. J. J. Slagmolen, T. J. Slaven-Blair, B. Smith, J. R. Smith, R. J. E. Smith, S. Somala, E. J. Son, B. Sorazu, F. Sorrentino, T. Souradeep, A. P. Spencer, A. K. Srivastava, K. Staats, M. Steinke, J. Steinlechner, S. Steinlechner, D. Steinmeyer, B. Steltner, S. P. Stevenson, D. Stocks, R. Stone, D. J. Stops, K. A. Strain, G. Stratta, S. E. Strigin, A. Strunk, R. Sturani, A. L. Stuver, T. Z. Summerscales, L. Sun, S. Sunil, J. Suresh, P. J. Sutton, B. L. Swinkels, M. J. Szczepańczyk, M. Tacca, S. C. Tait, C. Talbot, D. Talukder, D. B. Tanner, M. Tápai, A. Taracchini, J. D. Tasson, J. A. Taylor, R. Taylor, S. V. Tewari, T. Theeg, F. Thies, E. G. Thomas, M. Thomas, P. Thomas, K. A. Thorne, E. Thrane, S. Tiwari, V. Tiwari, K. V. Tokmakov, K. Toland, M. Tonelli, Z. Tornasi, A. Torres-Forné, C. I. Torrie, D. Töyrä, F. Travasso, G. Traylor, J. Trinastic, M. C. Tringali, A. Trovato, L. Trozzo, K. W. Tsang, M. Tse, R. Tso, D. Tsuna, L. Tsukada, D. Tuyenbayev, K. Ueno, D. Ugolini, A. L. Urban, S. A. Usman, H. Vahlbruch, G. Vajente, G. Valdes, N. van Bakel, M. van Beuzekom, J. F. J. van den Brand, C. Van Den Broeck, D. C. Vander-Hyde, L. van der Schaaf, J. V. van Heijningen, A. A. van Veggel, M. Vardaro, V. Varma, S. Vass, M. Vasúth, A. Vecchio, G. Vedovato, J. Veitch, P. J. Veitch, K. Venkateswara,

G. Venugopalan, D. Verkindt, F. Vetrano, A. Viceré, A. D. Viets, S. Vinciguerra, D. J. Vine, J.-Y. Vinet, S. Vitale, T. Vo, H. Vocca, C. Vorvick, S. P. Vyatchanin, A. R. Wade, L. E. Wade, M. Wade, R. Walet, M. Walker, L. Wallace, S. Walsh, G. Wang, H. Wang, J. Z. Wang, W. H. Wang, Y. F. Wang, R. L. Ward, J. Warner, M. Was, J. Watchi, B. Weaver, L.-W. Wei, M. Weinert, A. J. Weinstein, R. Weiss, F. Wellmann, L. Wen, E. K. Wessel, P. Weßels, J. Westerweck, K. Wette, J. T. Whelan, B. F. Whiting, C. Whittle, D. Wilken, D. Williams, R. D. Williams, A. R. Williamson, J. L. Willis, B. Willke, M. H. Wimmer, W. Winkler, C. C. Wipf, H. Wittel, G. Woan, J. Woehler, J. K. Wofford, W. K. Wong, J. Worden, J. L. Wright, D. S. Wu, D. M. Wysocki, S. Xiao, W. Yam, H. Yamamoto, C. C. Yancey, L. Yang, M. J. Yap, M. Yazback, Hang Yu, Haocun Yu, M. Yvert, A. Zadrożny, M. Zanolin, T. Zelenova, J.-P. Zendri, M. Zevin, J. Zhang, L. Zhang, M. Zhang, T. Zhang, Y.-H. Zhang, C. Zhao, M. Zhou, Z. Zhou, S. J. Zhu, X. J. Zhu, A. B. Zimmerman, Y. Zlochower, M. E. Zucker, and J. Zweizig. GW170817: Measurements of Neutron Star Radii and Equation of State. *Physical Review Letters*, 121:161101, 2018.

[AAA+19] BP Abbott, R Abbott, TD Abbott, F Acernese, K Ackley, C Adams, T Adams, P Addesso, RX Adhikari, VB Adya, et al. Properties of the binary neutron star merger gw170817. *Physical Review X*, 9(1):011001, 2019.

[ABBS+18] Z. Arzoumanian, A. Brazier, S. Burke-Spolaor, S. Chamberlin, S. Chatterjee, B. Christy, J. M. Cordes, N. J. Cornish, F. Crawford, H. T. Cromartie, K. Crowter, M. E. DeCesar, P. B. Demorest, T. Dolch, J. A. Ellis, R. D. Ferdman, E. C. Ferrara, E. Fonseca, N. Garver-Daniels, P. A. Gentile, D. Halmrast, E. A. Huerta, F. A. Jenet, C. Jessup, G. Jones, M. L. Jones, D. L. Kaplan, M. T. Lam, T. J. W. Lazio, L. Levin, A. Lommen, D. R. Lorimer, J. Luo, R. S. Lynch, D. Madison, A. M. Matthews, M. A. McLaughlin, S. T. McWilliams, C. Mingarelli, C. Ng, D. J. Nice, T. T. Pennucci, S. M. Ransom, P. S. Ray, X. Siemens, J. Simon, R. Spiewak, I. H. Stairs, D. R.

Stinebring, K. Stovall, J. K. Swiggum, S. R. Taylor, M. Vallisneri, R. van Haasteren, S. J. Vigeland, and W. Zhu. The NANOGrav 11-year data set: High-precision timing of 45 millisecond pulsars. *The Astrophysical Journal Supplement Series*, 235(2):37, April 2018.

[ABC+09] S. Aoki, S. Y. Bahk, S. H. Chung, H. Funahashi, C. H. Hahn, M. Hanabata, T. Hara, S. Hirata, K. Hoshino, M. Ieiri, T. Iijima, K. Imai, Y. Itow, T. Jin-ya, M. Kazuno, C.O. Kim, J.Y. Kim, S. H. Kim, K. Kodama, T. Kuze, Y. Maeda, A. Masaike, A. Masuoka, Y. Matsuda, A. Matsui, Y. Nagase, C. Nagoshi, M. Nakamura, S. Nakanishi, T. Nakano, K. Nakazawa, K. Niwa, H. Oda, H. Okabe, S. Ono, R. Ozaki, B. D. Park, I. G. Park, K. Sakai, T. Sasaki, Y. Sato, H. Shibuya, H. M. Shimizu, J. S. Song, M. Sugimoto, H. Tajima, H. Takahashi, R. Takashima, F. Takeutchi, K. H. Tanaka, M. Teranaka, I. Tezuka, H. Togawa, T. Tsunemi, M. Ukai, N. Ushida, T. Watanabe, N. Yasuda, J. Yokota, and C. S. Yoon. Nuclear capture at rest of hyperons. *Nuclear Physics A*, 828(3-4):191–232, September 2009.

[ACCG19] Sofija Antić, Debarati Chatterjee, Thomas Carreau, and Francesca Gulminelli. Quantifying the uncertainties on spinodal instability for stellar matter through meta-modeling. *Journal of Physics G: Nuclear and Particle Physics*, 46(6):065109, 2019.

[AFW+13] J. Antoniadis, P. C. C. Freire, N. Wex, T. M. Tauris, R. S. Lynch, M. H. van Kerkwijk, M. Kramer, C. Bassa, V. S. Dhillon, T. Driebe, J. W. T. Hessels, V. M. Kaspi, V. I. Kondratiev, N. Langer, T. R. Marsh, M. A. McLaughlin, T. T. Pennucci, S. M. Ransom, I. H. Stairs, J. van Leeuwen, J. P. W. Verbiest, and D. G. Whelan. A massive pulsar in a compact relativistic binary. *Science*, 340(6131):1233232, April 2013.

[AGKV18] E. Annala, T. Gorda, A. Kurkela, and A. Vuorinen. Gravitational-wave constraints on the neutron-star-matter equation of state. *Physical Review Letters*, 120(17), April 2018.

[AHP13] M. G. Alford, S. Han, and M. Prakash. Generic conditions for stable hybrid stars. *Physical Review D*, 88(8), October 2013.

[AKV10] P. Romatschke A. Kurkela and A. Vuorinen. Cold quark matter. *Physical Review D*, 81:105021, May 2010.

[ASA15] N. Alam, A. Sulaksono, and B. K. Agrawal. Diversity of neutron star properties at the fixed neutron-skin thickness of ^{208}Pb. *Physical Review C*, 92:015804, 2015.

[BACK16] David Blaschke, DE Alvarez-Castillo, and T Klahn. Universal symmetry energy contribution to the neutron star equation of state. *arXiv preprint arXiv:1604.08575*, 2016.

[Bau03] T. Baumgarte. Numerical relativity and compact binaries. *Physics Reports*, 376(2):41, March 2003.

[BB98] S. Balberg and N. Barnea. S-wave pairing of Λ hyperons in dense matter. *Physical Review C*, 57(1):409–416, January 1998.

[BB16] M. Baldo and G. F. Burgio. The nuclear symmetry energy. *Progress in Particle and Nuclear Physics*, 91:203, 2016.

[BBG12] E. Botta, T. Bressani, and G. Garbarino. Strangeness nuclear physics: a critical review on selected topics. *The European Physical Journal A*, 48(3), March 2012.

[BBM08] J. Bartel, K. Bencheikh, and J. Meyer. Extended thomas-fermi density functionals in the presence of a tensor interaction in spherical symmetry. *Physical Review C*, 77(2), February 2008.

[BC76] G Baym and SA Chin. Can a neutron star be a giant mit bag? *Physics Letters B*, 62(2):241–244, 1976.

[BD05] K. Bennaceur and J. Dobaczewski. Coordinate-space solution of the Skyrme–Hartree–Fock–Bogolyubov equations within spherical symmetry. the program HFBRAD (v1.00). *Computer Physics Communications*, 168(2):96, June 2005.

[BFGQ75] M. Beiner, H. Flocard, Nguyen Van Giai, and P. Quentin. Nuclear ground-state properties and self-consistent calculations

with the Skyrme interaction. *Nuclear Physics A*, 238(1):29, January 1975.

[BFST88] D. Berdichevsky, R. Fleming, D. W. L. Sprung, and F. Tondeur. Charge and mass radii of the tin isotopes. *Zeitschrift für Physik A Atomic Nuclei*, 329(4):393–405, 1988.

[BHR03] M. Bender, P.-H. Heenen, and P.-G. Reinhard. Self-consistent mean-field models for nuclear structure. *Reviews of Modern Physics*, 75(1):121, January 2003.

[BL91] I. Bombaci and U. Lombardo. Asymmetric nuclear matter equation of state. *Physical Review C*, 44:1892–1900, Nov 1991.

[Boo07] *Star Deaths and the Formation of Compact Objects*. John Wiley & Sons, Ltd, 2007.

[BPM+02] E. Berti, J. A. Pons, G. Miniutti, L. Gualtieri, and V. Ferrari. Are post-Newtonian templates faithful and effectual in detecting gravitational signals from neutron star binaries? *Physical Review D*, 66(6), September 2002.

[BS15] P. Bedaque and A. W. Steiner. Sound velocity bound and neutron stars. *Physical Review Letters*, 114(3), January 2015.

[BT85] D. Berdichevsky and F. Tondeur. Nuclear core densities, isotope shifts, and the parametrization of the droplet model. *Zeitschrift für Physik A Atoms and Nuclei*, 322(1):141, 1985.

[CBH+98] E. Chabanat, P. Bonche, P. Haensel, J. Meyer, and R. Schaeffer. A Skyrme parametrization from subnuclear to neutron star densities Part II. Nuclei far from stabilities. *Nuclear Physics A*, 635(1-2):231, 1998.

[CCK+09] L.-W. Chen, B.-J. Cai, C. M. Ko, B.-A. Li, C. Shen, and J. Xu. Higher-order effects on the incompressibility of isospin asymmetric nuclear matter. *Physical Review C*, 80:014322, 2009.

[CDMM19] M. W. Coughlin, T. Dietrich, B. Margalit, and B. D. Metzger. Multi-messenger Bayesian parameter inference of a binary neutron-star merger. *Monthly Notices of the Royal Astronomical Society: Letters*, August 2019.

[CFR+19] H. T. Cromartie, E. Fonseca, S. M. Ransom, P. B. Demorest, Z. Arzoumanian, H. Blumer, P. R. Brook, M. E. DeCesar, T. Dolch, J. A. Ellis, R. D. Ferdman, E. C. Ferrara, N. Garver-Daniels, P. A. Gentile, M. L. Jones, M. T. Lam, D. R. Lorimer, R. S. Lynch, M. A. McLaughlin, C. Ng, D. J. Nice, T. T. Pennucci, R. Spiewak, I. H. Stairs, K. Stovall, J. K. Swiggum, and W. W. Zhu. Relativistic shapiro delay measurements of an extremely massive millisecond pulsar. *Nature Astronomy*, September 2019.

[CLS00] J. Cugnon, A. Lejeune, and H.-J. Schulze. Hypernuclei in the Skyrme-Hartree-Fock formalism with a microscopic hyperon-nucleon force. *Physical Review C*, 62(6), November 2000.

[CN76] George Chapline and Michael Nauenberg. Phase transition from baryon to quark matter. *Nature*, 264(5583):235–236, 1976.

[CS13] G. Colucci and A. Sedrakian. Equation of state of hypernuclear matter: impact of hyperon-scalar-meson couplings. *Physical Review C*, 87(5):055806, 2013.

[CSY19] Z. Carson, A. W. Steiner, and K. Yagi. Constraining nuclear matter parameters with GW170817. *Physical Review D*, 99(4), February 2019.

[CT02] C. Cutler and K. S. Thorne. An overview of gravitational-wave sources. In *General Relativity and Gravitation*. World Scientific, September 2002.

[CTB+19] C. D. Capano, I. Tews, Stephanie M. Brown, B. Margalit, S. De, S. Kumar, D. A. Brown, B. Krishnan, and S. Reddy. GW170817: Stringent constraints on neutron-star radii from multimessenger observations and nuclear theory. 2019.

[CV16] D. Chatterjee and I. Vidaña. Do hyperons exist in the interior of neutron stars? *The European Physical Journal A*, 52(2), February 2016.

[DFL+18] S. De, D. Finstad, J. M. Lattimer, D. A. Brown, E. Berger, and C. M. Biwer. Tidal Deformabilities and Radii of Neutron Stars

from the Observation of GW170817. *Physical Review Letters*, 121(9), August 2018.

[DFT84] J. Dobaczewski, H. Flocard, and J. Treiner. Hartree-Fock-Bogolyubov description of nuclei near the neutron-drip line. *Nuclear Physics A*, 422(1):103, June 1984.

[dGM+19] N. Baillot d'Etivaux, S. Guillot, J. Margueron, N. Webb, M. Catelan, and A. Reisenegger. New Constraints on the Nuclear Equation of State from the Thermal Emission of Neutron Stars in Quiescent Low-mass X-Ray Binaries. *The Astrophysical Journal*, 887(1):48, December 2019.

[DH01] F. Douchin and P. Haensel. A unified equation of state of dense matter and neutron star structure. *Astronomy & Astrophysics*, 380(1):151, December 2001.

[DHS16] C. Drischler, K. Hebeler, and A. Schwenk. Asymmetric nuclear matter based on chiral two- and three-nucleon interactions. *Physical Review C*, 93(5), May 2016.

[DL09] P. Danielewicz and J. Lee. Symmetry energy I: Semi-infinite matter. *Nuclear Physics A*, 818(1-2):36, February 2009.

[DMPV11] C. Ducoin, J. Margueron, C. Providência, and I. Vidaña. Core-crust transition in neutron stars: Predictivity of density developments. *Physical Review C*, 83(4), April 2011.

[DN09] T. Damour and A. Nagar. Relativistic tidal properties of neutron stars. *Physical Review D*, 80(8), October 2009.

[DNW+96] J Dobaczewski, W Nazarewicz, TR Werner, JF Berger, CR Chinn, and J Dechargé. Mean-field description of ground-state properties of drip-line nuclei: Pairing and continuum effects. *Physical Review C*, 53(6):2809, 1996.

[DP53] M. Danysz and J. Pniewski. Delayed disintegration of a heavy nuclear fragment: I. *The London, Edinburgh, and Dublin Philosophical Magazine and Journal of Science*, 44(350):348–350, March 1953.

[DZGL12] J. Dong, W. Z., J. Gu, and U. Lombardo. Density dependence of the nuclear symmetry energy constrained by mean-field calculations. *Physical Review C*, 85(3), March 2012.

[FAMF19] M. Fasano, T. Abdelsalhin, A. Maselli, and V. Ferrari. Constraining the Neutron Star Equation of State Using Multiband Independent Measurements of Radii and Tidal Deformabilities. *Physical Review Letters*, 123:141101, September 2019.

[FAPVn17] M. Fortin, S. S. Avancini, C. Providência, and I. Vidaña. Hypernuclei and massive neutron stars. *Physical Review C*, 95:065803, June 2017.

[Fav14] Marc Favata. Systematic parameter errors in inspiraling neutron star binaries. *Physical review letters*, 112(10):101101, 2014.

[FH08] É. É Flanagan and T. Hinderer. Constraining neutron-star tidal love numbers with gravitational-wave detectors. *Physical Review D*, 77(2):021502, 2008.

[FJ84] E. Farhi and R. L. Jaffe. Strange matter. *Physical Review D*, 30(11):2379, December 1984.

[FKLS92] B. Fenyi, T. G. Kovacs, I. Lovas, and K. Sailer. The effect of pion condensation on superfluidity in neutron stars. *Journal of Physics G: Nuclear and Particle Physics*, 18(6):1051, jun 1992.

[FKVW07] P. Finelli, N. Kaiser, D. Vretenar, and W. Weise. In-medium chiral $SU(3)$ dynamics and hypernuclear structure. *Physics Letters B*, 658(1):90, December 2007.

[FN15] A Feliciello and T Nagae. Experimental review of hypernuclear physics: recent achievements and future perspectives. *Reports on Progress in Physics*, 78(9):096301, August 2015.

[FPE+16] E. Fonseca, T. T. Pennucci, J. A. Ellis, I. H. Stairs, D. J. Nice, S. M. Ransom, P. B. Demorest, Z. Arzoumanian, K. Crowter, T. Dolch, R. D. Ferdman, M. E. Gonzalez, G. Jones, M. L. Jones, M. T. Lam, L. Levin, M. A. McLaughlin, K. Stovall, J. K. Swiggum, and W. Zhu. The Nanograv Nine-Year Data

Set: Mass and Geometric Measurements of Binary Millisecond Pulsars. *The Astrophysical Journal*, 832(2):167, dec 2016.

[FPT97] M. Farine, J. M. Pearson, and F. Tondeur. Nuclear-matter incompressibility from fits of generalized skyrme force to breathing-mode energies. *Nuclear Physics A*, 615(2):135, 1997.

[GCS19] R. O. Gomes, P. Char, and S. Schramm. Constraining Strangeness in Dense Matter with GW170817. *The Astrophysical Journal*, 877(2):139, June 2019.

[GDS12] N. Guleria, S. K. Dhiman, and R. Shyam. A study of Λ hypernuclei within the Skyrme–Hartree–Fock model. *Nuclear Physics A*, 886:71–91, July 2012.

[GHM16] A Gal, EV Hungerford, and DJ Millener. Strangeness in nuclear physics. *Reviews of Modern Physics*, 88(3):035004, 2016.

[Gin05] J. N. Ginocchio. Relativistic symmetries in nuclei and hadrons. *Physics Reports*, 414(4-5):165, August 2005.

[Gle87] NK Glendenning. Hyperons in neutron stars. *Zeitschrift für Physik A Atomic Nuclei*, 326(1):57–64, 1987.

[Gle12] Norman K Glendenning. *Compact stars: Nuclear physics, particle physics and general relativity*. Springer Science & Business Media, 2012.

[GLO+07] U. Garg, T. Li, S. Okumura, H. Akimune, M. Fujiwara, M.N. Harakeh, H. Hashimoto, M. Itoh, Y. Iwao, T. Kawabata, K. Kawase, Y. Liu, R. Marks, T. Murakami, K. Nakanishi, B.K. Nayak, P.V. Madhusudhana Rao, H. Sakaguchi, Y. Terashima, M. Uchida, Y. Yasuda, M. Yosoi, and J. Zenihiro. The Giant Monopole Resonance in the Sn Isotopes: Why is Tin so "Fluffy"? *Nuclear Physics A*, 788(1-4):36, May 2007.

[GM53] M. Gell-Mann. Isotopic spin and new unstable particles. *Physical Review*, 92(3):833, November 1953.

[Goo99] A. L. Goodman. Proton-neutron pairing in $z = n$ nuclei with $a = 76 - 96$. *Physical Review C*, 60(1), June 1999.

[GS81] N. V. Giai and H. Sagawa. Spin-isospin and pairing properties of modified skyrme interactions. *Physics Letters B*, 106(5):379, November 1981.

[GSWR13] S. Guillot, M. Servillat, N. A. Webb, and R. E. Rutledge. Measurement of the radius of neutron stars with high signal-to-noise quiescent low-mass X-ray binaries in globular clusters. *The Astrophysical Journal*, 772(1):7, June 2013.

[HF08] L. Hong-Feng. Extreme Exotic Calcium Lambda Hypernuclei in the Relativistic Continuum Hartree-Bogoliubov Theory. *Chinese Physics Letters*, 25(10):3613, October 2008.

[HFW+03] A. Heger, C. L. Fryer, S. E. Woosley, N. Langer, and D. H. Hartmann. How Massive Single Stars End Their Life. *The Astrophysical Journal*, 591(1):288, jul 2003.

[HII+89] R. S. Hayano, T. Ishikawa, M. Iwasaki, H. Outa, E. Takada, H. Tamura, A. Sakaguchi, M. Aoki, and T. Yamazaki. Evidence for a bound state of the He hypernucleus. *Physics Letters B*, 231(4):355, November 1989.

[Hin08] T. Hinderer. Tidal love numbers of neutron stars. *The Astrophysical Journal*, 677(2):1216, 2008.

[HN18] E. Hiyama and K. Nakazawa. Structure of S=-2 Hypernuclei and Hyperon–Hyperon Interactions. *Annual Review of Nuclear and Particle Science*, 68(1):131, October 2018.

[HP82] P. Haensel and M. Proszynski. Pion condensation in cold dense matter and neutron stars. *The Astrophysical Journal*, 258:306, July 1982.

[HPY07] P. Haensel, A. Y. Potekhin, and D. G. Yakovlev. *Neutron stars* 1*: Equation of state and structure*, volume 326. Springer Science & Business Media, 2007.

[HS19] S. Han and A. W. Steiner. Tidal deformability with sharp phase transitions in binary neutron stars. *Phys. Rev. D*, 99:083014, April 2019.

[HT06] O. Hashimoto and H. Tamura. Spectroscopy of Λ hypernuclei. *Progress in Particle and Nuclear Physics*, 57(2):564–653, October 2006.

[HTZ+18] N. Hornick, L. Tolos, A. Zacchi, J.-E. Christian, and J. Schaffner-Bielich. Relativistic parameterizations of neutron matter and implications for neutron stars. *Physical Review C*, 98(6):065804, 2018.

[HY09] Emiko Hiyama and T Yamada. Structure of light hypernuclei. *Progress in Particle and Nuclear Physics*, 63(2):339–395, 2009.

[Ito70] Naoki Itoh. Hydrostatic equilibrium of hypothetical quark stars. *Progress of Theoretical Physics*, 44(1):291–292, 1970.

[JLM+07] H.-T. Janka, K. Langanke, A. Marek, G. Martínez-Pinedo, and B. Müller. Theory of core-collapse supernovae. *Physics Reports*, 442(1):38, 2007.

[KAB+00] P. Khaustov, D. E. Alburger, P. D. Barnes, B. Bassalleck, A. R. Berdoz, A. Biglan, T. Bürger, D. S. Carman, R. E. Chrien, C. A. Davis, H. Fischer, G. B. Franklin, J. Franz, L. Gan, A. Ichikawa, T. Iijima, K. Imai, Y. Kondo, P. Koran, M. Landry, L. Lee, J. Lowe, R. Magahiz, M. May, R. McCrady, C. A. Meyer, F. Merrill, T. Motoba, S. A. Page, K. Paschke, P. H. Pile, B. Quinn, W. D. Ramsay, A. Rusek, R. Sawafta, H. Schmitt, R. A. Schumacher, R. W. Stotzer, R. Sutter, F. Takeutchi, W. T. H. van Oers, K. Yamamoto, Y. Yamamoto, M. Yosoi, and V. J. Zeps. Evidence of Ξ hypernuclear production in the 12C(K−, K+)Ξ 12Be reaction. *Physical Review C*, 61(5), March 2000.

[KK76] Bradley D Keister and Leonard S Kisslinger. Free-quark phases in dense stars. *Physics Letters B*, 64(1):117–120, 1976.

[KLK+18] Y.-M. Kim, Y. Lim, K. Kwak, C. H. Hyun, and C.-H. Lee. Tidal deformability of neutron stars with realistic nuclear energy density functionals. *Physical Review C*, 98(6):065805, 2018.

[KM13] E. Khan and J. Margueron. Determination of the density dependence of the nuclear incompressibility. *Physical Review C*, 88(3):034319, 2013.

[KMGR15] E. Khan, J. Margueron, F. Gulminelli, and A. R. Raduta. Microscopic evaluation of the hypernuclear chart with λ hyperons. *Physical Review C*, 92(4), October 2015.

[KMV12] E. Khan, J. Margueron, and I. Vidaña. Constraining the nuclear equation of state at subsaturation densities. *Physical review letters*, 109(9):092501, 2012.

[LC05] B.-A. Li and L.-W. Chen. Nucleon-nucleon cross sections in neutron-rich matter and isospin transport in heavy-ion reactions at intermediate energies. *Physical Review C*, 72(6), December 2005.

[LCK08] B.-A. Li, L.-W. Chen, and C. M. Ko. Recent progress and new challenges in isospin physics with heavy-ion reactions. *Physics Reports*, 464(4-6):113, August 2008.

[LDL+19] O. Lourenço, M. Dutra, C. H. Lenzi, C. V. Flores, and D. P. Menezes. Consistent relativistic mean-field models constrained by gw170817. *Physical Review C*, 99(4):045202, 2019.

[LGL+07] T. Li, U. Garg, Y. Liu, R. Marks, B. K. Nayak, P. V. Madhusudhana Rao, M. Fujiwara, H. Hashimoto, K. Kawase, K. Nakanishi, S. Okumura, M. Yosoi, M. Itoh, M. Ichikawa, R. Matsuo, T. Terazono, M. Uchida, T. Kawabata, H. Akimune, Y. Iwao, T. Murakami, H. Sakaguchi, S. Terashima, Y. Yasuda, J. Zenihiro, and M. N. Harakeh. Isotopic Dependence of the Giant Monopole Resonance in the Even-A $^{112-124}$Sn Isotopes and the Asymmetry Term in Nuclear Incompressibility. *Physical Review Letters*, 99(16), October 2007.

[LGP13] D. Lonardoni, S. Gandolfi, and F. Pederiva. Effects of the two-body and three-body hyperon-nucleon interactions in Λ hypernuclei. *Physical Review C*, 87(4), April 2013.

[LH13] B.-A. Li and X. Han. Constraining the neutron–proton effective mass splitting using empirical constraints on the density dependence of nuclear symmetry energy around normal density. *Physics Letters B*, 727(1-3):276, 2013.

[LH18] Y. Lim and J. W. Holt. Neutron star tidal deformabilities constrained by nuclear theory and experiment. *Physical Review Letters*, 121(6):062701, 2018.

[LH19] Y. Lim and J. W. Holt. Bayesian modeling of the nuclear equation of state for neutron star tidal deformabilities and GW170817. *The European Physical Journal A*, 55(11), November 2019.

[LLGP15] D. Lonardoni, A. Lovato, S. Gandolfi, and F. Pederiva. Hyperon Puzzle: Hints from Quantum Monte Carlo Calculations. *Physical Review Letters*, 114(9), March 2015.

[LMZ15] Haozhao Liang, Jie Meng, and Shan-Gui Zhou. Hidden pseudospin and spin symmetries and their origins in atomic nuclei. *Physics Reports*, 570:1, March 2015.

[LP07] J. M. Lattimer and M. Prakash. Neutron star observations: Prognosis for equation of state constraints. *Physics Reports*, 442(1):109, April 2007.

[LS08] Z. H. Li and H.-J. Schulze. Neutron star structure with modern nucleonic three-body forces. *Physical Review C*, 78(2), August 2008.

[LS14] J. M. Lattimer and A. W. Steiner. Constraints on the symmetry energy using the mass-radius relation of neutron stars. *The European Physical Journal A*, 50(2):40, 2014.

[LSC18] M. Linares, T. Shahbaz, and J. Casares. Peering into the dark side: Magnesium lines establish a massive neutron star in psr j2215+ 5135. *The Astrophysical Journal*, 859(1):54, 2018.

[MAD+17] C. Mondal, B. K. Agrawal, J. N. De, S. K. Samaddar, M. Centelles, and X. Viñas. Interdependence of different symmetry energy elements. *Physical Review C*, 96:021302, 2017.

[MAD+19] T. Malik, B. K. Agrawal, J. N. De, S. K. Samaddar, C. Providência, C. Mondal, and T. K. Jha. Tides in merging neutron stars: Consistency of the GW170817 event with experimental data on finite nuclei. *Physical Review C*, 99(5), May 2019.

[MAF+18] T. Malik, N. Alam, M. Fortin, C. Providência, B. K. Agrawal, T. K. Jha, B. Kumar, and S. K. Patra. GW170817: Constraining the nuclear matter equation of state from the neutron star tidal deformability. *Physical Review C*, 98(3):035804, 2018.

[MCG18a] J. Margueron, R. H. Casali, and F. Gulminelli. Equation of state for dense nucleonic matter from metamodeling. I. Foundational aspects. *Physical Review C*, 97(2):025805, 2018.

[MCG18b] J. Margueron, R. H. Casali, and F. Gulminelli. Equation of state for dense nucleonic matter from metamodeling. II. Predictions for neutron star properties. *Physical Review C*, 97(2):025806, 2018.

[MDDS+18] A. Marino, N. Degenaar, T. Di Salvo, R. Wijnands, L. Burderi, and R. Iaria. On obtaining neutron star mass and radius constraints from quiescent low-mass x-ray binaries in the galactic plane. *Monthly Notices of the Royal Astronomical Society*, 479(3):3634, 2018.

[Met17] B. D. Metzger. Kilonovae. *Living Reviews in Relativity*, 20(1), May 2017.

[MG19] J. Margueron and F. Gulminelli. Effect of high-order empirical parameters on the nuclear equation of state. *Physical Review C*, 99:025806, 2019.

[MKG17] J. Margueron, E. Khan, and F. Gulminelli. Density Functional approach for multistrange hypernuclei: Competition between Λ and $\Xi^{0,-}$, hyperons. *Physical Review C*, 96(5), November 2017.

[MKV15] K. A. Maslov, E. E. Kolomeitsev, and D. N. Voskresensky. Solution of the hyperon puzzle within a relativistic mean-field model. *Physics Letters B*, 748:369, September 2015.

[MLMY08] T. Motoba, D. E. Lanskoy, D. J. Millener, and Y. Yamamoto. Λ spin–orbit splitting in heavy hypernuclei as deduced from DWIA analyses of the reaction. *Nuclear Physics A*, 804(1):99–115, May 2008.

[MR19] L. McLerran and S. Reddy. Quarkyonic Matter and Neutron Stars. *Physical Review Letters*, 122:122701, March 2019.

[MTHR19] G. Montana, L. Tolós, M. Hanauske, and L. Rezzolla. Constraining twin stars with gw170817. *Physical Review D*, 99(10):103009, 2019.

[MTW73] C. W. Misner, K. S. Thorne, and J. A. Wheeler. *Gravitation*. 1973.

[MWRSB18] E. R. Most, L. R. Weih, L. Rezzolla, and J. Schaffner-Bielich. New constraints on radii and tidal deformabilities of neutron stars from gw170817. *Physical Review Letters*, 120(26):261103, 2018.

[NAA+19] M. Nakagawa, M. Agnello, Y. Akazawa, N. Amano, K. Aoki, E. Botta, N. Chiga, H. Ekawa, P. Evtoukhovitch, A. Feliciello, M. Fujita, T. Gogami, S. Hasegawa, S. H. Hayakawa, T. Hayakawa, R. Honda, K. Hosomi, S. Hwang, N. Ichige, Y. Ichikawa, M. Ikeda, K. Imai, S. Ishimoto, S. Kanatsuki, M. Kim, S. Kim, S. Kinbara, T. Koike, J. Lee, S. Marcello, K. Miwa, T. Moon, T. Nagae, S. Nagao, Y. Nakada, Y. Ogura, A. Sakaguchi, H. Sako, Y. Sasaki, S. Sato, T. Shiozaki, K. Shirotori, H. Sugimura, S. Suto, S. Suzuki, T. Takahashi, H. Tamura, K. Tanabe, K. Tanida, Z. Tsamalaidze, M. Ukai, T. O. Yamamoto, Y. Yamamoto, and S. Yang. Search for excited state of \(_{\sigma }^{4}\text{he}\) hypernucleus in the j-PARC e13 experiment. In *Proceedings of the 8th International Conference on Quarks and Nuclear Physics (QNP2018)*. Journal of the Physical Society of Japan, November 2019.

[Nag13] T. Nagae. Strangeness nuclear physics at j-PARC. *Few-Body Systems*, 54(7):785, January 2013.

[NCP19] R. Nandi, P. Char, and S. Pal. Constraining the relativistic mean-field model equations of state with gravitational wave observations. *Physical Review C*, 99:052802, May 2019.

[NEF+15] K. Nakazawa, Y. Endo, S. Fukunaga, K. Hoshino, S. H. Hwang, K. Imai, H. Ito, K. Itonaga, T. Kanda, M. Kawasaki, J. H. Kim, S. Kinbara, H. Kobayashi, A. Mishina, S. Ogawa, H. Shibuya, T. Sugimura, M. K. Soe, H. Takahashi, T. Takahashi, K. T. Tint, K. Umehara, C. S. Yoon, and J. Yoshida. The first evidence of a deeply bound state of $Xi^- - {}^{14}N$ system. *Progress of Theoretical and Experimental Physics*, 2015(3):33D02, March 2015.

[NN53] T. Nakano and K. Nishijima. Charge independence forV-particles. *Progress of Theoretical Physics*, 10(5):581, November 1953.

[NT10] K. Nakazawa and H. Takahashi. Experimental Study of Double-Λ Hypernuclei with Nuclear Emulsion. *Progress of Theoretical Physics Supplement*, 185:335, 2010.

[ÖF16] F. Özel and Paulo Freire. Masses, radii, and the equation of state of neutron stars. *Annual Review of Astronomy and Astrophysics*, 54:401, 2016.

[ÖPG+16] F. Özel, D. Psaltis, T. Güver, G. Baym, C. Heinke, and S. Guillot. The dense matter equation of state from neutron star radius and mass measurements. *The Astrophysical Journal*, 820(1):28, mar 2016.

[OV39] J. R. Oppenheimer and G. M. Volkoff. On massive neutron cores. *Physical Review*, 55(4):374, 1939.

[PC09a] J. Piekarewicz and M. Centelles. Incompressibility of neutron-rich matter. *Physical Review C*, 79(5):054311, 2009.

[PC09b] J. Piekarewicz and M. Centelles. Incompressibility of neutron-rich matter. *Physical Review C*, 79:054311, 2009.

[PLPS04] D. Page, J. M. Lattimer, M. Prakash, and A. W. Steiner. Minimal cooling of neutron stars: A new paradigm. *The Astrophysical Journal Supplement Series*, 155(2):623, December 2004.

[PYAC+18] V. Paschalidis, K. Yagi, D. Alvarez-Castillo, D. B. Blaschke, and A. Sedrakian. Implications from GW170817 and i-love-q relations for relativistic hybrid stars. *Physical Review D*, 97(8), April 2018.

[RMCS12] X. Roca-Maza, G. Colò, and H. Sagawa. New skyrme interaction with improved spin-isospin properties. *Physical Review C*, 86(3), September 2012.

[RMCS18] X. Roca-Maza, G. Colò, and H. Sagawa. Nuclear Symmetry Energy and the Breaking of the Isospin Symmetry: How Do They Reconcile with Each Other? *Physical Review Letters*, 120(20):202501, 2018.

[ROP16] C. A. Raithel, F. Özel, and D. Psaltis. From Neutron Star Observables to The Equation of State. I. An Optimal Parametrization. *The Astrophysical Journal*, 831(1):44, October 2016.

[RÖP17] C. A. Raithel, F. Özel, and D. Psaltis. From Neutron Star Observables to the Equation of State. II. Bayesian Inference of Equation of State Pressures. *The Astrophysical Journal*, 844(2):156, aug 2017.

[RPJ+18] L. Rezzolla, P. Pizzochero, D. I. Jones, N. Rea, and I. Vidaña. *The Physics and Astrophysics of Neutron Stars*. Springer International Publishing, 2018.

[RR74] Clifford E. Rhoades and Remo Ruffini. Maximum Mass of a Neutron Star. *Physical Review Letters*, 32:324, February 1974.

[RS04] Peter Ring and Peter Schuck. *The nuclear many-body problem*. Springer Science & Business Media, 2004.

[RSW17] A. R. Raduta, A. Sedrakian, and F. Weber. Cooling of hypernuclear compact stars. *Monthly Notices of the Royal Astronomical Society*, 475(4):4347, December 2017.

[RSZ17] S.-H. Ren, T.-T. Sun, and W. Zhang. Green's function relativistic mean field theory for Λ hypernuclei. 95(5), May 2017.

[Sam10] C. Samanta. Generalized mass formula for non-strange, strange and multiply-strange nuclear systems. *Journal of Physics G: Nuclear and Particle Physics*, 37(7):075104, May 2010.

[SBG00] J. Schaffner-Bielich and A. Gal. Properties of strange hadronic matter in bulk and in finite systems. *Physical Review C*, 62(3), August 2000.

[SC19] A. Sedrakian and J. W. Clark. Superfluidity in nuclear systems and neutron stars. *The European Physical Journal A*, 55(9), September 2019.

[SDLmcD14] B. M. Santos, M. Dutra, O. Lourenço, and A. Delfino. Correlations between the nuclear matter symmetry energy, its slope, and curvature from a nonrelativistic solvable approach and beyond. *Physical Review C*, 90:035203, 2014.

[SLB10] A. W. Steiner, J. M. Lattimer, and E. F. Brown. The equation of state from observed masses and radii of neutron stars. *The Astrophysical Journal*, 722(1):33, 2010.

[SNR+12] T. R. Saito, D. Nakajima, C. Rappold, S. Bianchin, O. Borodina, V. Bozkurt, B. Göküzüm, M. Kavatsyuk, E. Kim, Y. Ma, F. Maas, S. Minami, B. Özel Tashenov, P. Achenbach, S. Ajimura, T. Aumann, C. Ayerbe Gayoso, H.C. Bhang, C. Caesar, S. Erturk, T. Fukuda, E. Guliev, Y. Hayashi, T. Hiraiwa, J. Hoffmann, G. Ickert, Z.S. Ketenci, D. Khaneft, M. Kim, S. Kim, K. Koch, N. Kurz, A. Le Fevre, Y. Mizoi, M. Moritsu, T. Nagae, L. Nungesser, A. Okamura, W. Ott, J. Pochodzalla, A. Sakaguchi, M. Sako, C. J. Schmidt, M. Sekimoto, H. Simon, H. Sugimura, T. Takahashi, G. J. Tambave, H. Tamura, W. Trautmann, S. Voltz, N. Yokota, C. J. Yoon, and K. Yoshida. Production of hypernuclei in peripheral HI collisions: The HypHI project at GSI. *Nuclear Physics A*, 881:218, May 2012.

[SR13] H.-J. Schulze and T. Rijken. Hypernuclear structure with the Nijmegen ESC08 potentials. *Physical Review C*, 88(2), August 2013.

[SS06] D. Sivia and J. Skilling. *Data analysis: a Bayesian tutorial*. OUP Oxford, 2006.

[SYC19] H. Sagawa, S. Yoshida, and L.-G. Cao. EoS from terrestrial experiments: Static and dynamic polarizations of nuclear density. In *Xiamen-Custipen Workshop on The Equation of State of Dense Neutron-Rich Matter in The Era of Gravitational Wave Astronomy*. AIP Publishing, 2019.

[TAA+01] H. Takahashi, J. K. Ahn, H. Akikawa, S. Aoki, K. Arai, S. Y. Bahk, K. M. Baik, B. Bassalleck, J. H. Chung, M. S. Chung, D. H. Davis, T. Fukuda, K. Hoshino, A. Ichikawa, M. Ieiri, K. Imai, Y. H. Iwata, Y. S. Iwata, H. Kanda, M. Kaneko, T. Kawai, M. Kawasaki, C. O. Kim, J. Y. Kim, S. J. Kim, S. H. Kim, Y. Kondo, T. Kouketsu, Y. L. Lee, J. W. C. McNabb, M. Mitsuhara, Y. Nagase, C. Nagoshi, K. Nakazawa, H. Noumi, S. Ogawa, H. Okabe, K. Oyama, H. M. Park, I. G. Park, J. Parker, Y. S. Ra, J. T. Rhee, A. Rusek, H. Shibuya, K. S. Sim, P. K. Saha, D. Seki, M. Sekimoto, J. S. Song, T. Takahash, F. Takeutchi, H. Tanaka, K. Tanida, J. Tojo, H. Torii, S. Torikai, D. N. Tovee, N. Ushida, K. Yamamoto, N. Yasuda, J. T. Yang, C. J. Yoon, C. S. Yoon, M. Yosoi, T. Yoshida, and L. Zhu. Observation of a $^{6}\mathrm{He}_{\Lambda\Lambda}$ Double Hypernucleus. *Physical Review Letters*, 87(21), November 2001.

[Tan19] Y. Tanimura. Clusterization and deformation of multi- Λ hypernuclei within a relativistic mean-field model. *Physical Review C*, 99(3), March 2019.

[TC67] K. S. Thorne and A. Campolattaro. Non-Radial Pulsation of General-Relativistic Stellar Models. I. Analytic Analysis for L $\geq$ 2. *The Astrophysical Journal*, 149:591, September 1967.

[THH+18] M. Tanabashi, K. Hagiwara, K. Hikasa, K. Nakamura, Y. Sumino, F. Takahashi, J. Tanaka, K. Agashe, G. Aielli, C. Amsler, M. Antonelli, D. M. Asner, H. Baer, Sw. Banerjee, R.

M. Barnett, T. Basaglia, C. W. Bauer, J. J. Beatty, V. I. Belousov, J. Beringer, S. Bethke, A. Bettini, H. Bichsel, O. Biebel, K. M. Black, E. Blucher, O. Buchmuller, V. Burkert, M. A. Bychkov, R. N. Cahn, M. Carena, A. Ceccucci, A. Cerri, D. Chakraborty, M.-C. Chen, R. S. Chivukula, G. Cowan, O. Dahl, G. D'Ambrosio, T. Damour, D. de Florian, A. de Gouvêa, T. DeGrand, P. de Jong, G. Dissertori, B. A. Dobrescu, M. D'Onofrio, M. Doser, M. Drees, H. K. Dreiner, D. A. Dwyer, P. Eerola, S. Eidelman, J. Ellis, J. Erler, V. V. Ezhela, W. Fetscher, B. D. Fields, R. Firestone, B. Foster, A. Freitas, H. Gallagher, L. Garren, H.-J. Gerber, G. Gerbier, T. Gershon, Y. Gershtein, T. Gherghetta, A. A. Godizov, M. Goodman, C. Grab, A. V. Gritsan, C. Grojean, D. E. Groom, M. Grünewald, A. Gurtu, T. Gutsche, H. E. Haber, C. Hanhart, S. Hashimoto, Y. Hayato, K. G. Hayes, A. Hebecker, S. Heinemeyer, B. Heltsley, J. J. Hernández-Rey, J. Hisano, A. Höcker, J. Holder, A. Holtkamp, T. Hyodo, K. D. Irwin, K. F. Johnson, M. Kado, M. Karliner, U. F. Katz, S. R. Klein, E. Klempt, R. V. Kowalewski, F. Krauss, M. Kreps, B. Krusche, Y. V. Kuyanov, Y. Kwon, O. Lahav, J. Laiho, J. Lesgourgues, A. Liddle, Z. Ligeti, C.-J. Lin, C. Lippmann, T. M. Liss, L. Littenberg, K. S. Lugovsky, S. B. Lugovsky, A. Lusiani, Y. Makida, F. Maltoni, T. Mannel, A. V. Manohar, W. J. Marciano, A. D. Martin, A. Masoni, J. Matthews, U.-G. Meißner, D. Milstead, R. E. Mitchell, K. Mönig, P. Molaro, F. Moortgat, M. Moskovic, H. Murayama, M. Narain, P. Nason, S. Navas, M. Neubert, P. Nevski, Y. Nir, K. A. Olive, S. Pagan Griso, J. Parsons, C. Patrignani, J. A. Peacock, M. Pennington, S. T. Petcov, V. A. Petrov, E. Pianori, A. Piepke, A. Pomarol, A. Quadt, J. Rademacker, G. Raffelt, B. N. Ratcliff, P. Richardson, A. Ringwald, S. Roesler, S. Rolli, A. Romaniouk, L. J. Rosenberg, J. L. Rosner, G. Rybka, R. A. Ryutin, C. T. Sachrajda, Y. Sakai, G. P. Salam, S. Sarkar, F. Sauli, O. Schneider, K. Scholberg, A. J. Schwartz, D. Scott, V. Sharma, S. R. Sharpe, T. Shutt, M. Silari, T. Sjöstrand, P. Skands, T. Skwarnicki, J. G. Smith, G. F. Smoot, S. Spanier, H. Spieler, C. Spiering, A. Stahl, S. L. Stone, T. Sumiyoshi, M.

J. Syphers, K. Terashi, J. Terning, U. Thoma, R. S. Thorne, L. Tiator, M. Titov, N. P. Tkachenko, N. A. Törnqvist, D. R. Tovey, G. Valencia, R. Van de Water, N. Varelas, G. Venanzoni, L. Verde, M. G. Vincter, P. Vogel, A. Vogt, S. P. Wakely, W. Walkowiak, C. W. Walter, D. Wands, D. R. Ward, M. O. Wascko, G. Weiglein, D. H. Weinberg, E. J. Weinberg, M. White, L. R. Wiencke, S. Willocq, C. G. Wohl, J. Womersley, C. L. Woody, R. L. Workman, W.-M. Yao, G. P. Zeller, O. V. Zenin, R.-Y. Zhu, S.-L. Zhu, F. Zimmermann, P. A. Zyla, J. Anderson, L. Fuller, V. S. Lugovsky, and P. Schaffner and. Review of particle physics. *Physical Review D*, 98(3), August 2018.

[Tho98] K. S. Thorne. Tidal stabilization of rigidly rotating, fully relativistic neutron stars. *Physical Review D*, 58:124031, Nov 1998.

[TLOK17] I. Tews, J. M. Lattimer, A. Ohnishi, and E. E. Kolomeitsev. Symmetry Parameter Constraints from a Lower Bound on Neutron-matter Energy. *The Astrophysical Journal*, 848(2):105, October 2017.

[TMC03] T. Tanigawa, M. Matsuzaki, and S. Chiba. Possibility of $\Lambda\Lambda$ pairing and its dependence on background density in a relativistic Hartree-Bogoliubov model. *Physical Review C*, 68(1), July 2003.

[TMR18] I. Tews, J. Margueron, and S. Reddy. Critical examination of constraints on the equation of state of dense matter obtained from gw170817. *Physical Review C*, 98:045804, October 2018.

[TMR19] I. Tews, J. Margueron, and S. Reddy. Confronting gravitational-wave observations with modern nuclear physics constraints. *The European Physical Journal A*, 55(6), June 2019.

[Tol39] R. C. Tolman. Static solutions of einstein's field equations for spheres of fluid. *Physical Review*, 55(4):364, 1939.

[TT00] T. Takatsuka and R. Tamagaki. Λ-hyperon superfluidity in

neutron star cores. *Nuclear Physics A*, 670(1-4):222–225, May 2000.

[vDCS14] E. N. E. van Dalen, G. Colucci, and A. Sedrakian. Constraining hypernuclear density functional with Λ-hypernuclei and compact stars. *Physics Letters B*, 734:383–387, June 2014.

[VPPR09] I. Vidaña, C. Providência, A. Polls, and A. Rios. Density dependence of the nuclear symmetry energy: A microscopic perspective. *Physical Review C*, 80(4), October 2009.

[VPRS01] I. Vidaña, A. Polls, A. Ramos, and H.-J. Schulze. Hypernuclear structure with the new Nijmegen potentials. *Physical Review C*, 64(4), September 2001.

[WFS71] H. H. Wolter, Amand Faessler, and P. U. Sauer. HFB calculations with t = 1 and t = 0 pairing correlations. *Nuclear Physics A*, 167(1):108, May 1971.

[WS10] Y. N. Wang and H. Shen. Superfluidity of Λ hyperons in neutron stars. *Physical Review C*, 81(2), February 2010.

[YS06] S. Yoshida and H. Sagawa. Isovector nuclear matter properties and neutron skin thickness. *Physical Review C*, 73(4), April 2006.

[YSZ+18] J. Yasuda, M. Sasano, R. G. T. Zegers, H. Baba, D. Bazin, W. Chao, M. Dozono, N. Fukuda, N. Inabe, T. Isobe, G. Jhang, D. Kameda, M. Kaneko, K. Kisamori, M. Kobayashi, N. Kobayashi, T. Kobayashi, S. Koyama, Y. Kondo, A. J. Krasznahorkay, T. Kubo, Y. Kubota, M. Kurata-Nishimura, C. S. Lee, J. W. Lee, Y. Matsuda, E. Milman, S. Michimasa, T. Motobayashi, D. Muecher, T. Murakami, T. Nakamura, N. Nakatsuka, S. Ota, H. Otsu, V. Panin, W. Powell, S. Reichert, S. Sakaguchi, H. Sakai, M. Sako, H. Sato, Y. Shimizu, M. Shikata, S. Shimoura, L. Stuhl, T. Sumikama, H. Suzuki, S. Tangwancharoen, M. Takaki, H. Takeda, T. Tako, Y. Togano, H. Tokieda, J. Tsubota, T. Uesaka, T. Wakasa,

K. Yako, K. Yoneda, and J. Zenihiro. Extraction of the Landau-Migdal Parameter from the Gamow-Teller Giant Resonance in ^{132}Sn. *Physical Review Letters*, 121(13), September 2018.

[YSZZ98] S. Yao-Song and R. Zhong-Zhou. Relativistic mean-field approaches for light hypernuclei. *Acta Physica Sinica (Overseas Edition)*, 7(4):258–270, April 1998.

[ZCZ19] Y. Zhou, L.-W. Chen, and Z. Zhang. Equation of state of dense matter in the multimessenger era. *Physical Review D*, 99(12), June 2019.

[ZH13] J. L. Zdunik and P. Haensel. Maximum mass of neutron stars and strange neutron-star cores. *Astronomy & Astrophysics*, 551:A61, 2013.

[ZHS16] X.-R. Zhou, E. Hiyama, and H. Sagawa. Exotic structure of medium-heavy hypernuclei in the Skyrme Hartree-Fock model. *Physical Review C*, 94(2), August 2016.

[ZSPD05] X.-R. Zhou, H.-J. Schulze, F. Pan, and J. P. Draayer. Strong Hyperon-Nucleon Pairing in Neutron Stars. *Physical Review Letters*, 95(5), July 2005.

List of Figures

List of Tables

université PARIS-SACLAY

ÉCOLE DOCTORALE
Particules, hadrons, énergie et noyau: instrumentation, imagerie, cosmos et simulation (PHENIICS)

Titre: Physique nucléaire dans les étoiles à neutrons : Etude de la superfluidité dans les hypernoyaux et contraintes sur les équations d'état

Mots clés: Etoiles à neutrons, Hypernoyaux, Equation d'état, Ondes gravitationelles, Structure nucléaire, Superfluidité

Résumé: Dans cette thése nous avons d'abord étudié l'effet du paring Lambda sur les propriétés des hypernoyaux dans le formalisme Hartree-Fock Bogoliubov. La fonctionnelle de Skyrme SLy5 est utilisée dans le canal nucleon-nucleon alors que 3 fonctionelles fittées sur les calculs microscopiques Brueckner Hartree-Fock sont utilisées dans le canal NΛ: DF-NSC89, DF-NSC97a et DF-NSC97f. Ces fonctionelles décrivent la séquence des énergies de liaison expérimentales à un Λ, des hypernoyaux légers aux hypernoyaux lourds. Dans le cas du canal ΛΛ, nous avons utilisé la prescription empirique EmpC, ajustée à 1 MeV sur l'énergie expérimentale de liaison dans le $^{6}\mathrm{He}_{\Lambda\Lambda}$. A l'aide de cette approche de la fonctionelle de la densité, plusieurs noyaux ont été étudiés, avec des couches nucléoniques fermées et des couches ouvertes en Λ. Une interaction d'appariement Lambda-Lambda est introduite, dont la magnitude est ajustée pour être consistante avec la valeur maximale des prédictions BCS pour le gap d'appariement Λ dans la matière hyperonique. Nous donnons ainsi une valeur maximale pour la prédiction du gap d'appariement Λ et ses effets dans les hypernoyaux. Nous avons montré que les effets de l'appariement ΛΛ dependent de l'hypernoyau considéré. L'énergie correspondante de condensation est de l'ordre de 3 MeV au maximum, ce qui entraine de faibles corrections sur les distributions de densité et la structure en couches. De manière générale, nous avons trouvé que l'appariement ΛΛ peut être important si l'écart en énergie entre les couches est plus petit que 3 MeV. A cette condition, l'appariement Lambda peut impacter les densité et les énergies de liaison. En résumé, il est montré que l'effet de l'appariement relié aux Λ peut être en général négligé dans la plupart des hypernoyaux, sauf pour les ceux ayant un écart typique dans le spectre à une particule plus petit que 3 MeV autour du niveau de Fermi. De plus, les conditions sur à la fois les énergies de Fermi et les moments angulaire orbitaux atténuent l'appariement nucleon-Λ pour la plupart des hypernoyaux. La deuxième partie de la thèse est dévolue aux équations d'état dans les étoiles à neutrons. Nous avons confronté les valeurs des déformabilités de marée extraites de l'évènement d'onde gravitationnelle GW170817, aux contraintes issues de la physique nucléaire à l'aide d'une approche semi-agnostique pour l'équation d'état de la matière dense. Nous avons utilisé les statistiques Bayesienne pour combiner les données de physique nucléaire à basse densité, comme les prédictions ab initio provenant des interactions chirales EFT ou la resonance géante monopolaire isoscalaire, et les contraintes astrophysiques sur les étoiles à neutrons, comme leur masse maximale, ou la fonction densité de probabilité de la déformabilité de marée obtenue de l'événement GW170817. Les fonctions postérieures de densité de probabilité sont marginalisées sur plusieurs paramètres nucléaires empiriques (L_{sym}, K_{sym}, Q_{sat} et Q_{sym}), et aussi sur des grandeurs observationnelles des étoiles à neutrons comme la masse et le rayon à 1.4 masses solaires, ou la pression à deux fois la densité de saturation $P(2n_{\mathrm{sat}})$. Les correlations entre L_{sym} et K_{sym}, et entre K_{sat} et Q_{sat} sont aussi analysées. Une tension importante entre les données observationnelles d'ondes gravitationnelles et les inputs de physique nucléaire est trouvée pour les distributions marginales de probabilité de Lsym et $R_{1.4}$. Ceci pourrait être une indication d'une transition de phase de nucléons vers des particules plus exotiques dans le coeur des étoiles à neutrons. Nous trouvons aussi qu'augmenter la précision sur la détermination de la déformabilité de marée à partir des ondes gravitationnelles, ou sur M_c à partir de la résonance géantes monopolaire, devrait aboutir à une meilleure determination de K_{sat} et Q_{sat}.

Title: Nuclear Physics in Neutron Stars: Study of Superfluidity in Hypernuclei and Constraining the Nuclear Equation of State

Keywords: Neutron Stars, Hypernuclei, Equation of State, Gravitational Wave, Nuclear Structure, Superfluidity

Abstract: In this thesis, we first investigated the effect of Λ pairing on the ground state properties of hypernuclei within the Hartree-Fock-Bogoliubov formalism. The SLy5 Skyrme functional is used in the NN channel, while for NΛ channel we employ three functionals fitted from microscopic Brueckner-Hartree-Fock calculations: DF-NSC89, DF-NSC97a and DF-NSC97f. These functionals reproduce the sequence of single-Λ experimental binding energies from light to heavy hypernuclei. For the ΛΛ channel, we used the empirical prescription EmpC, calibrated to 1 MeV on the experimental bond energy in $^{6}\mathrm{He}_{\Lambda\Lambda}$. Based on this density-functional approach, several nuclei have been studied with nucleon closed-shells and Λ open-shells. A ΛΛ pairing interaction is introduced, which magnitude is calibrated to be consistent with the maximum BCS predictions for the Λ pairing gap in hypernuclear matter. In this way, we provide an upper bound for the prediction of the Λ pairing gap and its effects in hypernuclei. We have shown that the effects of the ΛΛ pairing depends on hypernuclei. The condensation energy is predicted to be about 3 MeV as a maximum value, yielding small corrections on density distributions and shell structure. Generally, we found that ΛΛ pairing could be active if the energy gap between shells is smaller than 3 MeV. Under this condition, Λ pairing could impact densities and binding energies. Since only a weak spin-orbit interaction is expected in the Λ channel, Λ states are highly degenerated and usually levels are distant by more than 3 MeV in energy. In summary, it is shown that the Λ-related pairing effect can usually be neglected in most of hypernuclei, except for hypernuclei which have a single particle gap lower than 3 MeV around the Fermi level. In addition, conditions on both Fermi energies and orbital angular momenta are expected to quench the nucleon-Λ pairing for most of hypernuclei.

The second part of the thesis is devoted to equation of states in neutron stars. We confronted the tidal deformability values extracted from the gravitational event GW170817 to nuclear physics constraints within a semi-agnostic approach for the dense matter equation of state. We used Bayesian statistics to combine together low density nuclear physics data, such as the ab-initio predictions based on χEFT interactions or the isoscalar giant monopole resonance, and astrophysical constraints from neutron stars, such as the maximum mass of neutron stars or the probability density function of the tidal deformability $\tilde{\Lambda}$ obtained from the GW170817 event. The posteriors probability distribution functions are marginalized over several nuclear empirical parameters (L_{sym}, K_{sym}, Q_{sat} and Q_{sym}), as well as over observational quantities such as the $1.4M_{\odot}$ radius $R_{1.4}$ and the pressure at twice the saturation density $P(2n_{\mathrm{sat}})$. The correlations between L_{sym} and K_{sym} and between K_{sat} and Q_{sat} are also further analyzed. It is found that there is a marked tension between the gravitational wave observational data and the nuclear physics inputs for the L_{sym} and $R_{1.4}$ marginal probability distributions. This could be a hint for nucleons to more exotic particles phase transition inside of the core of neutron stars. We also conclude that increasing the accuracy on the determination of tidal deformability from the gravitational wave, as well as M_c from the isoscalar giant monopole resonance, will lead to a better determination of K_{sat} and Q_{sat}.

Université Paris-Saclay
Espace Technologique / Immeuble Discovery
Route de l'Orme aux Merisiers RD 128 / 91190 Saint-Aubin, France